Modeling the collapse of Hebes Chasma, Valles Marineris, Mars

M.P.A. Jackson[1,†], J.B. Adams[2], T.P. Dooley[1], A.R. Gillespie[2], and D.R. Montgomery[2]
[1]*Bureau of Economic Geology, Jackson School of Geosciences, University of Texas, Austin, Texas 78713, USA*
[2]*Department of Earth and Space Sciences, University of Washington, Seattle, Washington 98195, USA*

ABSTRACT

Physical modeling and detailed mapping of Hebes Chasma provide new insights into the crustal composition and origin of the Valles Marineris region of equatorial Mars. Hebes Chasma is a 315-km-long and 8-km-deep closed depression containing distinctive landforms that include diapirs and extensive allochthonous flows that end in pits. A central puzzle of Hebes Chasma is how and where 10^5 km^3 of missing material disappeared. Our physical models tested the hypothesis that the chasma formed by collapse and removal of material from below. Gravity-driven collapse in the models reproduced all the chasma's main landforms as subsidence evolved from early sagging of the upper surface, to inward collapse and removal of material, to emergence of diapirs and low-gradient flows. The models and geologic evidence suggest that Hebes Mensa arched upward diapirically and raised deep stratigraphy almost level with the chasma rim. If the chasma indeed collapsed by subsurface drainage as occurred in the models, the upper 8–10 km of deposits at Hebes must have been solid to depths of ~5 km but viscous at greater depths. The materials removed could not have consisted mainly of basalt flows; instead, they probably were a mixture of hydrated and nonhydrated salts, water ice, liquid water, and insoluble (likely basaltic) particles. The proportions of these constituents are unknown but constrained because the material drained from the subsiding chasma and apparently contributed to the outburst floods released down neighboring Echus Chasma and Kasei Valles.

INTRODUCTION

The Valles Marineris chasmata are a strikingly linear set of trenches trending east-southeast along the north rim of the Thaumasia Plateau in equatorial Mars (Fig. 1A). Among the northern chasmata is Hebes Chasma, a cavity 315 km long and 126 km wide. The chasma is more than 8 km deep from its rim at +3950 m to its floor at –4530 m and is one of the deepest canyons on Mars. This huge cavity implies removal of 10^5 km^3 of material (the present-day volume of the chasma estimated using Mars Orbiter Laser Altimeter [MOLA] data). The composition and fate of the vanished material are a puzzle that has exercised researchers trying to explain the origin of Valles Marineris chasmata and similar canyons (Table 1).

Deep as it is, Hebes Chasma is dwarfed in length by other major canyons nearby in Valles Marineris (Fig. 1A). However, Hebes Chasma has an unusual allure for research into the origin of the chasmata: This closed canyon lacks any surface outlets, so an origin by fluvial erosion is not viable. A hypothesis of downward drainage has been considered for Valles Marineris in general (Table 1) and for Hebes Chasma in particular through photogeologic mapping and a briefly described physical model of collapse (Adams et al., 2009). Here, we present the full results and structural analysis of physical modeling designed to test and elucidate the hypothesis of downward drainage and collapse inferred by Adams et al. (2009). We compare specific features of the models with geometrically similar Hebes landforms illustrated in Figure 1B and discuss these at length in the second half of the paper. This comparison leads to new insights into the evolution of landforms in Hebes Chasma. The conclusions have implications for the composition of the upper few kilometers of deposits in Hebes Chasma and elsewhere on Mars, but especially in the Valles Marineris region (Fig. 1A).

As far as we know, this is the first attempt to physically model the tectonics of a Martian canyon using scaled materials. The models reproduce the structures in Hebes Chasma and reveal a complex balance of karstic downward drainage, upward reactive diapirism, and surface flows partly akin to allochthonous salt tectonics on Earth. This balance varied over time and from place to place within the model and probably within Hebes Chasma too. Although the modeling and mapping provide a comprehensive view of how a distinctive suite of landforms evolved in Hebes Chasma, many pieces of the puzzle remain hidden.

PREVIOUS HYPOTHESES FOR FORMATION OF CHASMATA

Previous ideas on the origin of the chasmata have three themes: erosional excavation, tectonic rifting, and karstic collapse (Table 1).

Surface erosion entails removal of 10^5 km^3 of material from the chasma by water or wind (Fig. 2A). Although fluvial erosion was widespread on Mars, removal of this volume of material by water erosion is impossible for Hebes Chasma because it lacks an outlet, and no fluvial channels are visible on the floor of either the chasma or canyons leading into it. Because of this fatal flaw, we do not consider further an origin for Hebes Chasma by fluvial erosion. Some wind erosion is likely. Within the chasma, wind has scoured yardangs and deposited sparse dunes and possibly some of the dark smooth deposits. Windborne sediment has undoubtedly left and entered the chasma, but the balance is unknown.

An origin by wind erosion would have several implications (Fig. 2A). Collapse structures in the chasma walls and in Hebes Mensa would have formed in response to the space produced by wind excavation. The youngest stratigraphic layers could not underlie the floor or the benches because erosion would have removed shallow units. The layered rocks exposed along the edges of benches would differ from the rimrock of the chasma. Hebes Mensa would be an erosional remnant of the same material as the walls, or it would consist of younger

[†]E-mail: martin.jackson@beg.utexas.edu.

 10.1130/B30307.1; 27 figures; 3 tables; Data Repository item 2011021.

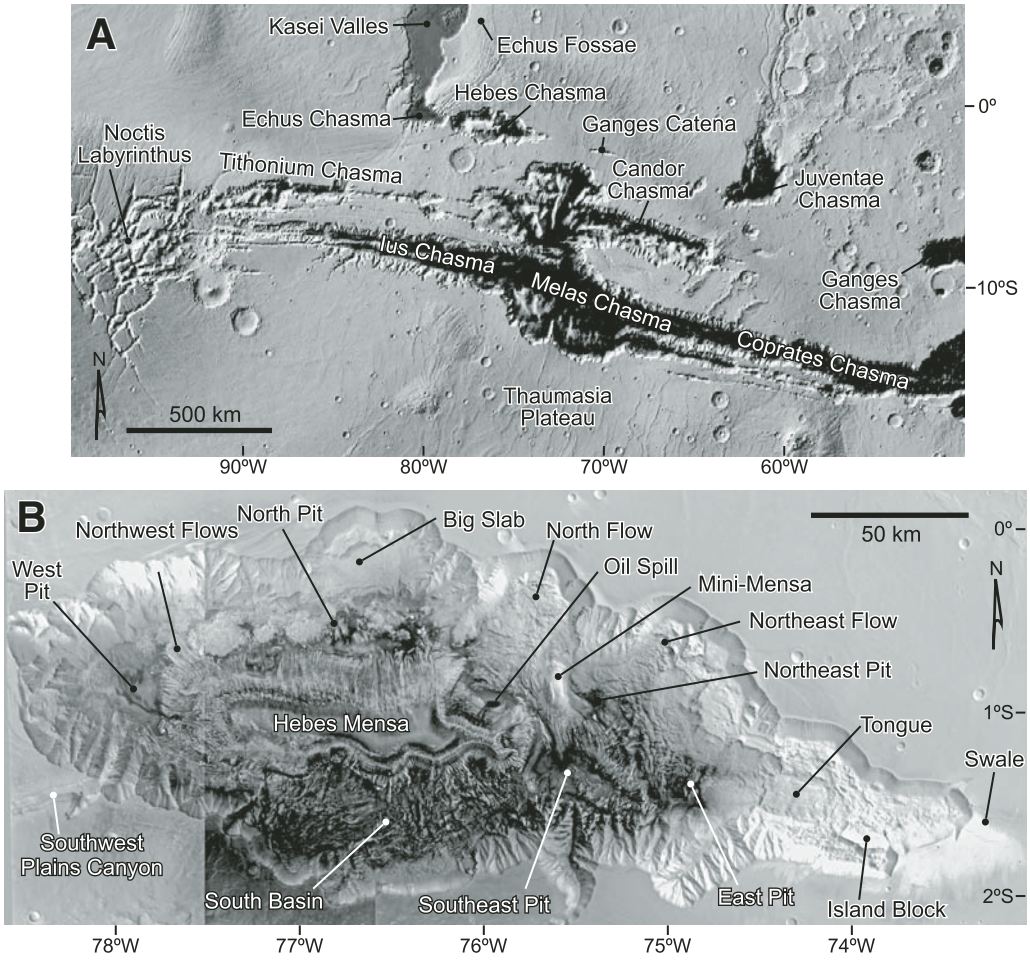

Figure 1. (A) Valles Marineris region showing the location of Hebes Chasma and nearby features. Mars Orbiter Laser Altimeter data. (B) Visible mosaic of Hebes Chasma showing informal place names used in this paper. Mars Express High Resolution Stereo Camera.

deposits filling a precursor chasma then left as an erosional remnant after a second episode of chasma excavation.

Several features argue against wind erosion as the chief agent of chasma excavation. (1) The canyon rim is sharp and scalloped, not rounded, hollowed, or grooved by wind erosion. (2) Wind erosion cannot explain a wide variety of features in Hebes Chasma: the shape and scale of the excavated cavity; or the swale at the east end of the chasma; or the preservation of the plains surface and the youngest layers on fault-bounded benches; or the arcuate headwall scarps in the chasma walls; or the pits, flows, and diapirs in the chasma floor. (3) Only a thin mantle of dust covers the chasma rim, though wind could have carried and deposited the dust elsewhere on the planet. So although surface erosion by water or wind was undoubtedly important in other canyons (Table 1), it is unlikely to be the main agent that formed Hebes Chasma.

TABLE 1. PREVIOUS HYPOTHESES FOR FORMATION OF THE VALLES MARINERIS CHASMATA

Hypotheses	Authors
Erosion	McCauley et al. (1972); Sharp (1973); Lucchitta (1979)
Collapse by removal of water or magma	Sharp (1973); Courtillot et al. (1975); Schonfeld (1979); Tanaka and Golombek (1989); Spencer and Fanale (1990); Schultz (1998); Schultz and Lin (2001); Fueten et al. (2005); Rodriguez et al. (2006); Rossi et al. (2008)
Tectonic rifting	Sharp (1973); Blasius et al. (1977); Frey (1979); Masson (1977, 1985); Schonfeld (1979); Anderson and Grimm (1998); Schultz (1991, 1995); Chadwick and Lucchitta (1993); Peulvast and Masson (1993); Mége and Masson (1996); Peulvast et al. (2001); Wilkins and Schultz (2003); Bleamaster (2009)
Combination of mechanisms	Lucchitta et al. (1992); Tanaka (1997); Schultz (1998); Lucchitta and Chapman (2002); Montgomery and Gillespie (2005); Montgomery et al. (2009)

The tectonic rifting hypothesis invokes an origin by north-south tectonic extension, forming Hebes Chasma as a graben (Fig. 2B). Some features support this idea. (1) Regional structure obviously influenced the location of Hebes Chasma and its parallelism with other Valles Marineris chasmata. (2) Downdropped benches of younger layers and the many scarps of normal faults along the chasma walls also point to strong extensional control.

An origin by tectonic extension has several implications (Fig. 2B). The youngest layers would underlie the chasma floor and would be covered by deposits derived by wasting of chasma walls. Hebes Mensa could be a central horst, and the youngest layers of its crest would have been eroded. Alternatively, the mensa could consist of younger sediments deposited on the down-dropped plains surface. Layered rocks in the mensa extend almost as high as the chasma rim. So if they are depositional, they must have once filled the chasma. If they filled the chasma,

all that fill except for the present mensa must have been removed in an unexplained second episode of canyon formation.

Several features are inconsistent with a chasma origin purely by tectonic rifting (Fig. 1B). (1) The elliptical planform, abrupt scalloped margins, blunt ends, and roughly uniform depth of chasma are atypical of rifts (although Wilkins and Schultz [2003] explained the blunt ends by inferred reactivated cross faults, using criteria that can equally be explained by karstic subsidence). (2) Absence of extensional structures on surrounding plains, except for sporadic, narrow, shallow fossae, allows little north-south extension to create the huge volume of the chasma. (3) Pits and allochthonous flows on the floor and sides of the chasma and mensa are not extensional.

Because Hebes Chasma cannot be plausibly explained by erosional excavation or tectonic rifting, our paper focuses on the third main hypothesis: karstic collapse. Melting ground ice and draining meltwater loses volume, so melting ice was an early suspect for causing collapse (Sharp, 1973; Nedell et al., 1987). Because the present canyon walls are too steep to consist largely of weak ice, Spencer and Fanale (1990) inferred that ice accumulated in a strong graben that originally created the chasma. Permafrost ice is unlikely to be more than 1–2 km deep for plausible geotherms past and present, whereas the present floor of Hebes Chasma is 7–8 km deep. For this reason, Spencer and Fanale (1990) favored chemical dissolution or thermal decomposition of carbonates as the agent for karstic collapse.

Our discussion section revisits the question of the type of material that could have vanished from the chasma. Before that section, we describe the physical model results and illustrate how the results explain the landforms of Hebes Chasma and its mensa.

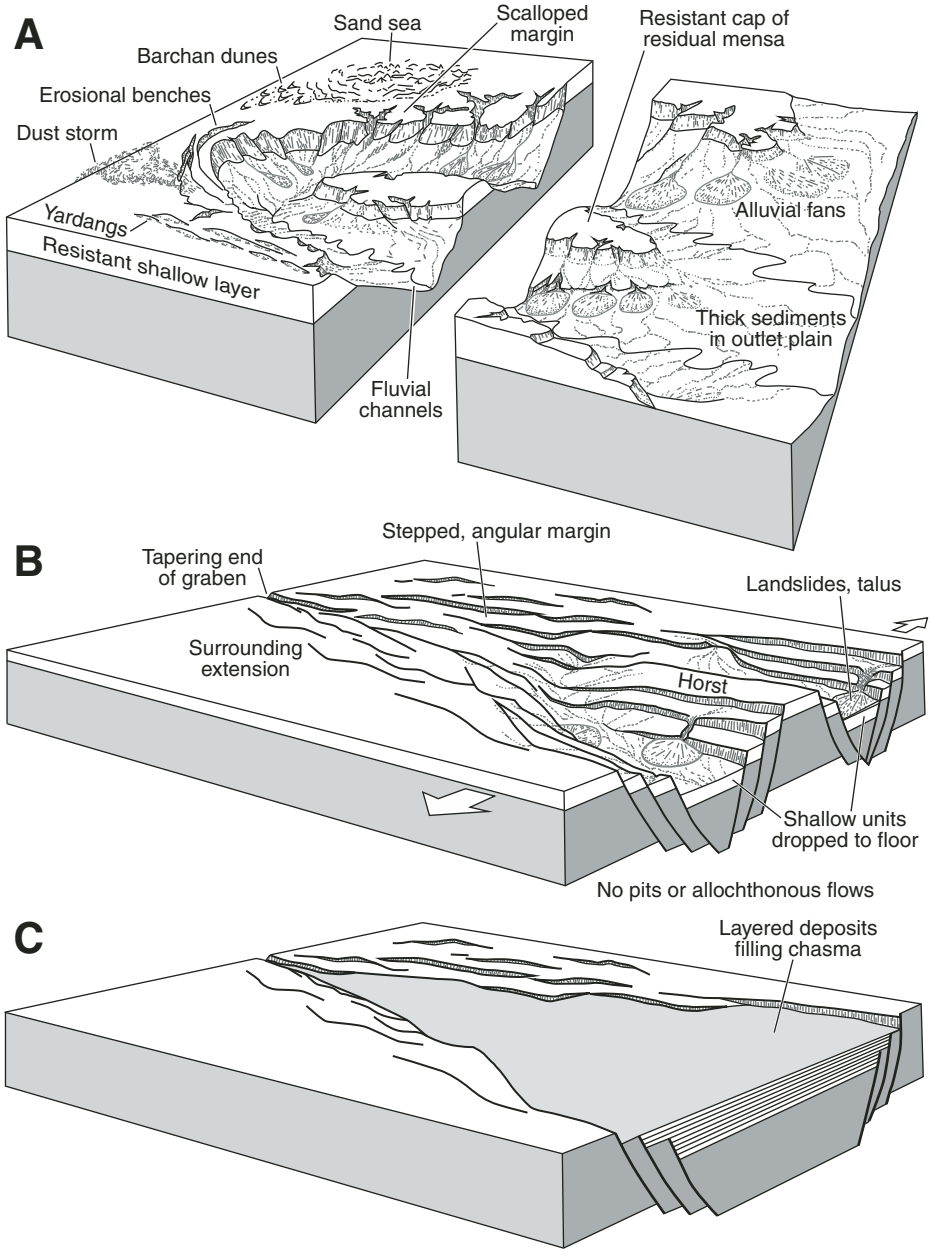

Figure 2. Block diagrams summarizing previous hypotheses for the origin of Valles Marineris chasmata: (A) erosional excavation, (B) tectonic rifting, and (C) tectonic rifting and postchasma infill by layered deposits. Table 1 summarizes sources of data.

MODEL DESIGN

Model Rationale

Some geologic processes can be seen directly, but others must be inferred because either they do not occur today or they operate at inaccessible depths. Processes can often be inferred from fragmentary traces left by different stages of an incomplete process. However, this classic inductive approach in geology is impractical if much of the early history is erased. Given the large volume of material removed from Hebes Chasma, we can reasonably assume that most of the early evidence was destroyed as the chasma deepened further. We cannot see the processes that formed Hebes Chasma, only some of their results. It is because we do not know presumptively how the chasma formed that our models test the hypothesis that Hebes Chasma subsided by karstic withdrawal of material from below. The models simulated both subsidence and diapirism. Modeling did not address the cause of subsidence, merely the process and results of subsidence.

The advantage of physical modeling is that it illustrates how early subsidence could have occurred, evidence of which is sparsely preserved in Hebes Chasma. In the models, landforms changed as each new stage of subsidence altered or replaced older ones. Caution is advisable when interpreting timing in the physical models. No model could reproduce all the features of Hebes in the same sequence that they formed in different parts of the chasma. The models drained continuously, but we do not know how drainage rates varied in space and time on Mars. Hence, the models did not necessarily stop subsiding at the same local evolutionary stage as in the equivalent place in Hebes, nor did the models reproduce any geologic or

erosional processes that may have further shaped Hebes Chasma after subsidence ended.

Model Materials

Ideally, the model materials should simulate the mechanical behavior of materials in Hebes Chasma. Matching mechanical behavior is difficult because the lithology of the chasma walls is uncertain. Chasma walls in the Valles Marineris show widespread layering (e.g., Malin and Edgett, 2001). A dominant inference is that these layers consist entirely of lavas flows, or lava interbedded with volcanic ash, or layered intrusions (e.g., McEwen et al., 1999; Beyer and McEwen, 2005). However, McEwen et al. (1999) could not exclude the possibility that the layers are largely sedimentary, and Beyer and McEwen (2005) concluded that Coprates Chasma walls consisted of thin, strong layers interbedded with thicker, weaker layers. Others have proposed unusually weak mixtures including salts to explain detachments and landslides in the Valles Marineris (Montgomery and Gillespie, 2005; Bigot-Cormier and Montgomery, 2007; Montgomery et al., 2009). Adams et al. (2009) presented evidence that Hebes Chasma and its mensa must be strong enough to sustain rugged topography but able to soften enough to have upwelled and flowed at the surface, and yielded fluids that drained or evaporated in vast quantities to form a closed depression.

The contrasting requirements of strength and the ability to flow, upwell, and drain implied by the landforms of Hebes Chasma suggest a three-layer mechanical stratigraphy for the models (Fig. 3). The uppermost unit 1 was represented by a strong, brittle layer of blue sand slightly moistened on its upper surface by mist from a squeezed water bottle. Dampness increased the cohesive strength of the sand surface and highlighted fractures and faults. Unit 1 simulated the erosionally resistant cap on the Martian plains surface, which responds to deformation by faulting. Next down, unit 2 was a weak, brittle layer of dry, glass microspheres having negligible cohesion and the ability to form particulate flows on slopes. This layer simulates the lower chasma walls, which are brittle but have ridge-and-gully topography suggesting material with lower frictional strength than the uppermost unit. At the base of the model was unit 3, a weak, viscous layer of near-Newtonian silicone polymer, polydimethylsiloxane. This unit simulates the deepest part of Hebes stratigraphy, which from the evidence presented later in this paper, we infer was mobilized as diapirs and allochthonous flows.

Model Construction

The stratigraphic thicknesses in Figure 3 filled a cutout in a rigid horizontal base having the planform of Hebes Chasma (Fig. 4). A wide bench separated the outer limit of unit 3 and the drainage slots. These sinuous slots of variable width in the rigid base of the model allowed overlying viscous and granular materials to drain out slowly. Drainage rates varied spatially depending on the width of the slots and the size of their catchment areas. A horizontal plate attached to a screwjack controlled the drainage rate through the overlying slots (Fig. 4). These irregular slots of controlled drainage represent any natural system of vertical drains, especially a system of irregular concentrations of fractures that may have widened into cavities in the upper kilometer or so as subsidence intensified. An "island" free of unit 3 localized the future mensa. The models deformed under 1*g* gravitational acceleration.

Model stratigraphy and strength profile	Model materials	Hebes equivalent
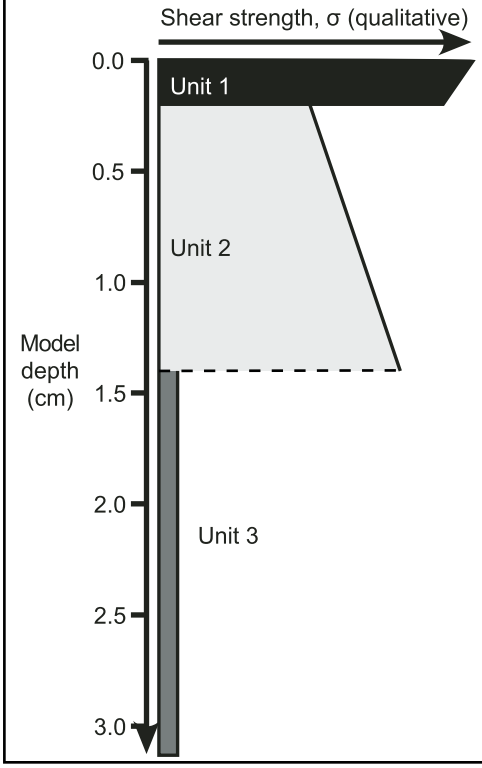	Unit 1: strong, damp, brittle veneer of blue silica sand. 2 mm thick, scaling to 1 km. Strong cohesion; Density, ρ = 1600 kg m^{-3} Coefficient of friction, μ > 0.65 Grain size, d = 300 μm	Upper Hebes Formation (UHF). 600–1000 m thick. Resistant layered cap of chasma rim.
	Unit 2: weak brittle layer of solid, white, glass beads. 12 mm thick, scaling to 6 km. Weak cohesion ≅ 2.5 x 10^4 Pas Density, ρ = 1600 kg m^{-3} Grain size, d = 90 μm	Lower Hebes Formation (LHF). 6 km thick. Layered weak units now forming the lower part of chasma.
	Unit 3: weak viscous layer. 20 mm thick, scaling to 10 km. Density, ρ = 970 kg m^{-3} Dynamic viscosity, η = 2.5 x 10^4 Pas	Lower Hebes Formation, 8–12 km thick. Largely missing.

Figure 3. Mechanical stratigraphy and qualitative strength profile of the three model layers and equivalent geologic units in Hebes Chasma. Figure 13 and Table 3 summarize Hebes geologic data.

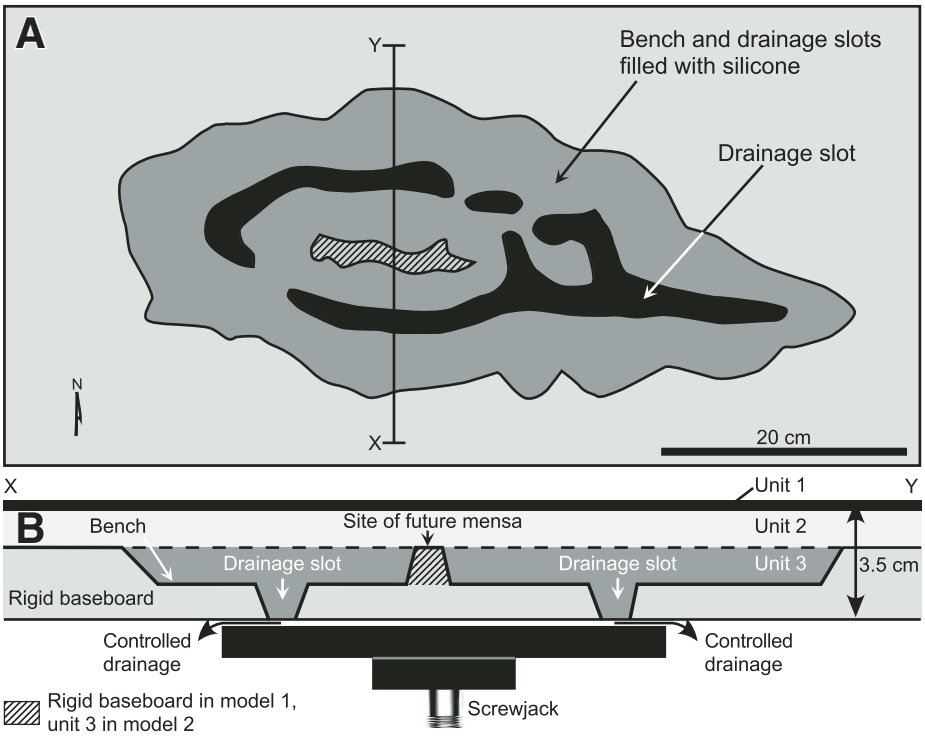

Figure 4. Model 1 setup before deformation in (A) plan view and (B) cross section. Figure 2 describes units 1, 2, and 3.

Two other closely similar models tested the effects of specific variations. Model 2 differed from model 1 in having unit 3 below the mensa. Model 3 differed from model 2 in having unit 3 across the entire model. Unless specifically referenced to the contrary, all model results refer to model 1.

Model Scaling

Table 2 shows the dynamic scaling of the model. Following Ramberg (1981), each model ratio is a model quantity divided by the equivalent quantity in nature. For example, the model's length scale of 2 mm to 1 km is a model length ratio of 2×10^{-6}. This length scale fixes the scaled thickness of the three stratigraphic units in the model (Fig. 3). The model chasma was 60 cm long and 26 cm wide, equivalent to 300 × 130 km in Hebes Chasma. The chasma's depth after deformation ranged from 14 mm to 24 mm, with an average of 16 mm. The upscaled equivalent of 16 mm is 8 km, which is the maximum depth of Hebes Chasma.

TABLE 2. SCALING OF PHYSICAL MODELS

Quantity	Model	Nature	Model ratio
Length, map view	l_m = **2 mm**	l_o = **1 km**	$l_r = 2 \times 10^{-6}$
Density, impure halite (unit 3)	ρ_m = **970 kg m^{-3}**	ρ_o = **2200 kg m^{-3}**	ρ_r = 0.44
Density, kieserite (unit 3)	ρ_m = **970 kg m^{-3}**	ρ_o = **2600 kg m^{-3}**	ρ_r = 0.37
Density, 70% tephra, 30% water ice (unit 3)	ρ_m = **970 kg m^{-3}**	ρ_o = **1350 kg m^{-3}**	ρ_r = 0.72
Density, 70% tephra, 30% halite (unit 3)	ρ_m = **970 kg m^{-3}**	ρ_o = **1710 kg m^{-3}**	ρ_r = 0.57
Density, overburden (unit 2)	ρ_m = **1600 kg m^{-3}**	ρ_o = **3600 kg m^{-3}** ρ_o = **4300 kg m^{-3}**	ρ_r = 0.44 ρ_r = 0.37
Gravity acceleration	$a_m = 1g$ = **9.8 m s^{-2}**	$a_o = 0.38g$ = **3.7 m s^{-2}**	a_r = 2.6
Strain			$\varepsilon_r = 1$
Stress or strength			$\sigma_r = \rho_r l a_r = 2.3 \times 10^{-6}$
Viscosity, dynamic, halite	η_m = **2.5 × 10^4 Pa s**	η_o = **1 × 10^{18} Pa s**	$\eta_r = 2.5 \times 10^{-14}$
Time, entire subsidence	t_m = 30 h = **1.1 × 10^5 s**	$t_o = 1.5 \times 10^{12}$ s = 310 k.y.	$t_r = \eta_r/\sigma_r = 1.1 \times 10^{-8}$
Time, diapiric emergence	t_m = 12.5 h = **4.5 × 10^4 s**	$t_o = 5.9 \times 10^{11}$ s = 130 k.y.	$t_r = \eta_r/\sigma_r = 1.1 \times 10^{-8}$
Velocity, surface flows	v_m = **1 × 10^{-6} m s^{-1}**	$v_o = v_m/v_r = 5.5 \times 10^{-9}$ m s^{-1} = 0.18 m yr^{-1}	$v_r = l/t_r$

Note: Values in bold are known or assumed. Other values are calculated from model ratios shown.

These length dimensions are simple to scale. All other properties include dimensions of mass and time, which are poorly known, so their scaling is more speculative. For example, what are the densities of the walls of Hebes Chasma and of the material inferred to have drained from the chasma? As shown in Table 2, a model ratio of density based on impure rock salt (2200 kg/m^3) is 0.44; the density ratio for kieserite (2600 kg/m^3), a denser hydrous salt, is only 0.37. The density ratio for a mixture of 70% tephra and 30% water ice is 0.72; for 70% tephra and 30% halite, the density ratio is 1.19. To scale strain, we wish to know what the deformed model would look like if it were geometrically scaled up to nature. The model ratio of strain is therefore 1 (Table 2). The model ratio for acceleration due to gravity is 2.6 because Mars has a smaller mass than Earth. For viscosity, we arbitrarily assume that the most mobile material in Hebes had the dynamic viscosity of rock salt, or ~1×10^{18} Pa s (van Keken et al., 1993). This viscosity model ratio yields model ratios of time and velocity from which we calculate that subsidence of a hypothetical scaled-up chasma in nature would have lasted 310 k.y. (Table 2). With the same model ratios of time and velocity, hypothetical scaled-up small diapirs reached the surface after 130 k.y. Scaled up, the fastest viscous extrusions at surface would flow at 0.18 m/yr—a velocity about one-tenth the rate of the most active subaerial salt glaciers in Iran and one-tenth to one-hundredth the rate of nonsurging ice glaciers (Talbot and Pohjola, 2009). These numbers are artificially precise because they are based on a particular assumed value of viscosity. Natural strain rates would scale 10 times slower for natural viscosities of 10^{19} Pa s and 10 times faster for 10^{17} Pa s. On Mars, the range of viscosity could be even larger than two magnitudes, given the uncertainties of Hebes lithology. For example, the viscosity of water ice varies between 10^{10} Pa s and 10^{14} Pa s, depending on grain size and temperature (Talbot and Pohjola, 2009). The viscosity of rock glaciers increases from these values as the content of rock fragments rises. Lithology also controls density, which affects the scaling ratios for stress, viscosity, time, and velocity. The scaling ratios in Table 2 are based on the density of halite because halite flows readily and because its mechanical properties are well known. If the buoyant unit 3 were instead equivalent to a tephra/salt/ice mixture, the results in nature would be difficult to predict because of complex interactions. For example, for a fixed viscosity, diapirs of tephra/salt/ice would rise faster and flows would drain or spread more slowly than for halite. However,

a decrease of viscosity for a fixed density would accelerate both diapirism and subsidence in nature. The scaling values of Table 2 are therefore illustrative rather than predictive.

Model Data Capture

A laser scanner and optical cameras recorded the evolution of each model. Laser scanning mapped the model's topography and tracked changes in relief on a submillimeter scale. Each laser scan produced more than 8×10^6 points, which yielded high-resolution three-dimensional (3-D) surfaces. Computer-controlled cameras photographed the model surface in overhead and oblique views. Shot at set intervals, these images yielded a time-lapse animation of the model's evolution (Fig. DR1[1]).

All model photographs were lit from the north at oblique incidence, and all model figures are oriented with Hebes north at the top, located in Figure 5.

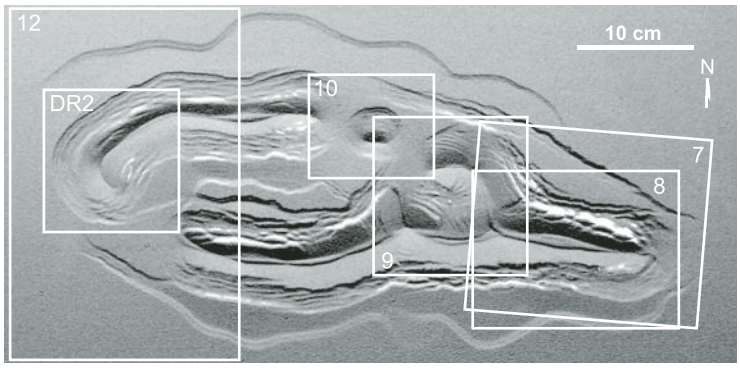

Figure 5. Locality map of illustrations of model 1, lit from the north.

MODEL EVOLUTION

Stage 1: Sagging

The first signs of subsidence were swales, where the plains surface sagged gently above drainage slots (Figs. 6A, 6B, and 7A). As the swales sagged further, incipient grabens formed along their bounding hinges. These grabens acted as hinges that allowed the sides of the swales to sag inward and downward. Thrusts formed along the axis of each swale where opposed slabs met in a crease. Thus, inner contraction balanced outer extension. As sagging intensified, swales deepened, hinge grabens lengthened, and axial thrusts increased in slip (Fig. 7B).

Stage 2: Extension and Axial Thrusting

Widespread extension spread outward to the edge of the viscous unit 3 (Fig. 6C). In outer parts of the chasma, fault blocks tilted gently outward against the bounding normal faults (Figs. 7D and 7E). In inner parts of the chasma, hinge grabens widened, stretching the blue plains surface of unit 1. This extension exposed the underlying pale unit 2 in scarp slopes of tilted fault blocks (Figs. 7C and 7D). Below the thinned grabens, diapiric walls began to rise reactively but remained below the surface. Reactive diapirs rise where extension thins the overburden above a mobile layer (Vendeville and Jackson, 1992). Hinging on these grabens, slabs capped by the plains surface tilted steeply inward toward the zones of subsidence (Figs. 7B and 7C). Along the crease of these subsidence zones, thrusts intensified. At the head of the westernmost drainage trench, curved thrust traces radiated from the deepest point of the drainage trench (Fig. DR2E [see footnote 1]). The thrust pattern resembled a closing iris shutter in a camera as thrust plates overrode one another and converged on the drainage pit. Inward sliding resulted in constrictional crowding.

Between the pits and trenches, residual highs remained, the largest of which was the future mensa (Figs. 6B and 6C). Crests of these highs were stretched in patterns controlled by adjoining drainage pits and trenches. For example, equant highs formed radial grabens, whereas elongate highs formed parallel grabens (Fig. 6C).

Stage 3: Landsliding, Drainage, and Diapiric Emergence

Continued subsidence gradually destroyed the plains surface in the center of the chasma as extension, landslides, and drainage intensified (Figs. 6D and 8).

Extension on the upper sides of drainage pits and trenches created parallel relays of normal faults (Fig. 7B). These faults formed benches that stepped down from the plains surface into the chasma. Arcuate faults at the end of drainage trenches intersected as they lengthened, carving out small rhombic fault blocks as breached relay structures (Figs. 7C and 7D). As these rhombic fault blocks subsided inward, they left curved headwall scarps that linked as a chain of inward-facing alcoves along the rim of the growing chasma (Fig. 6D).

While slabs of units 1 and 2 tilted inward into drainage troughs, they continued to extend (Fig. DR2 [see footnote 1]). As fault traces migrated toward drainage troughs, extension widened the distance between the faults. New normal faults formed updip, while the oldest faults disappeared into the drainage crease. Axial thrusts also drained down pits and trenches, which gradually enlarged (Figs. 7C and 7D).

During this advanced extension, diapirs emerged after rising buoyantly because unit 3 had a density 61% of the overburden density. The extension pattern strongly controlled diapirism. Extensional thinning exposed first the underlying pale unit 2, and then ridges of unit 3 that had been rising as reactive diapiric walls until they surfaced (Figs. 7D and 7F).

Linear walls were the most common diapir, rising below the extensional hinges of inward-tilting slabs of units 1 and 2 (Fig. 8A). A chain of diapiric culminations formed along the upwelling walls wherever unit 3 rose fastest. Eventually, lower parts of the upwelling chain also breached the surface and joined into continuous, emergent walls (Fig. 8B).

Pluglike stocks were less common and formed in three settings. In the first, stocks emerged near the end of a broad extensional zone next to a drainage trough (Fig. DR2A [see footnote 1]). In a second setting, a broad dome remained as a residual high flanked by subsidence troughs (Fig. 9A). Radial-striking grabens unroofed the dome until unit 3 was exposed in patches (Figs. 9B–9D). Because the stock was sapped by surrounding drainage trenches, it rose slowly and never fully emerged despite being large. In a third setting, a stock formed in a drainage pit (Fig. 10A). During a lull in drainage, unit 3 welled up diapirically from the side of the drainage pit where the overburden was thinnest (Fig. 10B). As the pit continued to drain, the stock sank from the floor of the pit along with landslides of the overburden (Figs. 10C and 10D). Appearance and disappearance of the diapir typified

[1]GSA Data Repository item 2011021, a movie (DR1) and five additional figures (DR2 to DR6); the time-lapse movie shows the map-view evolution of the physical model of the collapse of Hebes Chasma; its surface is lit from the north, is available at http://www.geosociety.org/pubs/ft2011.htm or by request to editing@geosociety.org.

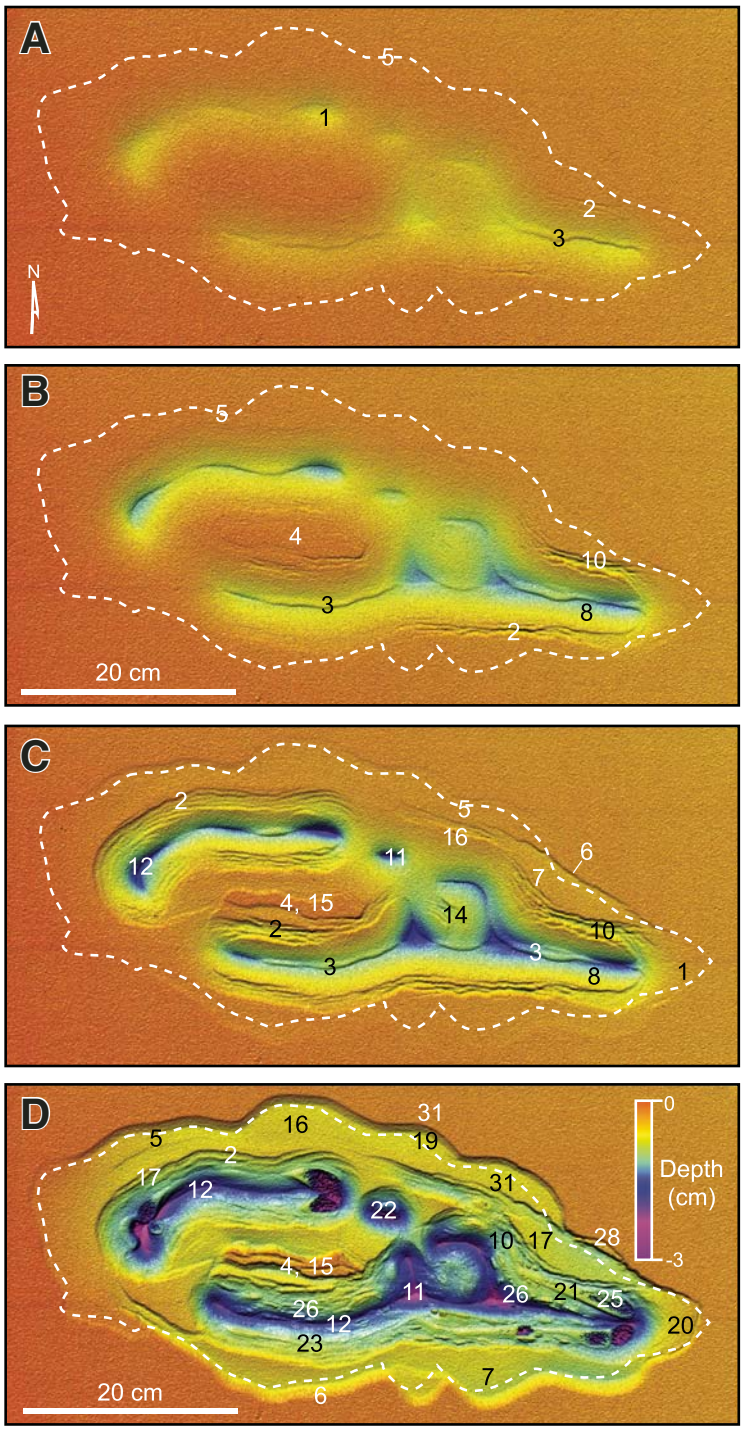

Figure 6. Evolution of subsidence in model 1 illustrated by laser-scan relief maps lit from the north. Key structures: 1—swale; 2—hinge graben; 3—axial thrust; 4—future mensa; 5—outer boundary of unit 3; 6—chasma-bounding normal fault; 7—outward-tilted extensional fault block; 8—inward-tilted slab of unit 1; 10—subsurface reactive diapir; 11—drainage pit; 12—drainage trench; 14—radial grabens in diapiric roof; 15—residual high; 16—downfaulted plains surface; 17—extensional terraces; 19—structural alcove; 20—arcuate extensional fault; 21—exposed diapiric wall; 22—exposed diapiric stock; 23—unit 2 exposed in landslide; 25—inward allochthonous flow; 26—chaotic landslide terrain; 28—slump off rim; 31—arcuate headscarp.

the delicate balance between buoyancy-driven upwelling and gravitationally driven subsidence. The disappearance of the diapir also underlines how difficult it is to picture early stages of subsidence at Hebes Chasma based on its present-day structure.

Drainage troughs acted like elongated sinkholes (Figs. 7 and 8). Some slabs remained cohesive even while they tilted steeply and gradually vanished down the drainage trough (Figs. 7C and 7D), but most tilted slabs of units 1 and 2 collapsed as particulate flows when shear stresses exceeded their shear strength (Fig. 7E). The excavated heads of the landslides further unroofed granular units 1 and 2. The landslides cascaded into trenches and covered older structures and stratigraphic layers. The landslides consisted of grains and rafts of reduced rhomboids. The result was a lumpy, chaotic topography (Figs. 7E and 7F). The pieces of units 1 and 2 cascaded down the sides of trenches and pits and disappeared. Arcuate normal faults curved around the upper ends of some drainage trenches as brittle units 1 and 2 continued to slide inward and extension spread outward (Fig. 7E).

In the outer parts of the chasma, the plains surface remained mostly intact, though downfaulted and tilted inward and outward (Fig. 6D).

Stage 4: Allochthonous Flow

As subsidence culminated, it transformed the inner part of the chasma (Figs. 11A and 11B). Landslides unroofed unit 2 and began to expose previously buried viscous diapirs that had risen from unit 3. Once exposed, diapirs extruded down the flanks of the drainage pits and trenches. These viscous allochthonous flows covered the terrain of chaotic landslides. Entrained within the viscous extrusions or carried above them, particle clumps of units 1 and 2 stretched into downslope-oriented streaks (Fig. 8A). Flows down opposite flanks of trenches approached, met, and sutured in the depths of some trenches. Linear sutures formed within linear trenches (Fig. 8B), whereas triple-point sutures formed where three trenches met (Fig. 9D).

Final Structural Zonation

Advanced subsidence in the model produced brittle and ductile structures in widely different states of strain. Broadly, subsidence increased from the outer rim inward to the nearest trench. Structures can be grouped into three zones, each having a different mix of structures that excavated the model chasma (Figs. 11B and 6D).

An outer zone had a structural fabric parallel to the chasma rim. Concentric extensional

faults suggest a response to inward viscous flow at depth (Fig. 7). Normal faults formed by brittle extension of units 1 and 2 accompanied inward viscous flow of unit 3 in the subsurface. Surface structures in the outer zone included normal faults along the rims, fault-controlled headscarps embaying the rim to form alcoves, fault-bounded benches, inward- and outward-tilted slabs of plains material, and slump-block terraces (Figs. 6D, 7E, and 8A).

An inner zone having fabrics oriented down-dip into the axial trenches and pits was dominated by inward and downward viscous flow at depth. Granular flows (landslides) and viscous flows (extrusions) stretched and aligned centripetal, flow-parallel streaks (Figs. 8 and 9). The fabric was one of extreme downslope extension parallel to the major principal axis of strain and extreme vertical shortening parallel to the minor axis, shaped like a flattened cigar. Surface structures in the inner zone included

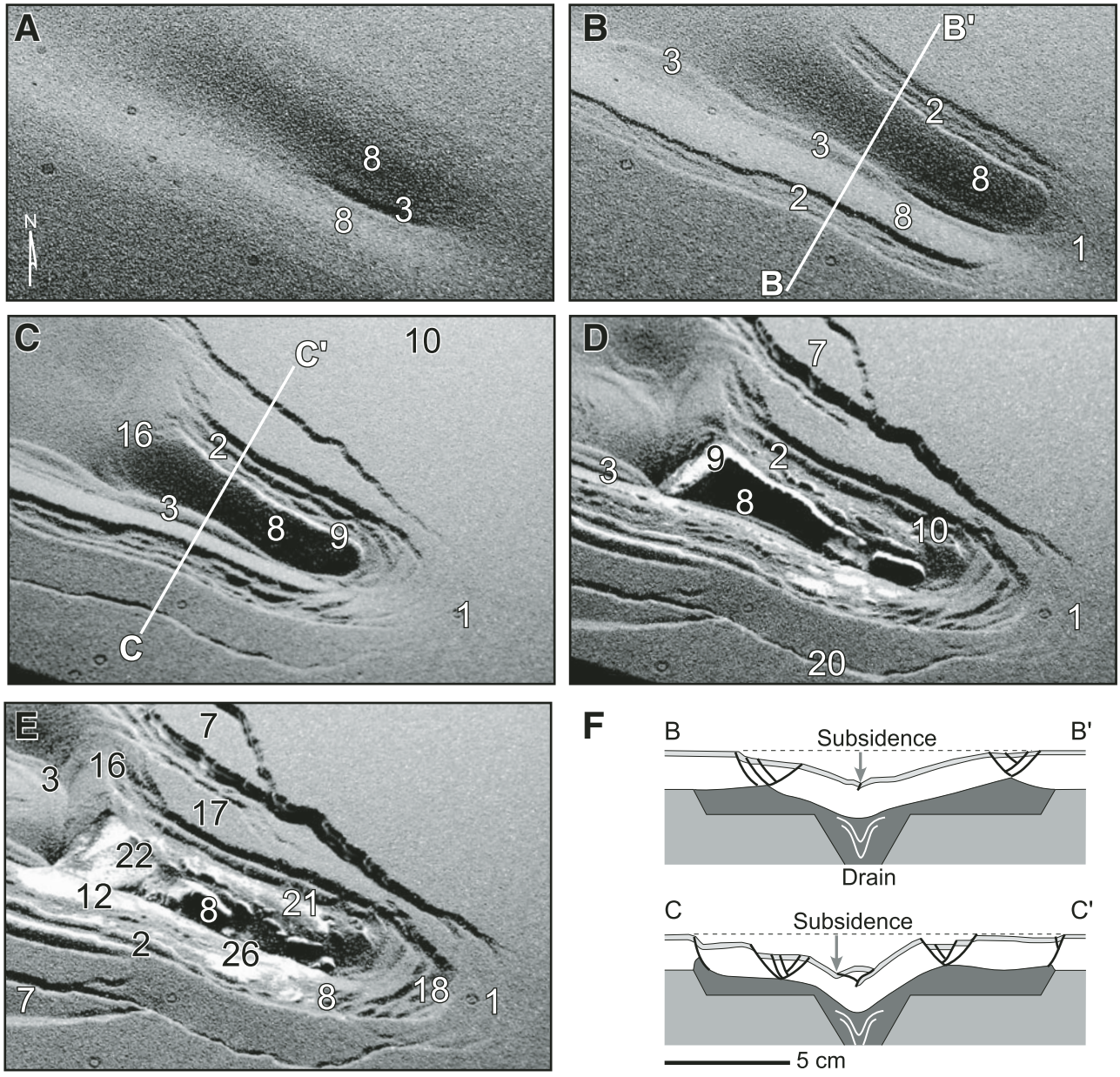

Figure 7. Surface structural evolution of the east end of model 1 during progressive collapse, illustrated by oblique photographs lit from the north; Figure 5 shows the location. (A–B) Stage 1 subsidence in the form of sagging. (C–E) Stages 2–4 of model subsidence, in which slabs subsided, broke apart, and disappeared, followed by allochthonous flow and diapir emergence. (F) Cross sections of the stages shown in B and C, based on surface structures and stratigraphic data. Key structures: 1—swale; 2—hinge graben; 3—axial thrust; 7—outward-tilted extensional fault block; 8—inward-tilted slab of unit 1; 9—extensional fault scarp exposing unit 2; 10—subsurface reactive diapir; 12—drainage trench; 16—downfaulted plains surface; 17—extensional terraces; 18—extensional rhombs; 20—arcuate extensional fault; 21—exposed diapiric wall; 22—exposed diapiric stock; 26—chaotic landslide terrain.

allochthonous viscous flows, trails of cohesive fragments parallel to flow, streaks of smaller clumps and entrained grains, and steep-sided drainage pits and trenches (Figs. 6D, 7E, 8A, 9, and 10).

A transitional zone acted as a broad hinge between the outer and inner structural zones, containing a concentric fabric parallel to the chasma rim (Fig. 11B). Extension was more advanced than in the outer zone. This zone includes the central mensa, which was degraded by extension on all sides and structurally unroofed. Surface structures in the transitional zone were fault-bounded benches, stretched inward-tilted slabs of plains material, fault lozenges, and reactive diapiric walls (Figs. 6D, 7E, 8, 9, and 10).

All three stratigraphic units deformed and moved inward toward the drainage pits and trenches in patterns depending on the location of the nearest pit or trench. Some structures migrated through more than one structural zone as subsidence progressed.

Diapirism and Extension in Hebes Mensa

In model 1, the equivalent to Hebes Mensa was a residual horst, which remained high as its surroundings subsided. The result was a flat plateau flanked by grabens (Fig. 12A). The mensa could not rise because it rested on rigid basement. In contrast, the mensa in model 2 was underlain by buoyant mobile unit 3. As a result, the core of the mensa rose diapirically. At the same time, extension thinned the mensa's roof, compensating for diapiric rise. Accordingly, the summit of the mensa remained just below the chasma rim, as seen in Hebes Mensa. The two profiles in Figures 12A and 12B show the difference between (1) pure extension in model 1, where a flat mensa crest is level with the plains, and (2) a mixture of diapirism and extension in model 2, where the arched mensa crest is slightly below plains level.

At the stage shown in Figure 12B, the diapir was still deep below its arched roof. After more chasma subsidence however, the mensa diapir continued to rise reactively and eventually emerged at the summit of the mensa (Fig. 12C).

GEOLOGY OF HEBES CHASMA

Introduction and Geologic Map

We analyzed the models while studying images of Hebes Chasma and preparing a geologic-geomorphic map built on the rich reservoir of images and measurements of Mars acquired by spacecraft over decades. Figure 13 is a composite of our more detailed maps. Unlike geologic mapping on Earth, where ground can be directly examined, remote mapping of planets must be based mainly on interpretation of landforms, roughness, albedo, and spectral reflectance. In keeping with the established practice of interpreting planetary geology from remote measurements, our "geologic" map includes geomorphic units such as surfaces and benches. Table 3 describes and interprets the map units, which are modified from Adams et

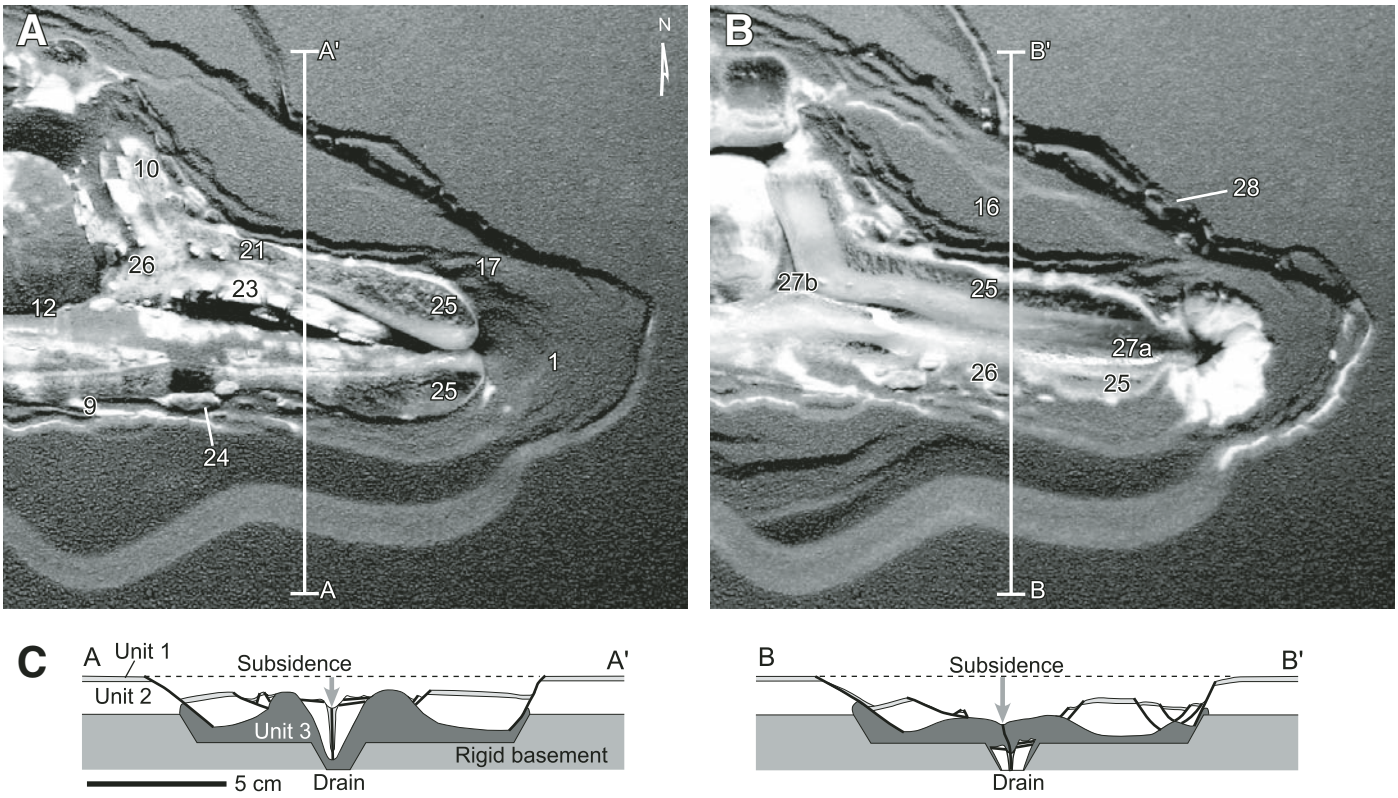

Figure 8. (A–B) Surface structural evolution of the east end of model 1 during stages 2–4 of model subsidence in which diapiric walls emerged, extruded, and sutured their allochthonous flows in drainage troughs. (C) Cross sections of the stages shown in A and B, based on surface structures and stratigraphic data. Overhead photographs are lit from the top; Figure 5 shows the location. Key structures: 1—swale; 9—extensional fault scarp exposing unit 2; 10—subsurface reactive diapir; 12—drainage trench; 16—downfaulted plains surface; 17—extensional terraces; 21—exposed diapiric wall; 23—unit 2 exposed in landslide; 24—rafted fragment of extensional lozenge; 25—inward allochthonous flow; 26—chaotic landslide terrain; 27a—linear suture; 27b—triple-point suture; 28—slump off rim.

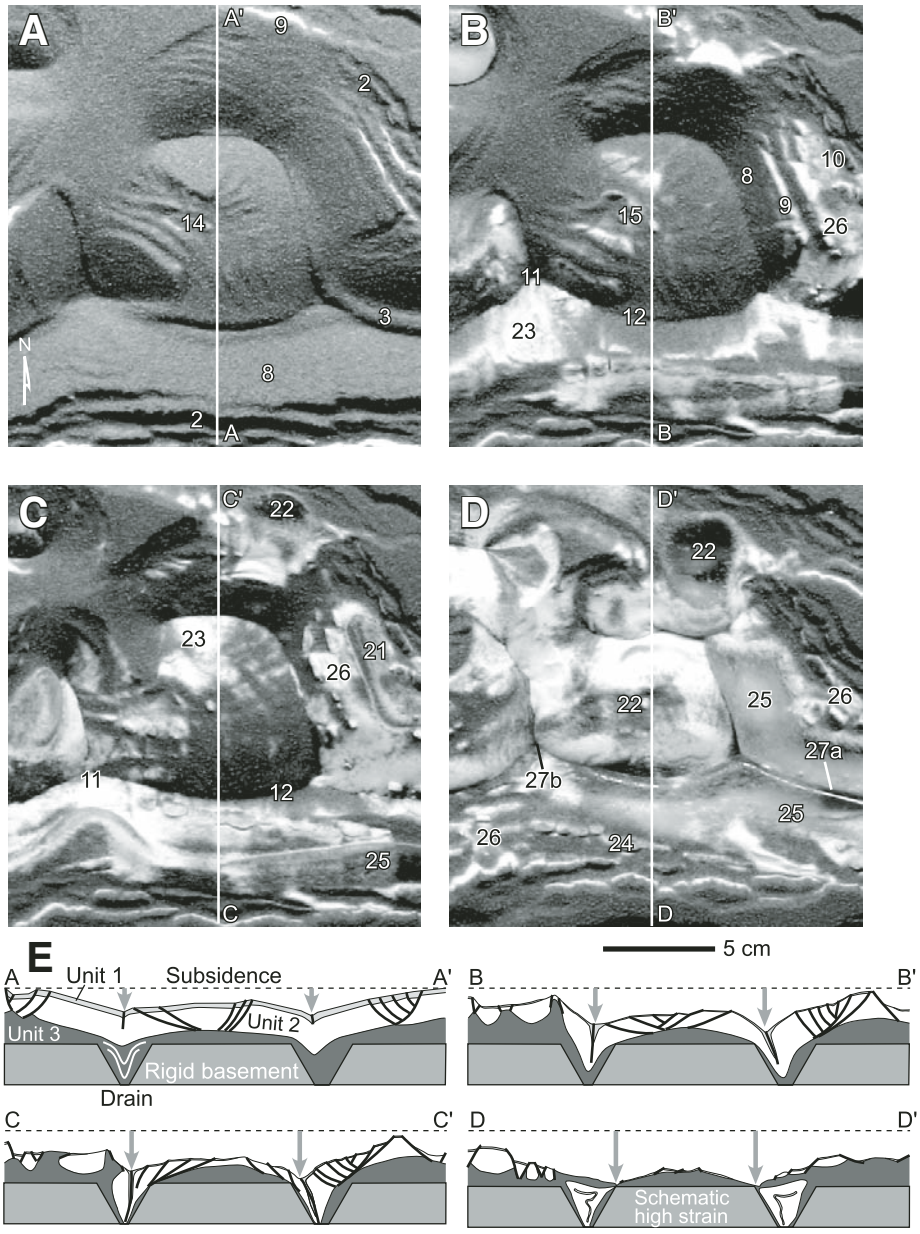

Figure 9. (A–D) Surface structural evolution of the center of model 1 during stages 2–4 of model subsidence in which diapiric stocks were unroofed and partially emerged, forming a residual high between drainage troughs. (E) Cross sections of the stages shown in A to D, based on surface structures and stratigraphic data. Overhead photographs are lit from the top; Figure 5 shows the location. Key structures: 2—hinge graben; 3—axial thrust; 8—inward-tilted slab of unit 1; 9—extensional fault scarp exposing unit 2; 10—subsurface reactive diapir; 11—drainage pit; 12—drainage trench; 14—radial grabens in diapiric roof; 15—residual high; 21—exposed diapiric wall; 22—partly exposed diapiric stock; 23—unit 2 exposed in landslide; 24—rafted fragment of extensional lozenge; 25—inward allochthonous flow; 26—chaotic landslide terrain; 27a—linear suture; 27b—triple-point suture.

al. (2009). Figure 14 shows the location of all Hebes illustrations.

A valuable marker for interpreting structures of the chasma walls was the base of the Upper Hebes Formation, which forms an uneven contact with the Lower Hebes Formation (Fig. 13). The Upper Hebes Formation probably formed diagenetically by cementation of preexisting materials of various ages to a depth of 600–800 m below the plains surface (Treiman et al., 1995; Adams et al., 2009). A diagenetic origin is not consistent with flood-basalt flows (McEwen et al., 1999). The resistant outcrops of the Upper Hebes Formation at various levels within the chasma dropped from near the original plains surface during subsidence.

Initial Subsidence (Stage 1): Sagging, Minor Extension, and Thrusting

At the eastern end of Hebes Chasma, there is a gentle sag of the plains surface called the "Swale" by Adams et al. (2009) (Figs. 1B and 15). The Swale is 18 km long, 10 km wide, and up to 750 m deep. Inward-tilted slabs hinge on a rim of grabens, and the deep axis of the sag is ridged. The Swale aligns with the axis of Hebes and with Ganges Catena, a chain of pits and troughs 148 km farther east (Fig. 1A). The Hebes-Ganges linearity and alignment suggest control by a regional fracture zone.

Adams et al. (2009) proposed that the Swale records an immature stage of subsidence as the chasma propagated eastward. Similar structures formed in model stage 1 (Figs. 6A, 7A, and 7B), but they were destroyed as subsidence continued. Preservation of the Hebes Swale therefore suggests that further subsidence stopped there. In the models, peripheral shallow grabens formed at the hinge of the inward-tilted plains surface, and inward-moving slabs overrode one other as thrust faults as they converged along the axis. The models support the interpretation that wrinkle ridges in the Hebes Swale are the surface expression of folds above blind thrust faults. This axial shortening in the model balances extension in the margins. Radial wrinkle ridges at the end of the Hebes Swale show that slabs converged by sliding radially inward (Fig. 15).

Extensional Collapse (Stages 2 and 3): Bench Subsidence, Inward Tilting, and Landsliding

Extensional Benches

As in the model, extension along the margins of Hebes Chasma formed gently sloping (<10°) fault-bounded benches that tilt both inward and outward. At the east end of the chasma, the inner

edges of the benches expose the same layered unit (Upper Hebes Formation) that forms the rimrock on the walls above, showing that the plains surface was down-faulted (Fig. DR3 [see footnote 1]). In Hebes cross sections, eroded bedrock and talus can be balanced only if faults defining the benches dip inward.

Extensional faulting also produced an isolated 17-km-wide bench of the Upper Hebes Formation on the north wall called "Big Slab" (Adams et al., 2009) (Fig. 16A). This slab has two pieces: an upper, narrow bench dipping 1° outward and a larger, lower bench dipping 9°–10° inward. The toe of the lower bench has transverse (strike-parallel) shallow grabens and ends in a fault scarp above the North Pit, which resembles scarps exposing layered Upper Hebes Formation at the edges of benches above the East Pit.

About half the chasma walls consist of fault blocks tilted at 15°–25° and carved into the ridges and gullies characteristic of the LHF_l (Lower Hebes Formation incised by gullies) (Fig. 16A). Pervasive strike-parallel faulting of these blocks shattered the plains surface and the resistant Upper Hebes Formation cap. Faulting exposed the more readily eroded Lower Hebes Formation in gullies and left scattered remnants of basal Upper Hebes Formation on ridges and on some block edges where dips are at angles close to the slopes of the walls. The ridge-and-gully blocks differ from the benches in lacking prominent headwall fault scarps.

The models produced similar inward-tilting wall blocks without headwalls (Figs. 7B–7D) when deep subsidence removed support. Slabs in the models formed early, but the walls faulted pervasively only after advanced tilting and breakup of the surface layer (Figs. 7, 8, and 10). Steep slabs were then engulfed whole or fragmented in drainage troughs. Because the models did not include surficial erosion, they did not produce incised landforms similar to the gullied topography of the LHF_l in Hebes.

A tilted fault block of wall material, here named "Island Block," projects from the eastern floor of the chasma (Fig. 16B). The north side of Island Block is an ~25° dip slope of lower Upper Hebes Formation strata. The block's southern scarp slope exposes the lower third of Upper Hebes Formation and some Lower Hebes Formation below. The northward tilt of Island Block and the trench between it and the south wall of the chasma are consistent with extension caused by subsurface removal of material along the chasma's axis (Fig. 16B). Similar tilted and rafted blocks appear at various stages in the models (Fig. 7). We interpret the low hills at the northern base of Island Block as a landslide of delaminated upper Upper Hebes Formation, which slid down the crest of the block. On Island Block and on the ridge-and-gully (LHF_l) chasma walls, the upper part of the Upper Hebes Formation fell apart on slopes steeper than 20°. In contrast, Upper Hebes Formation on the benches, which slope at less than 10°, remained largely intact, although it is possible that the southern flank of Big Slab (9°–10° dip) also delaminated. So when Hebes Chasma formed, the Upper Hebes Formation may have been less cohesive than its counterpart in the models.

A spectacular terrestrial analog for pervasive faulting and inward tilting caused by subsidence is the collapse of the Vatnajökull ice cap in Iceland during a 2 wk subglacial eruption in 1996 (Gudmundsson et al., 1997). Eruption from a fissure connecting two volcanoes melted 3 km^3 of ice, which ponded in a subglacial lake before bursting out as a jökulhlaup flood. After meltwater escaped, the overlying ice collapsed to form intensely crevassed ice cauldrons that rapidly deepened to several hundred meters and widened extensionally to several kilometers (Fig. 17A).

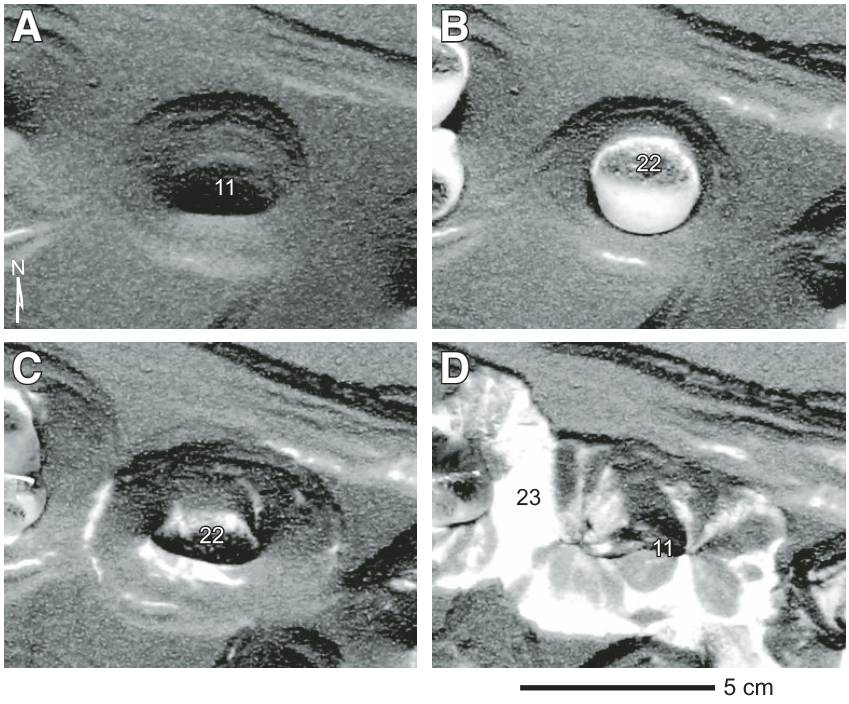

Figure 10. Surface structural evolution of the center of model 1 during stages 2 and 3 of model subsidence, in which a diapiric stock emerged in a drainage pit and then disappeared as pit walls slid inward. Overhead photographs are lit from the top; Figure 5 shows the location. Key structures: 11—drainage pit; 22—exposed diapiric stock; 23—unit 2 exposed in landslide.

Bench Disaggregation and Landsliding

The west wall of the chasma has narrow fault benches just below the rim and normal faults at the headwall that extend into the plains surface as shallow grabens (Fig. DR4 [see footnote 1]). These arcuate grabens subparallel to the headwall may be influenced by larger fault sets (Echus Fossae or Tithoniae Fossae), or they may be cross faults orthogonal to the main border faults (Wilkins and Schultz, 2003), but they certainly controlled collapse of the chasma's blunt west wall. Below the fault benches, the chasma's western wall consists of a chaotic block (mapped as LHF_s (slumped Lower Hebes Formation) in Fig. 13) different from the ridge-and-gully topography. Resistant remnants of the lower part of the Upper Hebes Formation protect ridges within the LHF_s, and the apparent dip of these remnants steepens downslope into the West Pit. Along its southern boundary, material of the chaotic block overlies ridges and gullies of the adjacent wall (Fig. 13). Along its northern boundary, the block coincides with a change in direction of a major gully. The chaotic topography of the block suggests massive landslides into the subsiding West Pit.

A terrestrial example of foundering extensional fault blocks that broke apart during subsidence is the sink holes produced by dissolution of underlying salt along the margin of the Dead Sea, Israel (Fig. 17B). Detached fault

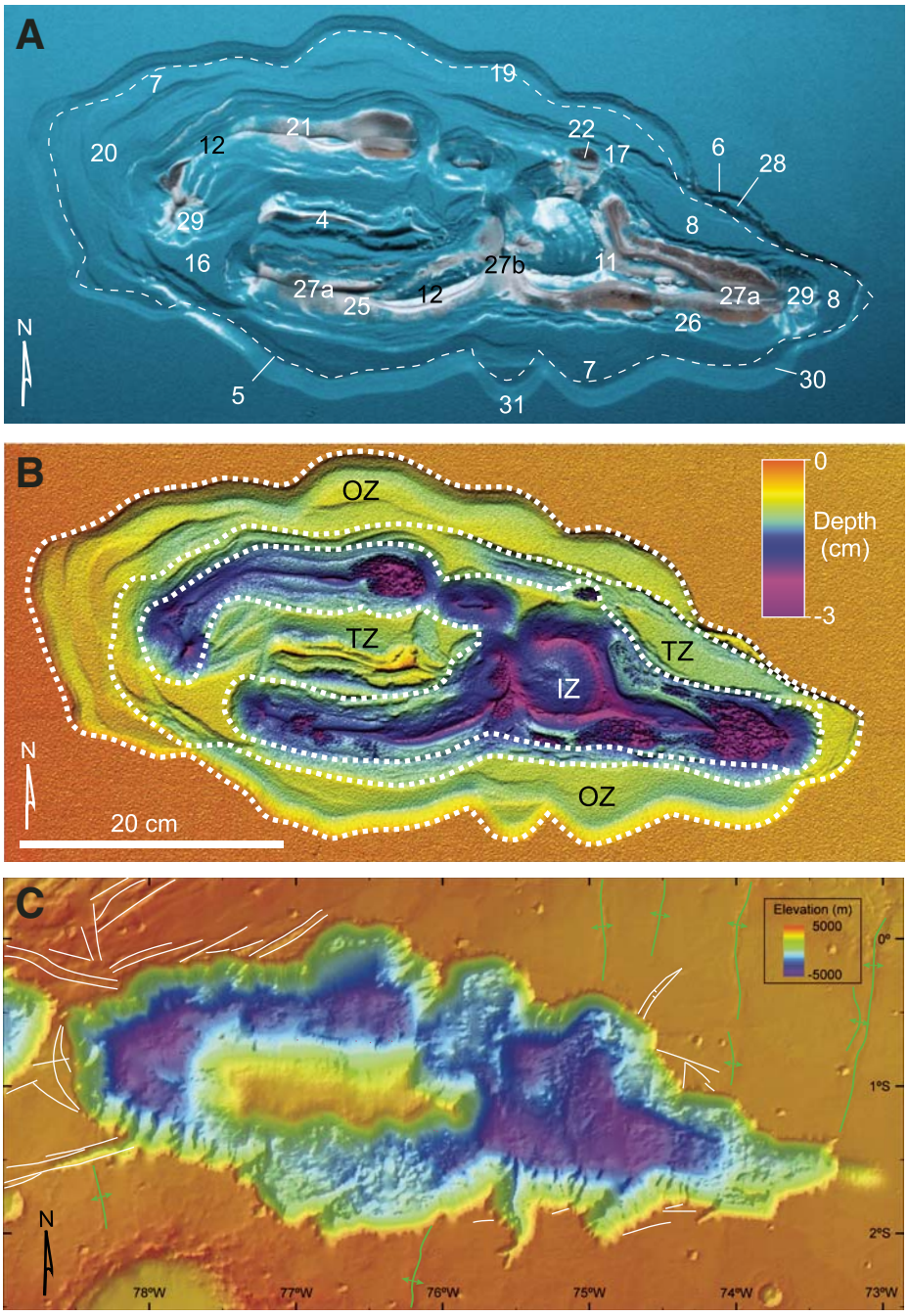

Figure 11. (A) Overhead photograph lit from the north showing key structures in the model in stage 4: 4—mensa; 5—outer boundary of unit 3; 6—chasma-bounding normal fault; 7—outward-tilted extensional fault block; 8—inward-tilted slab of unit 1; 11—drainage pit; 12—drainage trench; 16—downfaulted plains surface; 17—extensional terraces; 19—structural alcove; 20—arcuate extensional fault; 21—exposed diapiric wall; 22—exposed diapiric stock; 25—inward allochthonous flow; 26—chaotic landslide terrain; 27a—linear suture; 27b—triple-point suture; 28—slump off rim; 29—landslide; 30—talus slope; 31—arcuate headscarp. (B) Laser-scan topographic map showing final structural topography and zonation lit from the north: OZ—outer zone, TZ—transitional zone, IZ—inner zone. (C) Hebes topographic map showing grabens (white) and wrinkle ridges (green) in surrounding plains. Mars Orbiter Laser Altimeter data.

blocks dip both inward and outward on extensional fault surfaces. The deepest fault blocks sank into salty mud as they broke apart to form a chaotic terrain of irregular foundered blocks.

Diapiric Emergence (Stages 2 and 3)

The most readily recognized diapirs are pale mounds that project upward through younger deposits in the floor of Hebes Chasma (Fig. 18). One of the largest exposed diapirs is Mini-Mensa, an 8-km-long oval mound east of Hebes Mensa (Fig. 19A). The pale crest and upper flanks of Mini-Mensa are highly fractured. At lower elevations, outward-dipping layers of the LHF_L (layered Lower Hebes Formation), interpreted by the Rule of V, define an antiform. This collar of upturned layers is distinctive of active salt diapirs on Earth (Fig. 19B). The domal structure of Mini-Mensa and of its equivalent in the model implies that as the surrounding troughs sank, Mini-Mensa rose diapirically because its roof thinned as material slid or flowed into the surrounding troughs and pits.

A smaller, but even more prominent, diapiric mound projects from the floor of the North Pit northwest of Hebes Mensa (Figs. 18 and 20A). This pale hill shaped like a tear drop is fluted and faceted by wind erosion. A flap next to its east flank tilts gently away from the diapir, as around Mini-Mensa and terrestrial active diapirs (Fig. 19B). Mounds form low conical or rounded hills elsewhere in the North Pit and in the Southeast Pit (Fig. 18), and many of them are within a region of the North Pit having the spectra of kieserite (Adams et al., 2009). Wrinkled mounds are present on the floor of the graben south of Island Block (Fig. 16B). We interpret the mounds as viscous extrusions of the Lower Hebes Formation from reactive diapirs triggered by graben opening, similar to reactive upwelling of unit 3 in grabens in the model (Fig. 8A).

The competition between gravity-driven rise (diapirism) and gravity-driven fall (subsidence) in the model highlights two lessons. First, underlying flows can carry a diapir laterally into a drainage trough (Fig. DR2, diapir 22 [see footnote 1]), where the diapir sutures with other diapirs before draining away. Second, a diapir can appear and disappear in the same place. A diapir rose in a drainage pit where the overburden was thinnest (Figs. 10A and 10B), and then sank out of sight as the pit continued to drain (Figs. 10C and 10D). Some diapirs that rose while Hebes Chasma subsided might therefore have drained away later—another reminder that the present-day structure is an incomplete picture.

Like many salt diapirs exposed subaerially on Earth, the Hebes mounds have an outer margin that is smooth and oval, a profile that is smooth

and rounded, and a texture that is scaly or lumpy like cauliflower (Figs. 19B and 20A). After rising to the surface, terrestrial salt diapirs degrade by erosion and dissolution. As a result, to remain as a hill, they must continue to rise (Fig. 19B). Their relief signifies ongoing rise on Earth but need not on a Mars, where erosion is far slower. The cauliflower texture of subaerial terrestrial diapirs (Fig. 19B) forms as halite dissolves, leaving a mantle of gypsum-rich soil created by hydration of anhydrite grains in the halite host rock (Jackson et al., 1990; Bruthans et al., 2008). In contrast to the cauliflower texture, the shaggy textures on the lower slopes of Hebes Mensa resemble the jagged weathering of anhydrite diapirs in an arid polar climate etched by dissolution and wind (Fig. DR5 [see footnote 1]; Harrison and Jackson, 2008). Although halite is the most common mineral in terrestrial salt bodies, other salts having different properties are known on Mars. Potash salts are even weaker than halite, and some salts, such as epsomite, are even less dense than halite. There are few clues to the composition of the allochthonous flows in Hebes Chasma. Accordingly, our analogies of Hebes landforms with halite salt structures on Earth are only meant to draw parallels with their geomorphology and distinctive deformation style, without implying that the Hebes diapirs and flows consist mostly of halite.

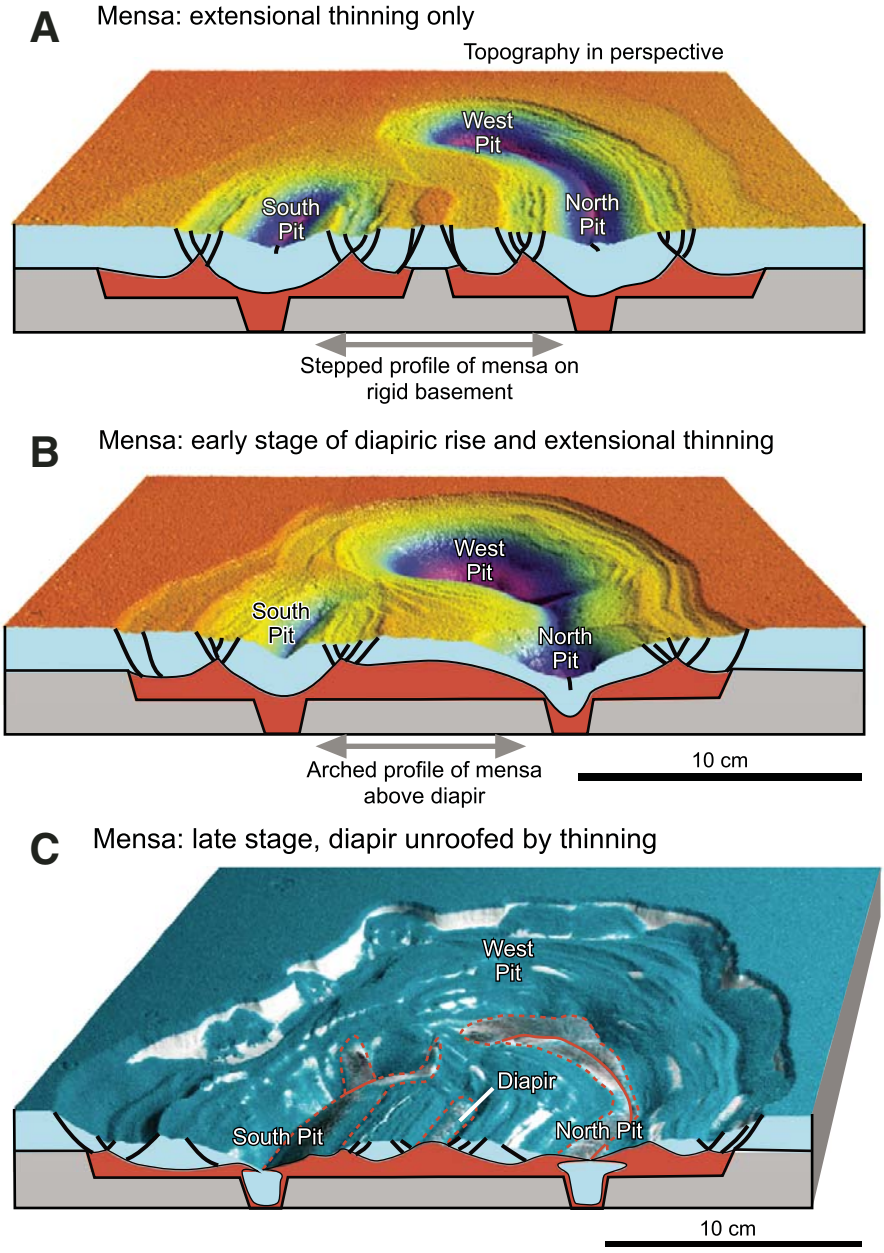

Figure 12. Perspective views of laser scans from models viewed to the west comparing (A) shape of a mensa produced by extension in model 1 with (B) shape of a mensa produced by both diapirism and extension in model 2. (C) Oblique photograph viewed to the west showing a diapir that emerged at the crest of the mensa after more advanced subsidence in a twin model to model 2. Cross sections are based on surface structures and stratigraphic data. Model is lit from the right (north); Figure 5 shows the location.

Allochthonous Flows (Stages 3 and 4)

Some features mapped in Figure 18 have been interpreted by others as landslides (e.g., Witbeck et al., 1991). Landslides have undoubtedly occurred, but we interpret most of the largest features as allochthonous flows on the basis of evidence summarized in a later section, "Landslides, Magma, Ice."

Deep-Sourced Flows Associated with Collapse

The largest flows in Hebes Chasma, here referred to as the Great Flows, emerged from the chasma walls (Figs. 1B and 18). These are the North Flow (50 km long), the Northeast Flow (70 km long), and the Tongue (45 km long) (Adams et al., 2009). All flowed toward the deepest depressions in the floor.

The Tongue follows the axis of the east-end trough and slopes at ~4° westward to the East Pit (Figs. 18 and 21). The Tongue is bounded by fault scarps to the north and south and is broken by transverse scarps. The gradual transition of the east benches (WB_F) into the upper part of the Tongue, and the absence of a single, prominent headwall detachment zone suggest that the flow consists largely of the Lower Hebes Formation. This interpretation is consistent with the physical models in which deep material emerged at the surface along both sides of the east trough and began to flow along the chasma axis (Fig. 8).

The North and Northeast Flows reach deep pits with flow gradients of 3° and 2°, respectively. The heads of each flow are in troughs bounded by fault scarps including arcuate headwalls capped by horizontal Upper Hebes Formation (Figs. 18 and 22A). Above the sides of the Great Flows, inward-dipping slabs of LHF_I capped by the lower Upper Hebes Formation are exposed in lateral fault scarps (Fig. 22A). The Great Flows thus occupy structural troughs similar to that confining the Tongue.

The first sign of breakout of an allochthonous flow is bulbous mounds near the base of the chasma walls (Fig. 22B). The mounds either never fully emerged or oozed only a few kilometers over older flows, before stiffening, and

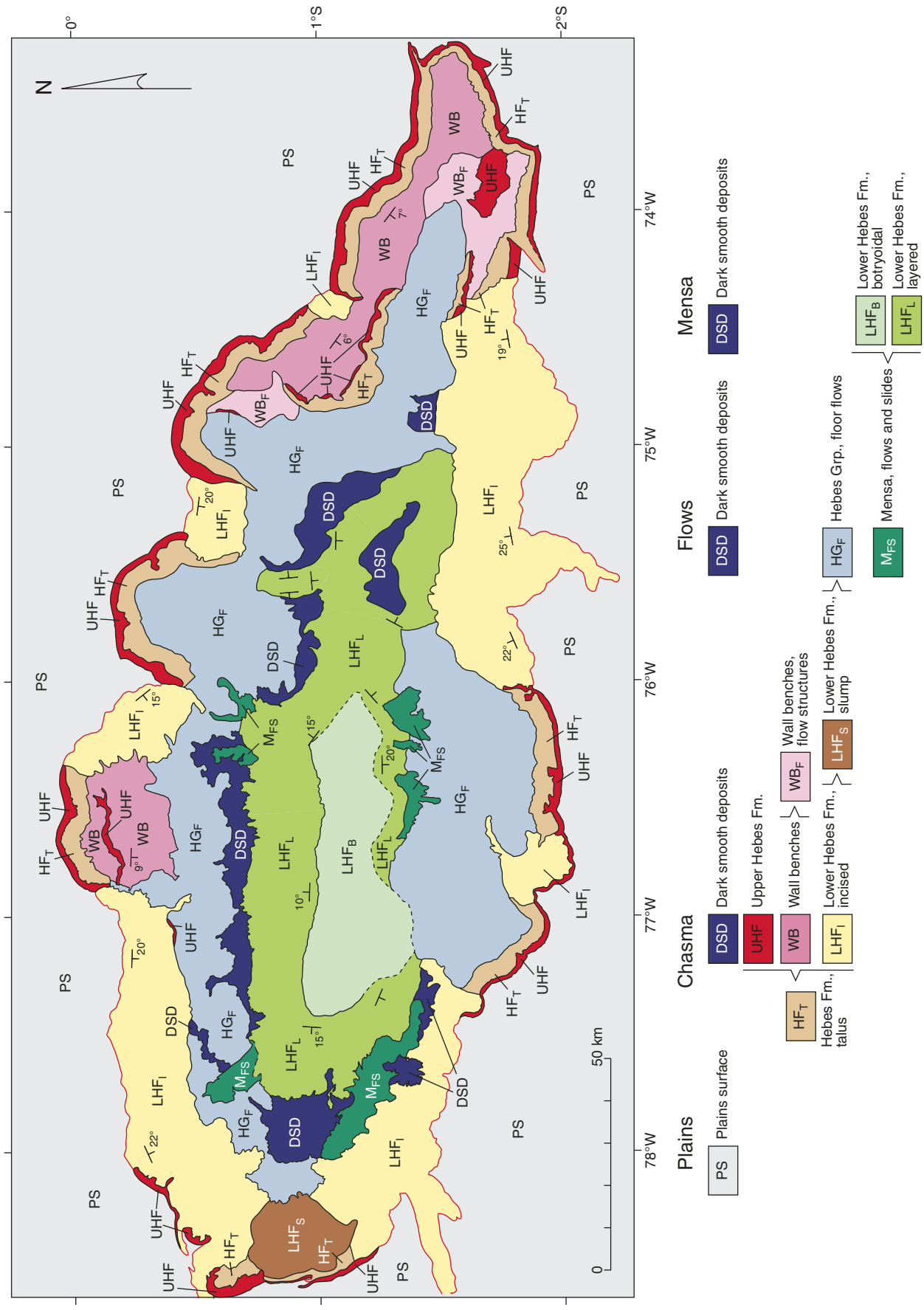

Figure 13. Geologic map of Hebes Chasma produced by photogeologic interpretation. Table 3 provides a detailed legend.

becoming immobile. In the area shown in Figure 22B, three discrete flows overlie older flows, impinging to produce several generations of refolded folds. The Great Flows are composites of smaller flows, many of which merged laterally (Fig. 18) and even sutured head to head, as in the model (Fig. 8B).

Morphologies of the termini of the small flows in the chasma provide further clues to flow mechanics. Some small flows end in a lobate escarpment, suggesting that viscosity increased and immobilized flow, perhaps by cooling or loss of pore fluids. Others end as a thinning wedge, like an ice glacier ablating or a salt glacier dissolving. More rarely, snouts end in a moat, as if the end of the flow had melted, ablated, or dissolved.

We interpret the Great Flows as a fundamental part of Hebes collapse, as in the physical models where subsidence and breakaway sliding of rafted fault blocks progressively sapped the chasma wall and exposed its mobile depths. In the models, flows consisted of the two deeper units with entrained pieces of the youngest unit. We infer that the three Great Flows also originated at depth and consist chiefly of the allochthonous Lower Hebes Formation with entrained Upper Hebes Formation relics.

Several features suggest that material began flowing at depth before emerging as lateral extrusions (Fig. 22). First, there is no bergschrund or other breakaway gap, which results when a glacial flow separates from a fixed uphill boundary such as a cliff. Second, the bulging mounds along the base of the headscarps of the Great Flows suggest that flows welled up from depth without signs of dribbling from above. Third, some flows appear to have emerged from the base of the chasma walls fully formed because their flow-parallel striae suggest viscous longitudinal extension (Fig. 22B). These striae could result from elongation of inclusions by subsurface flow or from shredding of the foot of the talus apron by traction of underlying flow. Surfaces of flows commonly have a

TABLE 3. DESCRIPTIVE LEGEND FOR GEOLOGIC MAP UNITS OF HEBES CHASMA

Major units	Minor units
Plains	**PS** Plains surface *Description*. Part of the Hesperian-age plateau of the Valles Marineris region (McEwen et al., 1999). **PS** is an extensive geomorphic surface defining the top of the Upper Hebes Formation.
Hebes Group: Upper Hebes Formation	**UHF** Upper Hebes Formation *Description*. Layered, resistant unit rimming the chasma, edges of benches in chasma walls, tilted blocks in the east floor of the chasma, and ridges of $\mathbf{LHF_I}$. On the chasma rim, the plains surface (**PS**) caps the **UHF**; the base of **UHF** grades into underlying softer, massive (nonlayered or cryptically layered) $\mathbf{LHF_T}$ and $\mathbf{LHF_I}$. Layers in **UHF** vary in resistance, albedo, and thickness (<5 to 100 m). The **UHF** unit is 500–800 m thick, but its base is uneven and, in places, poorly defined. *Interpretation*. Diagenetically formed cap locally discordant to underlying strata (Treiman et al., 1995; Adams et al., 2009). **UHF** is cemented and altered LHF. Outcrops of **UHF** below the chasma rim are remnants of the rim displaced by faulting, tilting, and sliding.
	WB Wall benches *Description*. Level or inward-tilted (<10°) surfaces below upper walls of **UHF** and $\mathbf{LHF_T}$ in the east and north. On the northeast wall, **WB** exposes layers of **UHF** on inward-facing slopes. In the east, **WB** is largely dust-free and hummocky, pitted by etched, degraded craters, some of which may be relics of former plains surface. *Interpretation*. **WB** consists of remnants of **UHF** and plains surface (**PS**) that subsided by normal faults along the chasma rim. In the east, sagging along an east-west axial zone and shallow thrusting deformed **UHF** into hummocks.
	$\mathbf{WB_F}$ Wall benches having flow structures *Description*. $\mathbf{WB_F}$ is present at the east end of the chasma between outcropping **WB** and $\mathbf{HG_F}$. Surfaces of $\mathbf{WB_F}$ show flow lobes, coarse ropy wrinkles, fine wrinkles, longitudinal flow ridges, and large hummocks. $\mathbf{WB_F}$ has sparser impact craters than does **WB**. In the east, lobate flows of $\mathbf{WB_F}$ overlie **WB**. Mobile $\mathbf{HG_F}$ intruded a bench of $\mathbf{WB_F}$ below the northeast wall. Layers of **UHF** crop out on the edges of $\mathbf{WB_F}$ benches on the northeast wall and south wall; the northward-dipping Island Block of **UHF** lies within $\mathbf{WB_F}$ near the southeast wall. *Interpretation*. $\mathbf{WB_F}$ is transitional between **WB** to $\mathbf{HG_F}$. Delamination, disaggregation, and softening mobilized **UHF**. Island Block is a **UHF** relic tilted and rafted northward by mobile **LHF** subsiding into the eastern axial zone of the chasma. The trough south of Island Block is a graben in which **WB** was mobilized to form hummocky $\mathbf{WB_F}$.
Hebes Group: Lower Hebes Formation	$\mathbf{HF_T}$ Hebes Formation, talus *Description*. Exposed in fault scarps along the chasma walls below outcrops of **UHF**. $\mathbf{HF_T}$ forms streaks and narrow fans on slopes of 20°–30°. Minimal deposits accumulated at the bases of talus slopes. Talus aprons are uninterrupted by ledges or layers. *Interpretation*. $\mathbf{HF_T}$ consists of noncohesive particles derived by mass wasting of nonlayered (or cryptically layered), relatively soft **LHF** and disaggregated **UHF**.
	$\mathbf{LHF_I}$ Lower Hebes Formation, incised *Description*. Chasma walls consisting mostly of nonlayered or cryptically layered Lower Hebes Formation eroded into ridges and gullies. **UHF** forms the chasma rim at the top of $\mathbf{LHF_I}$, and remnants of **UHF** cap ridges within $\mathbf{LHF_I}$ even in lowest parts of chasma walls. In the south, canyons incised into plains surface (**PS**) continue across $\mathbf{LHF_I}$ as gullies down to the chasma floor. Most debris removed from plains canyons and from gullies is not present on the chasma floor. *Interpretation*. $\mathbf{LHF_I}$ is the upper part of **LHF** exposed where overlying **UHF** was breached. $\mathbf{LHF_I}$ was displaced inward along the chasma walls by normal faulting during subsidence.
	$\mathbf{LHF_S}$ Lower Hebes Formation, slump *Description*. $\mathbf{LHF_S}$ on the west wall of the chasma is separated from **UHF** and $\mathbf{HF_T}$ on the rim by normal faults. $\mathbf{LHF_S}$ has transverse ridges and gullies and consists of fault blocks of $\mathbf{LHF_I}$ capped by remnants of **UHF**. $\mathbf{LHF_S}$ extends downslope to the West Pit without its toe thickening on the chasma floor. *Interpretation*. $\mathbf{LHF_S}$ is a slump caused by collapse of **UHF** and **LHF** in the west wall into the West Pit. Crowding within the slump caused it to laterally override ridges and gullies to north and south. Debris drained from the slump's toe into the West Pit.
	$\mathbf{LHF_B}$ Lower Hebes Formation, botryoidal *Description*. Discontinuous layered deposit (about 100 m thick) containing botryoidal structures. Caps Hebes Mensa and occurs locally near the top of Mini-Mensa (latter outcrops are too small to show on the geologic map).
	$\mathbf{LHF_L}$ Lower Hebes Formation, layered *Description*. Finely layered, generally pale, locally contorted and fragmented at kilometer scale. $\mathbf{LHF_L}$ underlies $\mathbf{LHF_B}$ on Hebes Mensa and Mini-Mensa. On both mensae, layering defines a gentle antiform. Below Mini-Mensa, $\mathbf{LHF_L}$ crops out in the Southeast Pit. Kieserite has been measured spectroscopically in layered deposits of the Southeast Pit (Gendrin et al., 2005; Adams et al., 2009). $\mathbf{LHF_L}$ is in fault contact with $\mathbf{LHF_I}$ at the base of the chasma's south wall. *Interpretation*. $\mathbf{LHF_B}$ and $\mathbf{LHF_L}$ are layered equivalents of the lower part of **LHF** in chasma walls. Botryoidal structures of $\mathbf{LHF_B}$ are kilometer-scale nested diapirs or fluid-escape cells of eruptive spring deposits. Layering in $\mathbf{LHF_L}$ may be depositional or may result from shear and flow segregation. $\mathbf{LHF_B}$ and $\mathbf{LHF_L}$ rose to their present positions on Hebes Mensa and Mini-Mensa by diapiric uplift.

(*Continued*)

TABLE 3. DESCRIPTIVE LEGEND FOR GEOLOGIC MAP UNITS OF HEBES CHASMA (*Continued*)

Major units	Minor units
Flows, slides, surficial deposits	**M_{FS}** Mensa, flows and slides *Description*. Unit includes pale tongues having lobate ends and arcuate transverse ridges. **M_{FS}** originates on slopes of Hebes Mensa and reaches the floors of surrounding trenches and pits. *Interpretation*. **M_{FS}** is derived from **LHF_B** and **LHF_L**. Flows and slides of **M_{FS}** are younger than underlying floors of trenches and pits. Flows on the southwest side of Hebes Mensa embay gullies in **LHF_I** and so postdate large gullies on the southwest wall, including the gully leading into the southwest plains canyon.
	HG_F Hebes Group, floor flows *Description*. (a) In the east **HG_F** consists of three large, low-gradient (2°–4°) flows (Tongue [45 km], Northeast Flow [70 km], and North Flow [50 km]) that terminate in closed depressions in the depths of the chasma. Normal faults bound upper sidewalls of the three large flows. The Tongue and the Northeast Flow grade into mobilized **WB_F**. (b) In the northwest, **HG_F** consists of multiple, kilometer-scale flows from the bases of chasma walls and from Hebes Mensa that end in closed depressions of the North Pit. In the west, flows from Hebes Mensa and the base of chasma walls converge on the West Pit. In the South Basin, **HG_F** forms a hummocky surface darkened by surficial deposits and filled by flows from the bases of the south chasma wall and Hebes Mensa. *Interpretation*. (a) Upper parts of the three large eastern flows of **HG_F** are interpreted as former benches (**WB** and **WB_F**) that foundered into or were transformed into mobile **LHF**. Flows consist primarily of **LHF**; any admixed **UHF** is mostly no longer recognizable. Along the sides of flows, subsidence produced normal-fault scarps, which shed additional sediment toward axial drains. At the toe of flows, the shape and drainage capacity of pits determined the directions and gradients of **LHF** flows. (b) Flows of **HG_F** from chasma walls extruded from reactive diapirs of **LHF** that welled up as the lower parts of chasma walls extended inward toward a free surface created by chasma collapse. Once these diapirs were sufficiently unroofed, their extrusions of mobile **LHF** drained into pits. Flows from lower parts of Hebes Mensa also contributed mobilized **LHF_L**, which advanced as viscous or granular flows. Flows from Hebes Mensa postdate gullies in the chasma walls. (c) In the North Pit, flows of **HG_F** from the chasma wall were back tilted towards their sources as Hebes Mensa arched upward and displaced the drains outward from the mensa.
	DSD Dark smooth deposits *Description*. Includes (a) level to gently sloping, smooth, dark deposits filling closed depressions in the chasma floor, (b) dark flows and mounds on the chasma floor, including the dark hill in the West Pit, (c) small pods and lenses of DSD in **LHF_I** along the base of the south wall, and (d) dark talus aprons banked against the lower slopes of Hebes Mensa and overlying **LHF_L**. **DSD** excludes small patches of dark dunes and a widespread veneer of dark dust within the chasma, including the summit of Hebes Mensa, and on the southwest chasma rim and plains that drape the bedrock topography. *Interpretation*. **DSD** is a poorly consolidated component of **LHF** (perhaps containing basaltic tephra) consisting of insoluble particulates flushed out of **LHF_L** by springs. Eroded **DSD** filled closed depressions, possibly temporary lakes, around Hebes Mensa, forming initially level deposits that became gently tilted toward drainage pits. The large mound of **DSD** in the West Pit that postdates flows of **M_{FS}** may be a fan delta, possibly modified by wind. **DSD** is the source of wind deposits of dark dunes and dust.
Faults	Faults pervade Hebes Chasma, especially on the chasma walls and on Hebes Mensa and Mini-Mensa. Faults are not shown on the geologic map to avoid data clutter.

network of fine cracks, suggesting a thin crust that became brittle.

Allochthonous salt sheets are the broadest salt structures on Earth. Fed by salt diapirs, salt sheets up to 6 km thick can merge into salt canopies hundreds of kilometers wide. These allochthonous flows extrude at the surface or overthrust sediments around them when buried (Worrall and Snelson, 1989; Jackson et al., 1990; Diegel et al., 1995; Talbot, 1998; Hudec and Jackson, 2006, 2009; Talbot and Pohjola, 2009). Even where terrestrial allochthonous flows are young landforms, they consist of salt much older than the sediments beneath them. Likewise, the Hebes flows originated from depth and then extruded across the Hebes floor over younger deposits.

Two terrestrial examples are especially relevant for Hebes. An analog for allochthonous

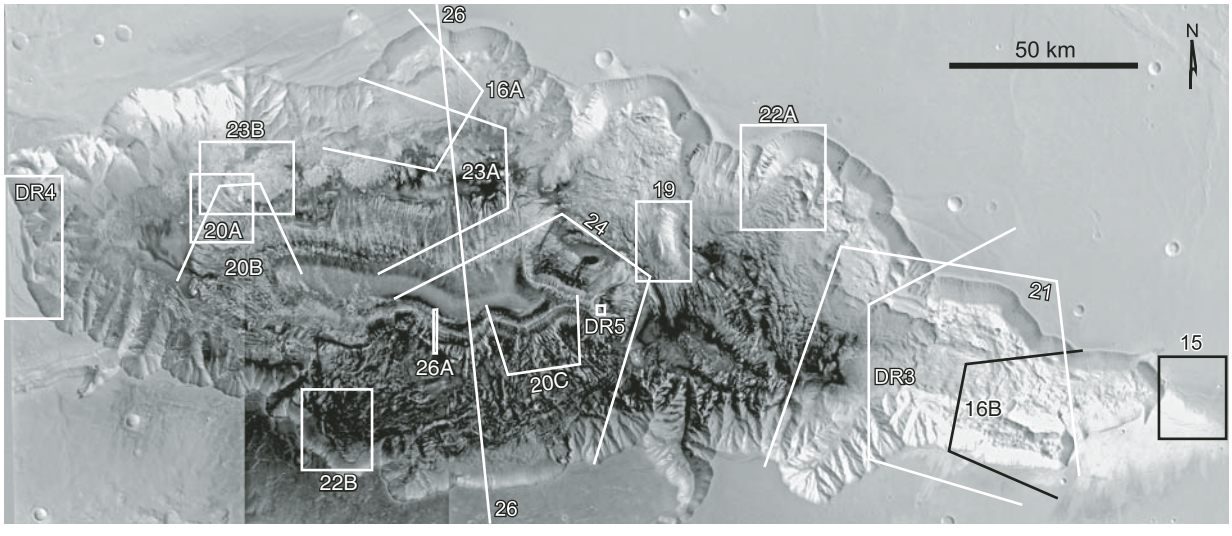

Figure 14. Nadir view of Hebes Chasma showing the location of illustrations. Visible mosaic is from Mars Express High Resolution Stereo Camera.

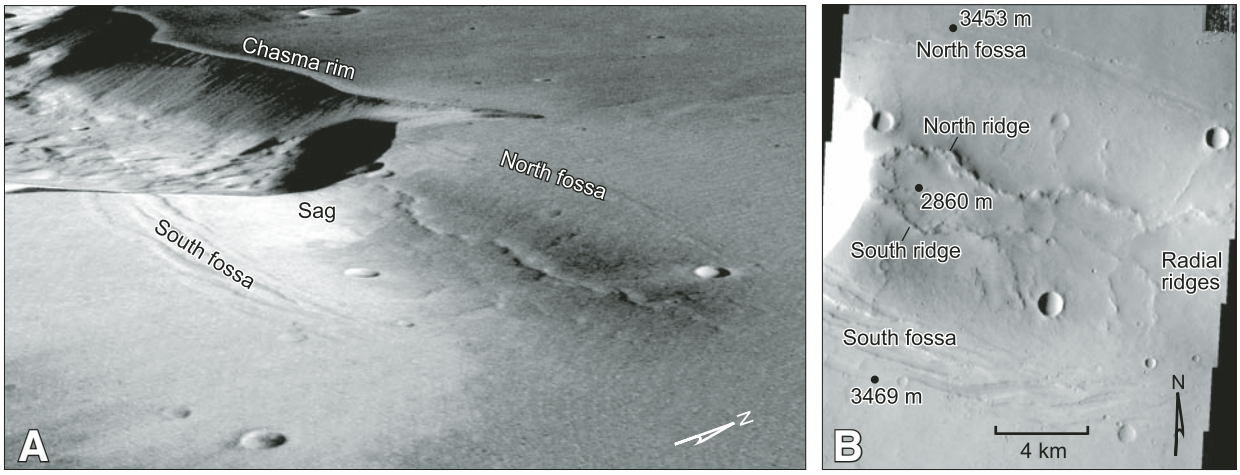

Figure 15. The Swale at the east end of Hebes Chasma. (A) Oblique view to the northwest (no vertical exaggeration). Mars Express High Resolution Stereo Camera. (B) Nadir view with spot heights showing the ~600 m relief of the sag between bounding fossae. *Mars Odyssey* Mission, THEMIS V18276001. Figure 14 shows location.

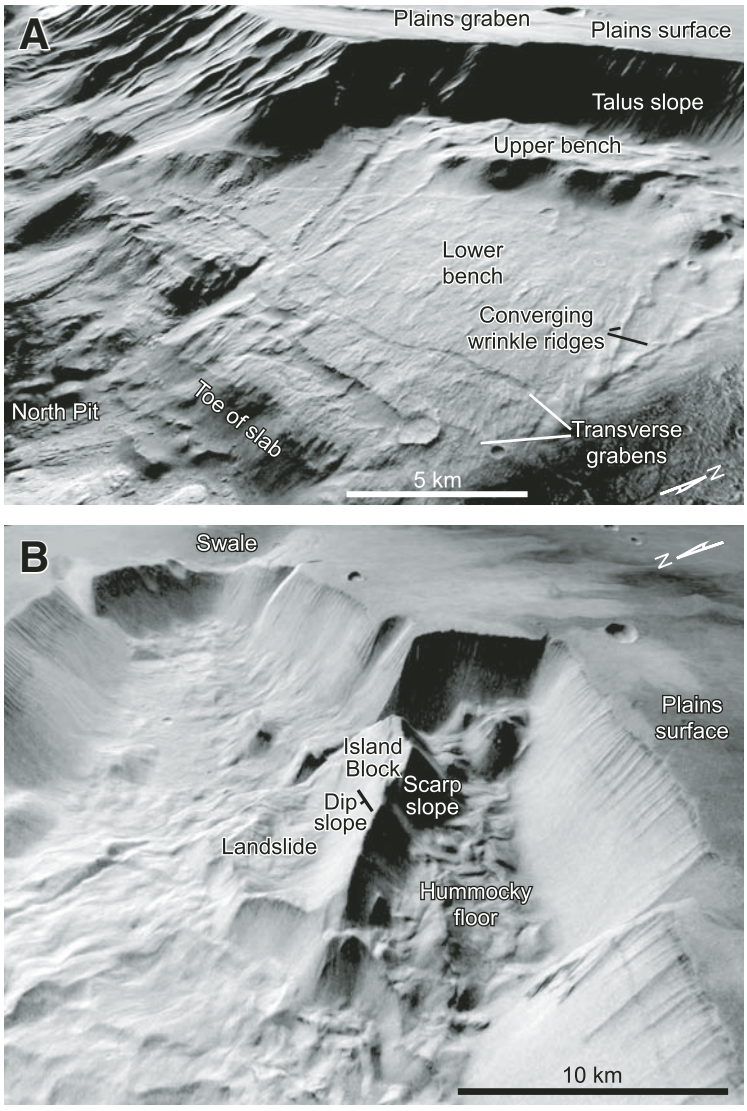

flows breaking out at the base of a slope is the Garmsar salt nappe in northern Iran (Schléder and Urai, 2007; Baikpour et al., 2010). This Eocene salt emerged from beneath torn Miocene roof flaps at the base of the Alborz mountain range and extruded southwestward 19 km over Pleistocene alluvial fans (Fig. 22C). An analog for allochthonous flow of salt down extensional fault terraces is the Red Sea, where flows of Miocene salt cascade toward the depths of an oceanic trough (Mitchell et al., 2010). Terrestrial salt glaciers originally consist mostly of halite, but dissolution gradually increases their proportion of less soluble evaporites and nonevaporite inclusions (Kent, 1979; Bruthans et al., 2009).

Shallow-Sourced Flows Associated with Unroofing

Pale flows originate from layers high in the sides of Hebes Mensa; the longest shallow-sourced mensa flow is 23 km. On the northwest shoulder of the mensa, two adjoining mensa

Figure 16. (A) Big Slab in the north wall of Hebes Chasma in an oblique view to the northwest. Eye altitude is 11 km; ~2× vertical exaggeration. Image via Google Earth from NASA/USGS/ESA/DLR/FU Berlin (G. Neukum). (B) Island Block near the southeast wall of Hebes Chasma in an oblique view to the east. Eye altitude is 22 km; ~2× vertical exaggeration. Image via Google Earth from NASA/USGS and ESA/DLR/FU Berlin (G. Neukum). Figure 14 shows locations.

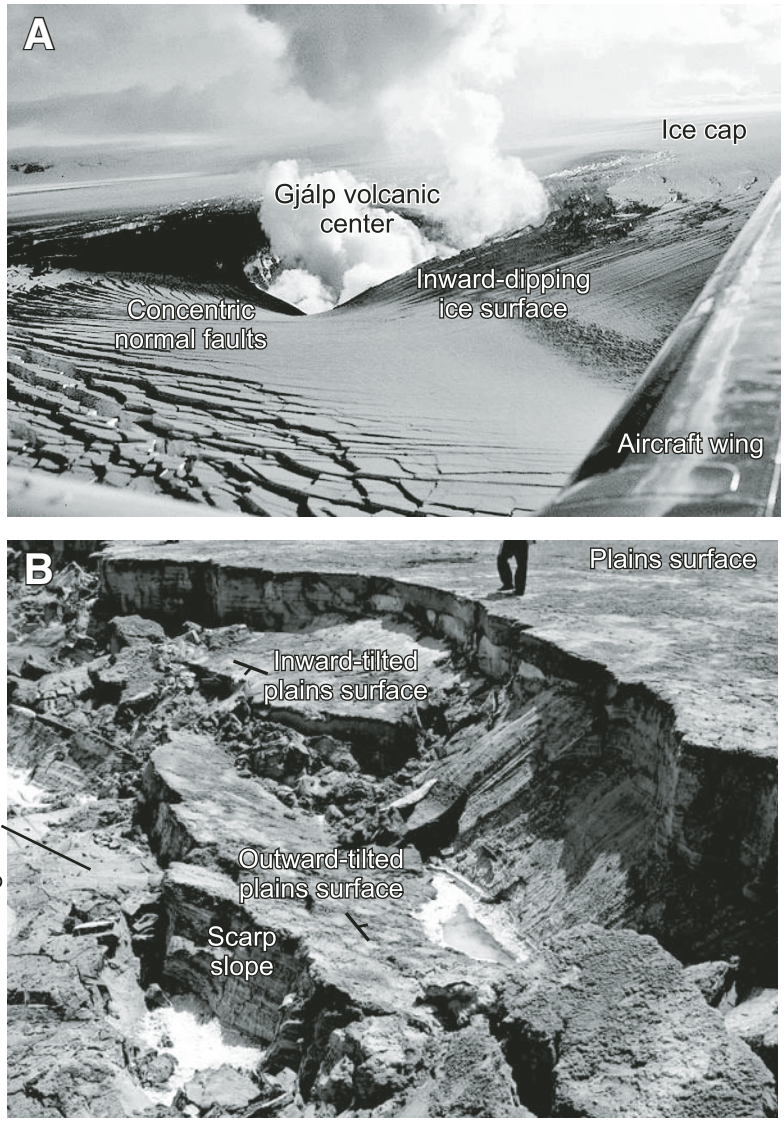

flows, the Northwest Flows, emerged from the mensa's anticlinal hinge and flowed down the mensa slope into the West Pit (Figs. 18, 20A, and 20B). Continuous layering connects the pale, bedded source of LHF_B high on the mensa shoulder with its streaked-out equivalents downstream in the flows. The lower part of the mensa flows has arcuate transverse ridges suggesting longitudinal shortening. The upper part has grooves and streaks parallel to flow suggesting longitudinal extension. Because no headwall or extensional breakaway exists at the head of the flows, they are not landslides.

At least 18 smaller mensa flows emerged from the northeast and southwest slopes of Hebes Mensa and flowed for 4–9 km (Figs. 18 and 20C). Their features are typical of flows: arcuate transverse ridges, longitudinal banding, lobate thickened snouts, and an allochthonous position over younger stratigraphy. The northeast mensa flows off the mensa are narrow,

Figure 17. (A) Collapse of an ice cauldron at Gjálp on Vatnajökull ice cap during a 1996 subglacial eruption in southeast Iceland. The oblique aerial view of ash-covered ice shows the cauldron encircled by concentric normal faults, as in our model (Fig. 7) and in the Swale at the east end of Hebes Chasma (Fig. 15). Image is from http://geonopia.files.wordpress.com/2009/03/vatnajokull-erupcion1.jpg. (B) Fault blocks foundering on the edge of a sinkhole above Pliocene Sedom evaporites, Dead Sea, Israel; person's legs provide scale. Photograph by Alan Gillespie.

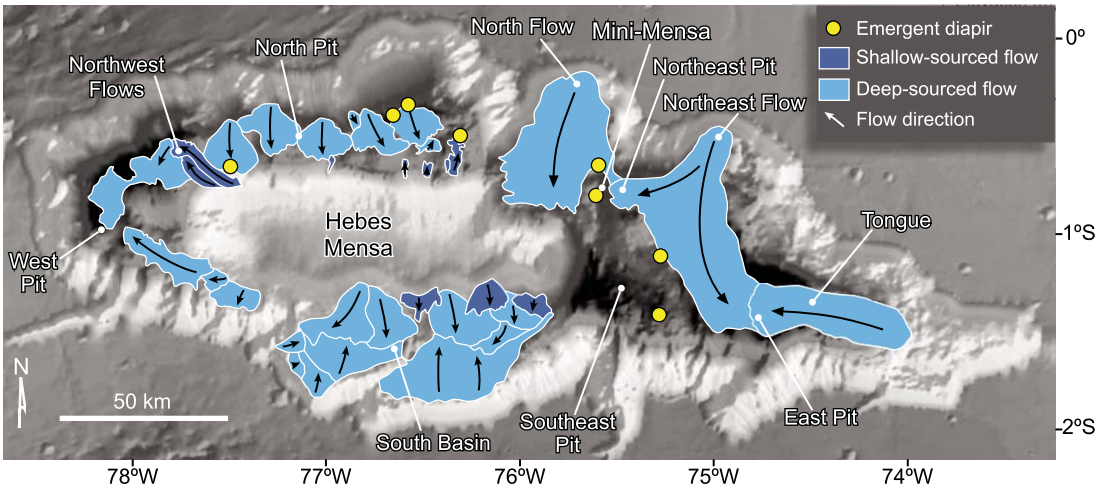

Figure 18. Map of Hebes Chasma showing the larger flows, diapirs, and pits. Large flows are sutured head to head in the South Basin and in the East Pit, as in the model. Background image is a visible mosaic from Mars Express High Resolution Stereo Camera.

fingerlike ridges that project into the dark, smooth deposits flooring the chasma. In addition, many of the pale, fingerlike ridges at the north foot of the mensa resemble less-mature mensa flows. The southwest pale mensa flows also originate in the layered slopes of the mensa but consist of smaller flows that coalesced into canopies. The southwest mensa flows spilled across the trough and reached the south wall of the chasma, where they locally penetrated the mouths of the large gullies of the LHF_I in the walls (Fig. 18).

We infer that unroofing of Hebes Mensa triggered flows off its flanks. Unroofing removed lateral support from the LHF_B layer and other mobile units, so they oozed downhill across an erosion surface. These mensa flows were thought to be igneous by Lucchitta and Chapman (2002), but if so, it is unclear what made them hot and mobile after the mensa flanks were exposed by erosion. These small mensa flows provide striking evidence of mobility but are merely surficial decorations to the landscape, unlike the Great Flows.

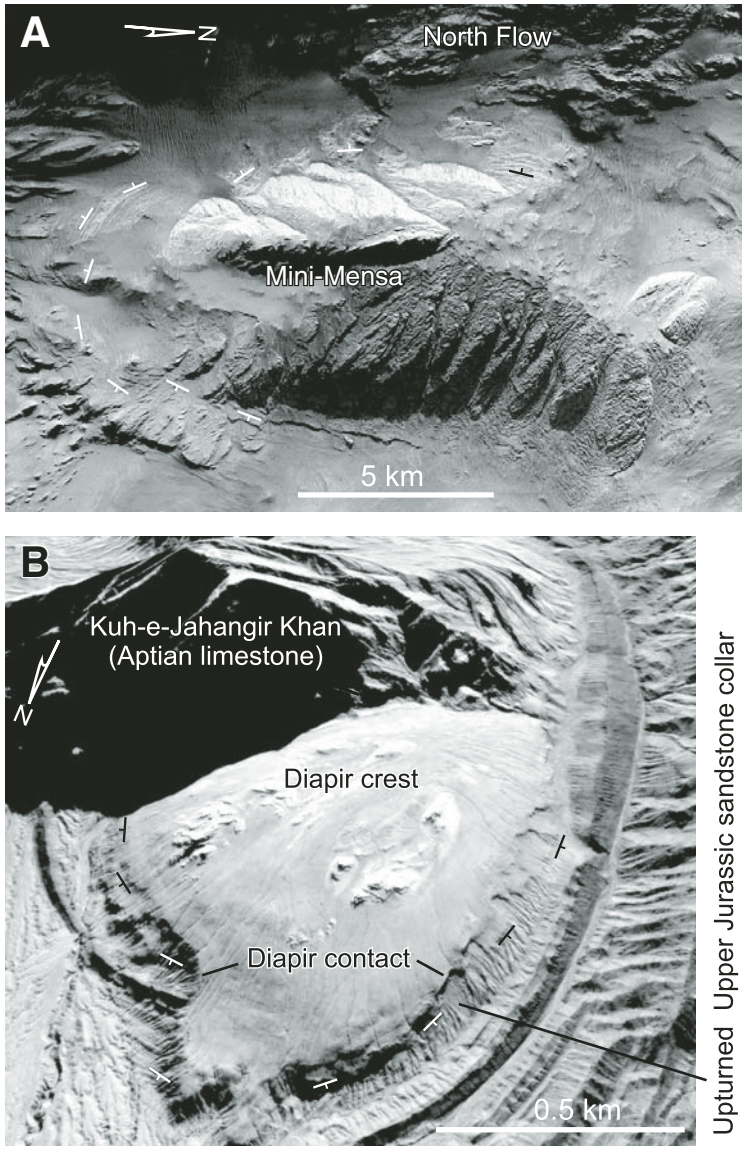

Figure 19. (A) Mini-Mensa, an inferred emergent diapir in Hebes Chasma. Figure 14 shows location. (B) Jahangir Khan diapir composed of Upper Jurassic salt in the North Kerman (Ravar) Basin, Iran. Diapir is 1.2 km long and 0.9 km wide. View is to southeast; eye altitude is 2.2 km; no vertical exaggeration. Image via Google Earth from CNES/ Spot Image and DigitalGlobe.

Drainage (Stages 3 and 4)

Two plains canyons descend into the chasma from the southwest rim (Figs. 1B and 11C), but Hebes lacks surface outlet channels. The plains canyons and the gullies on the chasma walls (LHF_I) lack inner channels, and they end at or above the chasma floor without accumulated deposits. Within the chasma, the only channels are minor features that drained dark smooth deposits from the flanks of Hebes Mensa. Allochthonous flows from the bases of the chasma walls and from the mensa did not carve channels. However, all these flows end in closed pits or troughs in the chasma floor without accumulation, showing that the depressions acted as drains that governed directions of incoming flow. Even the Great Flows taper gently into pits, without the terminal ridge common in terrestrial landslides and rock glaciers (although many retreating terrestrial glaciers ablate to a tapering snout).

The drains are part of the complex topography of the chasma floor (Fig. 18). For example, the East Pit is a 30-km-wide closed sink, 8 km below the chasma rim. Within the pit, a 13-km-long crease mantled by dark material marks where the Tongue and the Northeast Flow meet (Fig. 21). We infer that the crease is the final surface expression of the main drain for the two Great Flows.

Layered rocks similar to those on the upper slopes of Hebes Mensa and Mini-Mensa (LHF_L) are exposed in the walls of the Southeast Pit (Figs. 1B and 18), which is the only pit that the youngest flows did not reach. Hebes Mensa forms the west wall of the pit, and Mini-Mensa forms the north wall. Unroofing of the mensae shed material into the Southeast Pit, but the Great Flows and flows in the South Basin apparently were largely blocked by topographic sills. If the Southeast Pit drained material faster than it was being supplied, erosion of the pit walls may have exposed the lower part of the Lower Hebes Formation. The models show many examples in which lower layers are unroofed in the walls of collapse pits.

The chasma floors to the north and south of Hebes Mensa (North Pit and South Basin; Figs. 1B and 18) appear different but are similar structurally. The North Pit was filled by pale diapiric flows from the base of the north wall of the chasma and by pale flows from Hebes Mensa (Fig. 23). These opposing flows end along a sinuous line that must have been a topographically low drain in the North Pit.

The South Basin received diapiric flows from the base of the mensa and from the base of the south-chasma wall. Minor pale flows from the upper wall of the mensa interfinger with and

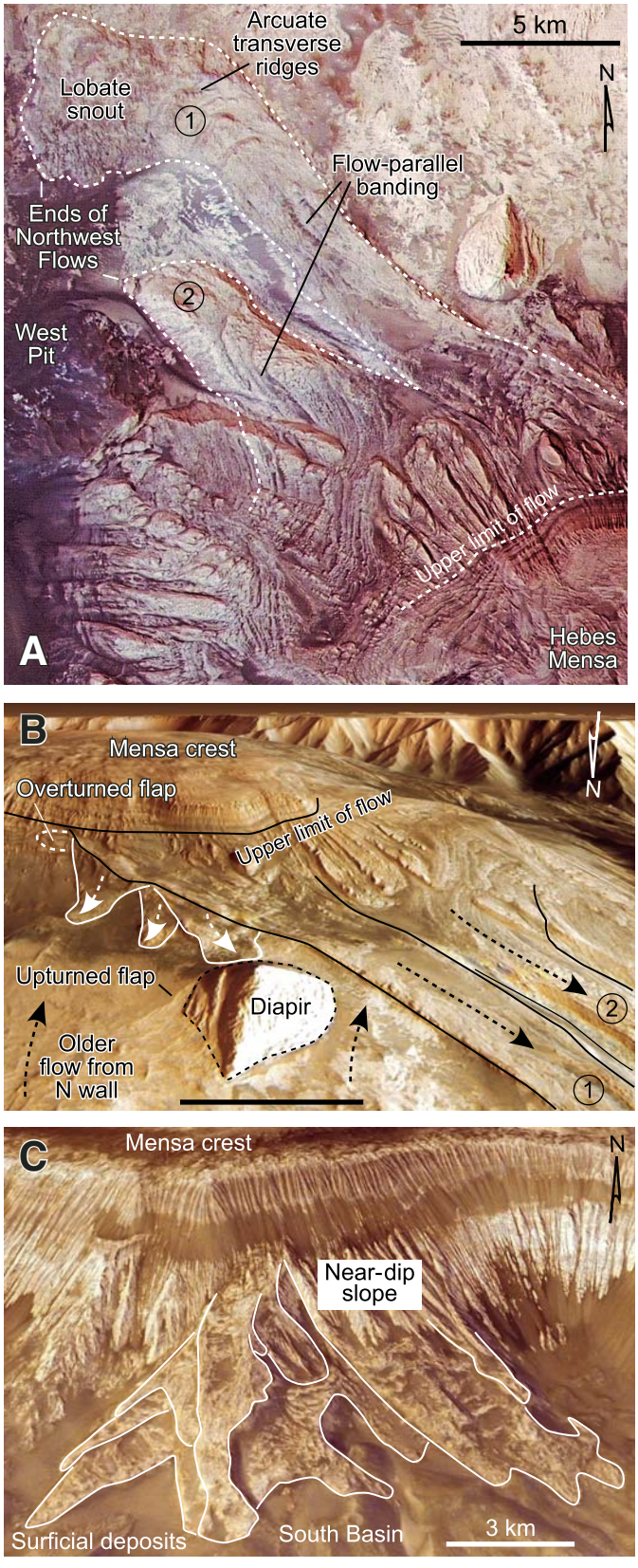

overlie the darker flows (Fig. 20C). The present basin floor is lumpy with many small closed depressions. However, the South Basin is overall a shallow trough along which flows from opposing sides converged, suggesting that subsidence was concentrated along its axis, like the axial creases in the models (Figs. 7C, 8C, and 8D).

The West Pit is the deepest part of an arcuate trench around the west end of Hebes Mensa (Figs. 1 and 18), completing the mensa's encirclement by closed depressions. The floor of the trench and West Pit is covered by flows off the mensa. These flows are overlain partly by a mound of dark smooth deposits sourced from the west flank of the mensa (Fig. 13). The chaotic slump on the west wall of the chasma (LHFs) did not leave deposits on the floor of the West Pit, implying that the west wall collapsed into the pit before flows oozed off Hebes Mensa.

The model suggests how the drains may have evolved. Deep drainage was first expressed at the surface as gentle sags and then as slabs tilting and sliding inward away from extensional hinges (Figs. 6 and 7). Where slabs sliding from opposite sides met in a crease, they overrode one another in sharply defined pits and troughs. As soon as material at the surface—rather than at depth—began to drain as particulate flows, the troughs and pits widened, merged, and softened in outline. Their sides sloped inward to their deepest points. The model trenches are analogous to the valleys on the north and south sides of Hebes Mensa. The large East Pit has gently sloping sides as in the model, consistent with flow of the Lower Hebes Formation at depth toward the pit and with continued postflow subsidence. Walls of some pits contain gentle bulges, suggesting diapiric upwelling just below the surface, as in the model (Fig. 10).

Figure 20. (A–B) Shallow-sourced flows (numbered) off the northwest shoulder of Hebes Mensa. (A) Vertical view from Mars Express High Resolution Stereo Camera. (B) Oblique view looking south of the area in A, showing the two numbered flows. Eye altitude is 4.8 km; ~2× vertical exaggeration. Image via Google Earth from ESA/DLR/FU Berlin (G. Neukum). (C) Oblique view to the north of shallow-sourced flows from the south flank of Hebes Mensa. Eye altitude is 9 km; ~2× vertical exaggeration. Image via Google Earth from ESA/DLR/FU Berlin (G. Neukum) and NASA/USGS. Figure 14 shows locations.

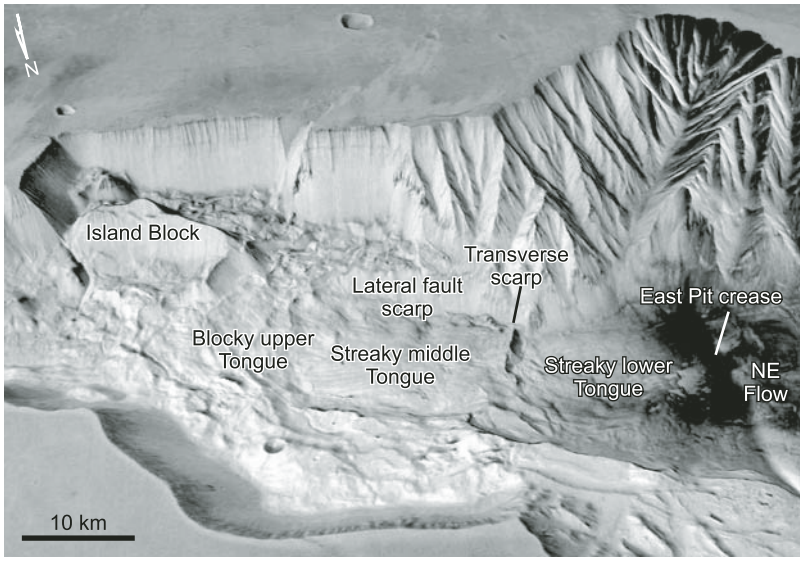

Figure 21. The Tongue in the eastern half of Hebes Chasma in an oblique view to the south. Eye altitude is 61 km; 2× vertical exaggeration. Image via Google Earth from ESA/DLR/FU Berlin (G. Neukum). Figure 14 shows location.

Formation of Hebes Mensa (Stages 3 and 4)

Hebes Mensa presents a puzzle as to the age of its units and where they belong in a stratigraphic sequence. The 109-km-long mensa rises 8 km from the chasma floor to within a few hundred meters of the chasma rim. The north and west flanks of the mensa have clearly defined layers (Figs. 23 and 24). Similar layers are present on the sides of Mini-Mensa and in the Southeast Pit (Hauber et al., 2008), but they are not present, or at least recognizable, in the chasma walls below the Upper Hebes Formation. Some researchers have concluded that Hebes Mensa consists of interior layered deposits (ILDs) laid down after the chasma formed (e.g., Witbeck et al., 1991; Lucchitta et al., 1992; Le Deit et al., 2008). However, this explanation seems implausibly elaborate for the closed basin of Hebes, because regardless of how the chasma itself formed (Table 1), if the mensa layers filled a preexisting chasma, then there must have been a second (undocumented) episode of chasma excavation

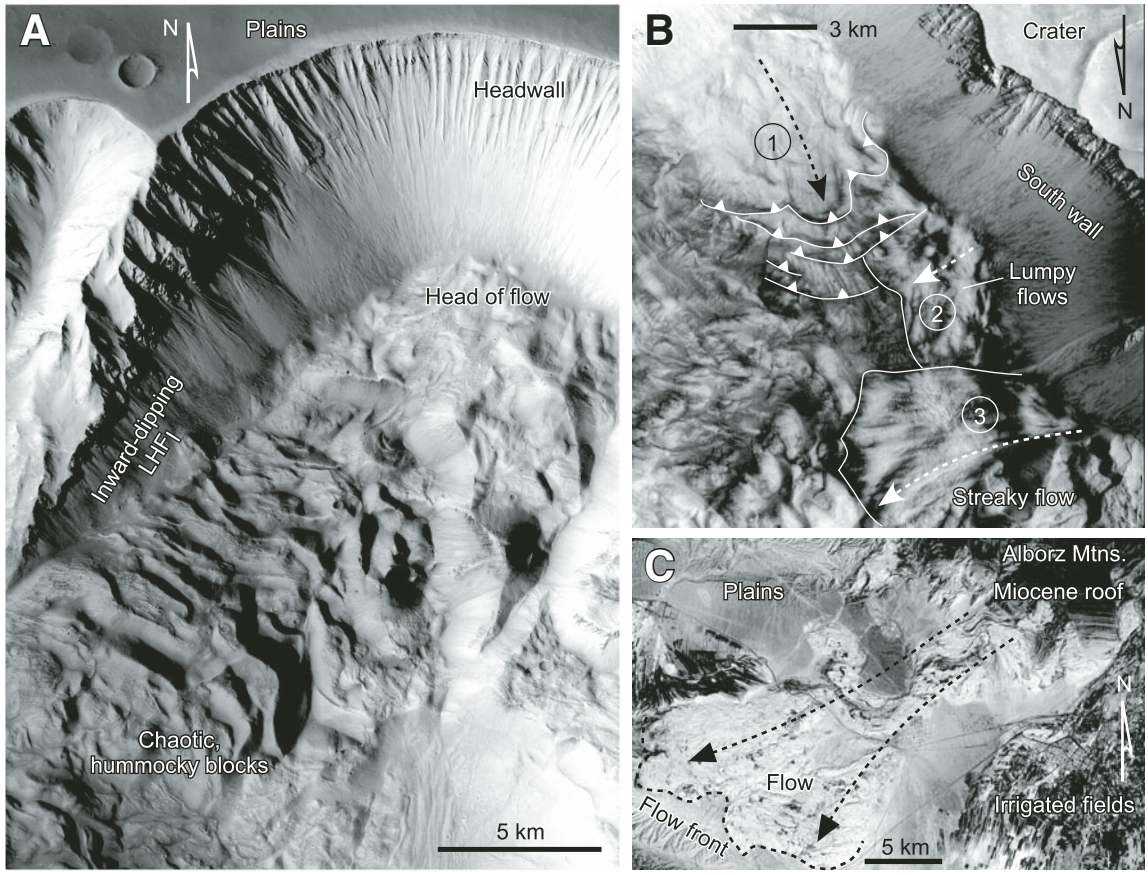

Figure 22. (A) Deep-sourced Northeast Flow emerging from the base of the north wall of Hebes Chasma in nadir view. (B) Deep-sourced flows from the south wall of the South Basin in nadir view. Numerals 1–3 indicate sequence of flows. Figure 14 shows locations. (C) Deep-sourced Garmsar salt nappe emerging from the Alborz mountain front in northern Iran. From its Miocene roof to the flow front, this wasted remnant of allochthonous salt dips at 0.7° to the southwest over a length of 24 km. Image via Google Earth from CNES/Spot Image, DigitalGlobe, and GeoEve.

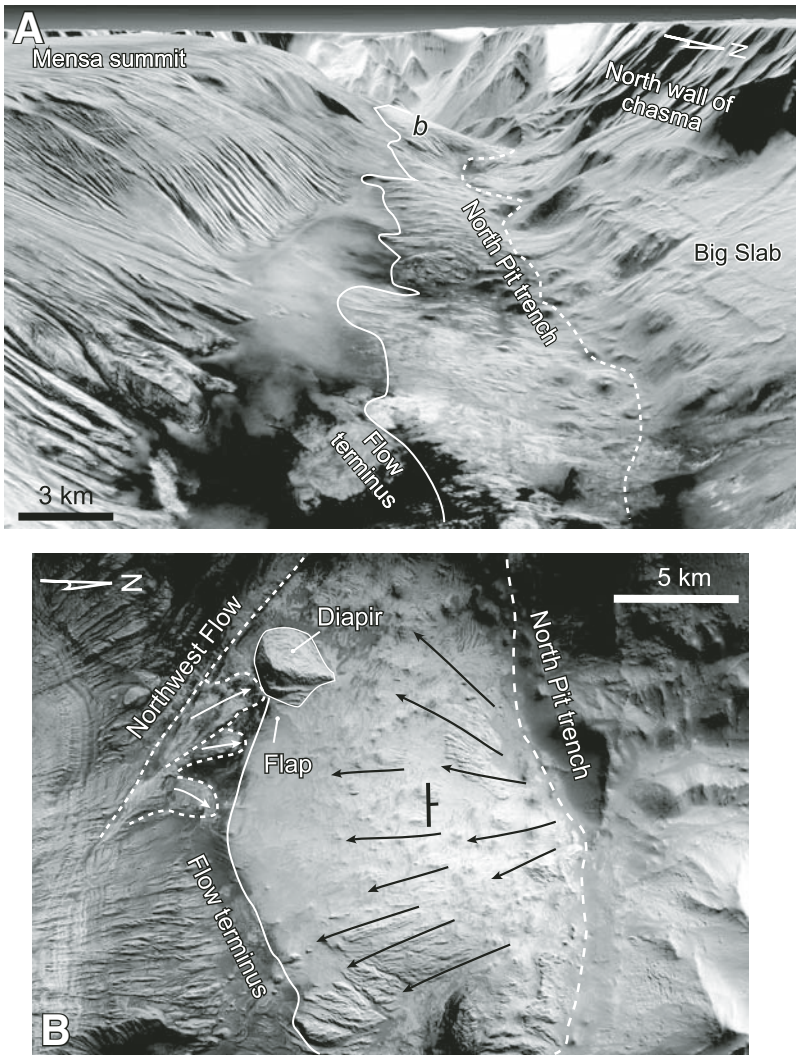

Figure 23. (A) Deep-sourced flows from the north wall of Hebes Chasma into the North Pit. The terminus of the flows (solid line) is inferred to mark the former drainage axis; the present-day trench (dashed line) is inferred to mark the final drainage axis. Oblique view to the west; eye altitude is 8.5 km; 2× vertical exaggeration. HRSC image via Google Earth from NASA/USGS and ESA/DLR/FU Berlin (G. Neukum). (B) Vertical view of the westernmost deep-sourced flow, marked *b* in part A, showing inferred streamlines (black arrows) from source of flow in north wall of chasma. The later rise of an inferred diapir upturned an outward-dipping flap in the deep-sourced flow on the diapir's eastern flank. The shallow-sourced Northwest Flow overran the deep-sourced flow, which was originally from the north but today slopes at 6°–10° to the north. Figure 14 shows locations.

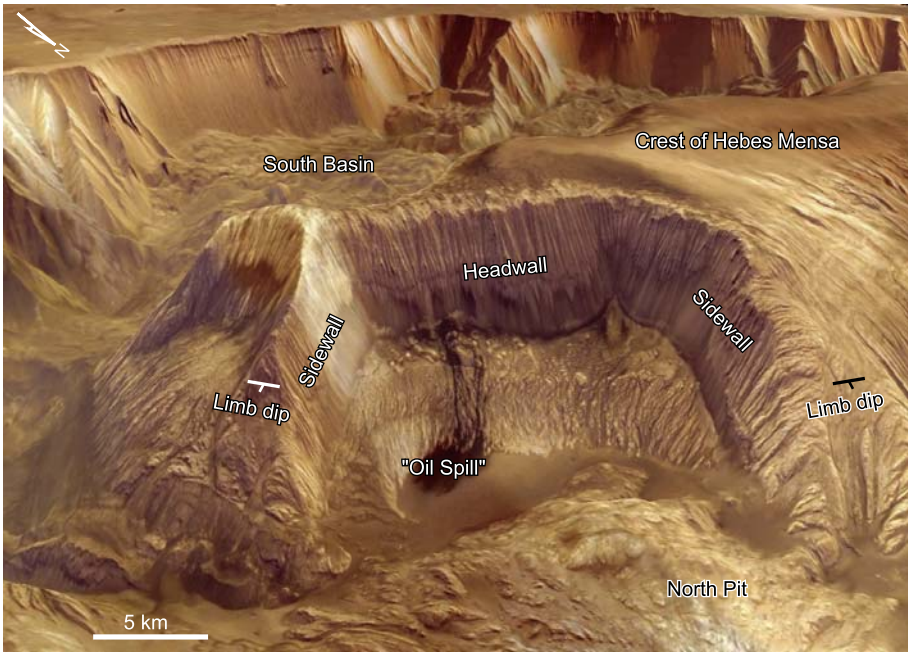

Figure 24. The east end of Hebes Mensa in an oblique view to the southwest. The sidewalls of a rectangular slump expose the northward-dipping limb of the anticline forming the mensa. Eye altitude is 15 km; 2× vertical exaggeration. Image via Google Earth from NASA/USGS and ESA/DLR/FU Berlin (G. Neukum). Figure 14 shows location.

that left Hebes Mensa as a remnant. Rossi et al. (2008) and Gindrod and Balme (2010) proposed that the mensa is a giant spring mound that postdates formation of the chasma. However, they did not explain the origin of the chasma itself. Malin and Edgett (2000) suggested that the mensa is an island of chasma-wall material with just a few hundred meters missing from the top due to erosion, but this does not explain the lack of comparable layers in the chasma walls below Upper Hebes Formation.

We present new evidence here based on our models and on detailed geologic mapping that the mensa units, LHF_B and LHF_L, are composed of deep materials exposed by unroofing and arching, which we tie to diapirism in the discussion section. This hypothesis explains why Hebes Mensa does not consist of younger infill and why its layers are not visible in the chasma walls. Units LHF_B and LHF_L are thus inferred to be stratigraphically below the level of Lower Hebes Formation exposed in the chasma walls and equivalent to those in Mini-Mensa and in the Southeast Pit (Hauber et al., 2008).

The cratered plains surface is absent on the crest of Hebes Mensa, even though the crest is nearly level with the chasma rim (Figs. 11C and 24). If Upper Hebes Formation ever existed on the mensa, it was removed or altered beyond recognition. The top of the mensa is partly veiled by surficial deposits, including smooth areas scored by dust devils and honeycombs resembling cemented dunes. Beneath this thin mantle, and well exposed on the upper flanks of the mensa, there is unit LHF_B (botryoidal Lower Hebes Formation), a unit having botryoidal, concentrically layered cells up to 1 km across and clumps of jumbled pieces of folded layers (Fig. 25). Wind erosion has sectioned and etched the cells. They resemble coalesced fumarolic or spring mounds or small diapirs (Adams et al., 2009). Preserved thickness of LHF_B is ~100 m. The unit dips up to 10° outward from the mensa crest on the north and west flanks, and 15°–18° on the southwest slope where the unit reaches the floor of the South Basin (Figs. 13 and 26). The top of LHF_B is defined only by the crest of the mensa, so its original thickness is unknown. The base of the unit is exposed along the higher parts of the north and west flanks of the mensa.

LHF_L crops out below LHF_B along the sides of the mensa. Layers in LHF_L are prominent on the north and west flanks where individual layers continue laterally for up to 5 km. The origin of the layers is unknown; they could be depositional or tectonic. We cannot exclude the possibility that botryoidal structures are also present in LHF_L but exposed only in oblique cross section, so that they appear as streaky layers rather than as the rounded structures visible in plan-form on the mensa crest. Layering is obscure or absent on the steeper south and east slopes, which are deeply gullied and interrupted by dark bands of talus and alcove slumps. In these areas, the contact between LHF_B and LHF_L is uncertain because neither botryoidal structure nor fine layering is present. On the geologic map (Fig. 13), a dashed line locates the boundary of the observed botryoidal structures, which typically is at the rim above the upper dark band of talus or above the alcoves. The base of LHF_L is not defined.

We do not consider the dark bands to be stratigraphic layers and do not define them as map units because the dark layers are interrupted by gullied patches of LHF_B and LHF_L (Fig. 25). Instead, we interpret the alcoves and the dark bands on the south wall as talus-covered slump scars where LHF_B and LHF_L have been displaced.

The slump scars and most of the deep gullies were sources of dark material that spilled from all sides of the mensa (Figs. 20, 23, and 24). Adams et al. (2009) proposed that the dark material, possibly particles of basaltic tephra, was expelled by springs from fractures at the surface of the mensa. Dark talus fans typically are aligned and bounded along horizontal fracture traces across the top (spring line?) and in places the bottom (drain line?) of the dark bands and in the alcoves. Dark material in the gullies near the base of the mensa on the west, north, and east sides is contiguous with the dark smooth deposits of the West Pit, North Trench, and the Oil Spill. The dark debris ponding in low areas embayed the adjacent topography, implying that the debris was deposited from a fluid. Further evidence of circulating fluids is the

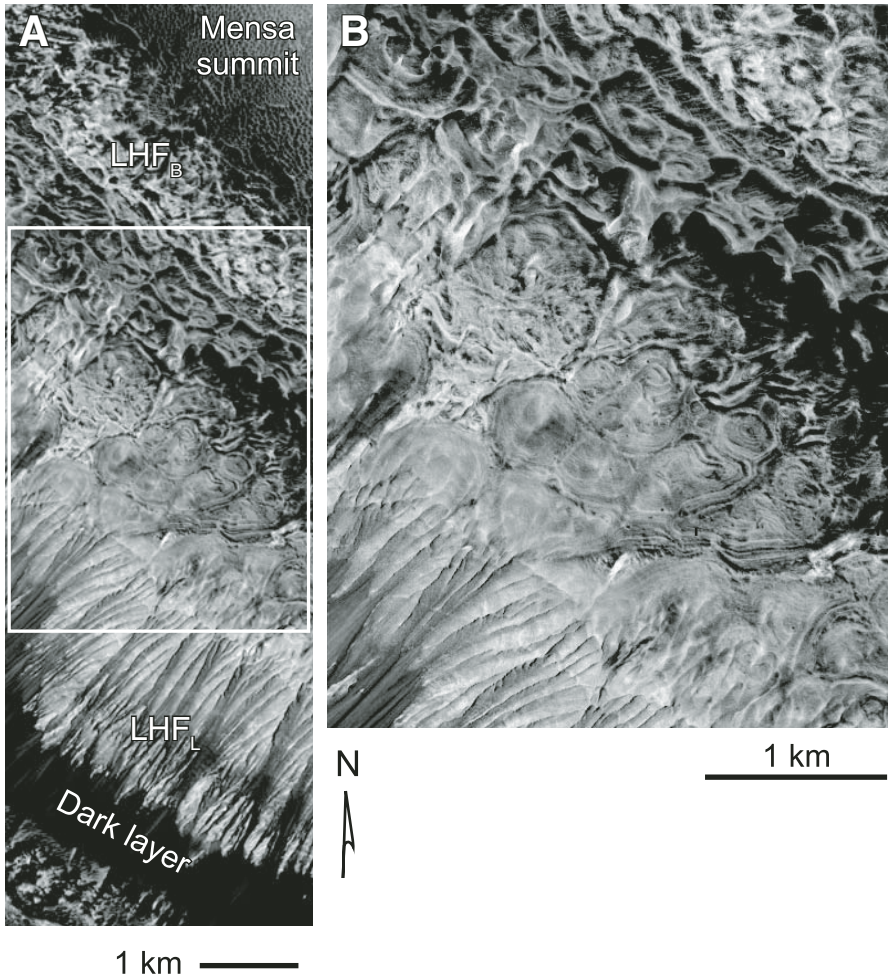

Figure 25. Botryoidal Lower Hebes Formation (LHF_B) capping Hebes Mensa. (A) Oblique swath down the south flank of Hebes Mensa showing the pale botryoidal layer overlain by a mantle of cemented eolian deposits and underlain by layered deposits (LHF_L), including the discordant band of dark deposits. (B) Detailed view from A, showing the cells in LHF_B inferred to result from fluid escape or diapirism. Image is from Mars Global Surveyor, Mars Orbiter Camera E1700518. Figure 14 shows location.

morphology of the talus fans. Some fans end laterally in cliffs undercut by *younger* fans, which implies cementation of the older fans, perhaps by precipitates from groundwater, before they were sapped and undercut.

The structure of Hebes Mensa is that of an asymmetric antiformal box fold: Its crest is nearly flat, its hinge encircles the mensa, and the antiform plunges periclinally at both ends. The limbs of the antiform dip into the surrounding pits. Only the north and west sides of the mensa show well-defined layers, and together LHF_B and LHF_L may only be ~400 m thick. Because layers of LHF_L dip at ~10° on topographic slopes of 10°–20° (Hauber et al., 2005, 2006), they create an illusion of greater thickness. The steepest dips on the south flank may approach the slope angles (>30°). On smaller scales within the antiform, layers are offset by myriad small faults and are tightly contorted by disharmonic folds.

On the southwest flank, which is not interrupted by dark bands, LHF_B drapes as a dip slope from the mensa crest to the floor of the South Basin (Fig. 26). A scarp of dark talus along the base of this slope is the headwall of a large alcove block of mensa material that is partially buried under dark flows on the floor of the South Basin. Along the edge of the basin floor, a narrow, pale band continues eastward, branches through the twin alcoves, and connects with the apron of LHF_B and LHF_L along the southeast wall. The pale band has contorted internal layers, suggesting that it may be a remnant of LHF_B or LHF_L entrained along the faulted margin of the mensa.

Summarizing, we interpret Hebes Mensa as a 7-km-high mound cored by unknown materials and covered by a thin shell of antiformal LHF_B and LHF_L—units that include folded and broken layers and a high density of faults. Parts of the shell slumped or flowed off the flanks. Even on gentle slopes, shallow allochthonous flows oozed from the softened shell, especially on the west end of the mensa. Along the southwest chasma wall, the flows embay the mouths of the gullies and the Southwest Plains Canyon. So, the flows off Hebes Mensa were probably a gravity-spreading response to subsidence of the surrounding troughs and pits. Dark material leaked from all sides and accumulated in small basins at the base of the mensa slopes. The contact between the mensa and its surroundings is obscured by all these surficial deposits and flows except along the faulted southwest margin. The structure of the mensa is not consistent with an undeformed stack of interior layered deposits or chasma wall material. Instead, we infer that the Hebes Mensa rocks were raised from depths equivalent to the Southeast Pit.

In the discussion section, we speculate on the kinematics behind the rise of Hebes Mensa.

DISCUSSION

Karstic Collapse

Having examined the landforms of Hebes Chasma, we favor karstic collapse to explain its origin, although other Valles Marineris chasmata most likely formed by a combination of processes that varied with location.

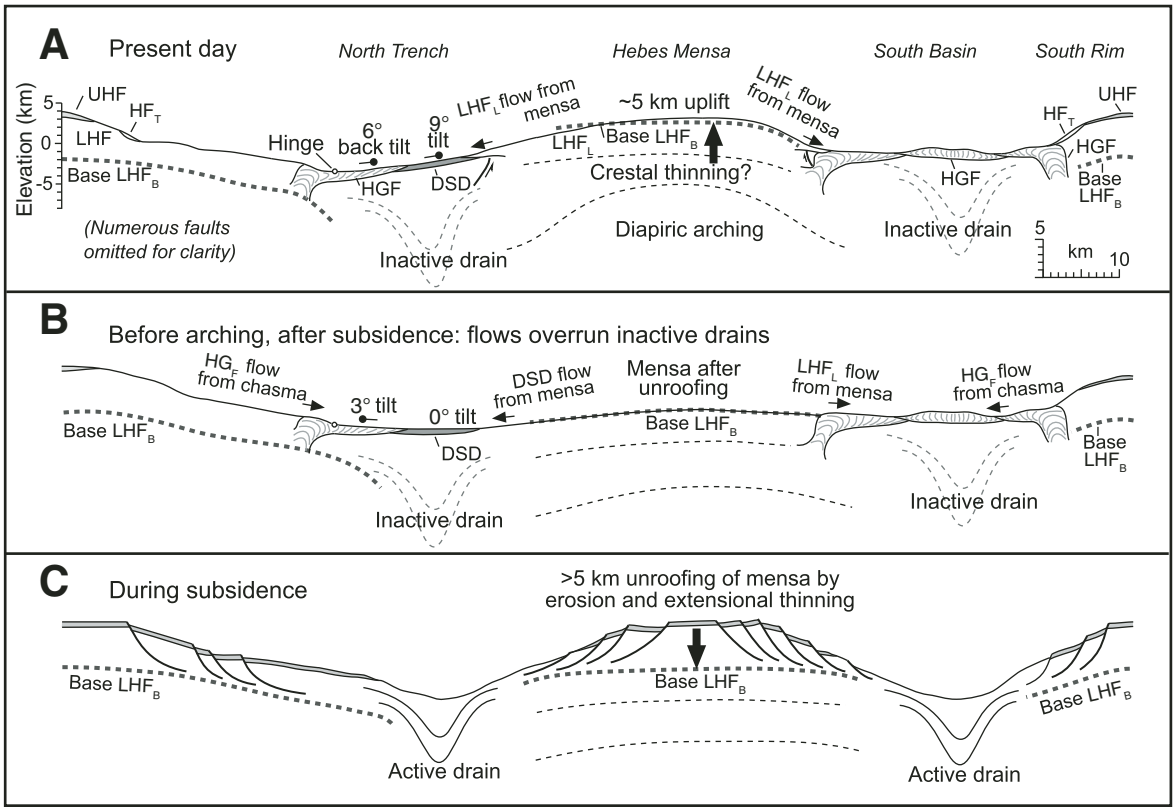

Figure 26. (A) Present-day N-S cross section across Hebes Chasma and mensa. Location shown in Figure 14. (B) The same section restored to a stage after the chasma subsidence had mostly ended, after the drains were clogged and overrun by flows from the base of the mensa and chasma walls. (C) The same section restored to an even earlier stage of chasma subsidence as erosion and extensional thinning unroofed the mensa. Thin flows and deposits are thickened in the cross sections to show age relations. For restoration method and implications, see the text; for map symbols, see Figure 13. DSD—dark smooth deposits.

Karstic subsidence entailed 10^5 km^3 of material draining from the chasma by subsurface fluid flow. This hypothesis explains (1) how the missing material was removed when a mixture of ice, hydrates, soluble minerals, or hydrous salts melted or disassociated and yielded water to drain into a regional aquifer, leaving behind insoluble solids; (2) absence of deposits around the chasma rim, excepting a coating of dust; (3) absence of a surface outlet and of fluvial channels on the chasma floor; (4) the elliptical planform, abrupt scalloped margins, blunt ends, and roughly uniform depth of chasma; (5) absence of nearby grabens in the plains except for narrow fossae; (6) inward tilting of Upper Hebes Formation along the chasma walls; (7) preservation of the plains surface and Upper Hebes Formation on fault-bounded benches; (8) pits on the chasma floor, which acted as drains; (9) allochthonous flows that oozed from chasma walls and mensa flanks and that end in pits; (10) Hebes Mensa and Mini-Mensa as antiforms arched by diapirism so that the shallow-sourced flows off Hebes Mensa were actually fed by a deep but upwarped stratigraphic layer; and (11) presence of the adjoining Echus Chasma outburst flood (Robinson and Tanaka, 1990).

If the karstic collapse hypothesis is correct, chasma-wall "landslides" interpreted by others are (1) inward-tilted slabs of plains surface or (2) allochthonous flows of stratigraphically older material. Hebes Mensa, which has been widely interpreted as a younger infill of "interior layered deposits," instead consists of uplifted stratigraphically old layers, which is our contention. Allochthonous flows shed off the mensa resurfaced the chasma floor and embayed gullies in the chasma walls. It is these allochthonous flows that are younger than the formation of the chasma, not the layered materials of the mensa itself.

Any one feature in Hebes Chasma is open to several interpretations, but the weight of geologic observations and the model simulations build a strong case for karstic subsidence to form Hebes Chasma. The following geologic observations and interpretations explore more deeply the two main processes forming Hebes Chasma: (1) subsidence, which is familiar in karstic collapse, and (2) mobilization, which is not. This leads to speculation on the composition and rheology of the mobilized materials.

Surface Expression of Subsidence

Regional Structural Control

Three fracture sets in the plains surface influenced Hebes subsidence. The main regional fracture set strikes west-northwest as part of the Valles Marineris system of linear, parallel canyons (Fig. 1A). On this trend, 150 km farther east from Hebes Chasma, there lies Ganges Catena, a 227-km-long intermittent chain of pits that partly merged to form a small chasma (Fig. 1A). Pit chains have been attributed to local collapse, physically modeled by drainage into dilational normal faults and subvertical fissures (Wyrick et al., 2004). The same west-northwest trend continues the other side of Hebes Chasma as the squared-off head of Echus Chasma (Fig. 1A). A swarm of wrinkle ridges trending north-northeast from the Thaumasia Plateau completes a structural picture of east-southeast shortening and north-northeast extension.

A second, minor set of regional grabens strikes northeast, oblique to the main Hebes trend. These fossae control the stubby side canyons of western Hebes and fray the canyon margins (Fig. 11C). Hebes Chasma incises the north margin of the Thaumasia Plateau, an uplift having structures that suggest a megaslide (Montgomery et al., 2009). Some have suggested an orogenic origin for the plateau (e.g., Courtillot et al., 1975; Anguita et al., 2006), but this idea was disputed by Nahm and Schultz (2010) because the low topographic slope is incompatible with critical-taper mechanics (an argument they further invoked to question the megaslide hypothesis and a role for salts even though the viscous yield strength of salt is [1] more relevant over geologic time than frictional strength and [2] negligible compared with the frictional strength they modeled). The north margin of the megaslide, which includes Ius, Melas, and Coprates chasmata (Fig. 1A), was inferred to be left-lateral transtensional, which would explain the oblique grabens at the west end of Hebes Chasma (Fig. 11C). Northwest of the chasma, there is a set of north-striking grabens called Echus Fossae (Fig. 1A), but approaching Hebes Chasma, this set curves into alignment with the northeast-striking grabens (Fig. 11C).

A third, much smaller set of grabens in the plains surface are curved and concentric to the chasma rim (Fig. DR4 [see footnote 1]). Their geometry suggests that they are unloading fractures formed during chasma collapse.

Processes of Subsidence

During subsidence, material did not simply fall into a canyon and disappear down a drain. Instead the deep Lower Hebes Formation and older rocks began to sag as their fluids drained downward or escaped to the atmosphere. This sag spread to the surface and caused the surface to dimple as swales. As the swales sagged further, they extended and broke into slabs. The slabs tilted inward toward the most active drains. Shallow parts of the slabs preserved the plains surface in extensional fault benches. These relics fragmented as subsidence intensified. As material migrated inward to the nearest drains, the overall chasma collapse widened as lateral support was removed, creating headwall alcoves. The style of collapse depended on proximity to the drains. Chasma walls close to a drain, such as the West Pit, collapsed in massive landslides, the debris of which poured directly into the pit. In contrast, where chasma walls were far from a drain, such as the East Pit, shallow layers foundered as cohesive slabs that became mobilized in their deeper parts.

Diapirism and the Rise of Hebes Mensa

Other authors have inferred salt diapirs in the Valles Marineris (e.g., Milliken et al., 2007; Popa et al., 2007; Baioni and Wezel, 2008). However, our paper is the first to link diapiric rise and karstic collapse on Mars. We know of no terrestrial analogs combining diapirism and collapse, although there are small-scale similarities with sink holes, where deep, mobile salty mud wells up between foundering fault blocks (Fig. 17B).

Downward drainage and upwelling diapirism were both driven by gravity. Diapirs rose and emerged sporadically at the surface wherever overburden thinned extensionally at the hinges of inward-bending slabs or in gaps where slabs tore away toward the drainage pits (Fig. 7). This structural unroofing created a differential load that forced the mobile material upward by active or reactive diapirism, as in salt tectonics (e.g., Vendeville and Jackson, 1992; Schultz-Ela et al., 1993; Hudec and Jackson, 2007). Emergent diapirs then extruded deep-sourced allochthonous flows from the walls of Hebes Chasma and the base of Hebes Mensa (Fig. 22). An extreme pressure gradient separated several kilometers of overburden load rimming the chasma from a merely atmospheric load at the free face within the chasma. This lateral pressure gradient would have expelled mobile material into the chasma floor, regardless of its density.

Evidence for Diapirism of Hebes Mensa

The largest structure within the chasma—Hebes Mensa—has also been the most refractory to explanation. We suggest that the stratigraphic and tectonic paradox of Hebes Mensa can be explained by the arching of a large gentle diapir surrounded by drainage pits and troughs. Four lines of evidence support the diapiric hypothesis.

First, stratigraphic units in Hebes Mensa were demonstrably mobile. At least 20 flows oozed down the sides of the mensa, and some reached deep pits after flowing up to 23 km. Most of these flows originated in the botryoidal

layer, LHF_B, the layering of which survives in streaked or contorted flow patterns in the flows. Some flows are bordered by recumbent drag folds in their source layers (Fig. 20B).

Second, the antiformal structure of the mensa is typical of the arched roofs of active diapirs (Fig. 24). Extrapolating the dip of the botryoidal layer outward from outcrops on the crest of the antiform results in a geometry consistent with the hypothesis that equivalent strata lie in the lower part or base of the chasma walls (bearing in mind the liberal assumptions extrapolating vanished deformed strata) (Fig. 26). Further evidence for this correlation is the previously mentioned similarity of layered deposits in the walls of the Southeast Pit to those on the upper slopes of Hebes Mensa, several kilometers higher in relief. Lateral shortening and magma intrusion can also arch strata, but evidence for these processes in Hebes Chasma is lacking.

Third, the models show how unroofing during subsidence can trigger diapirism and create a broad arched uplift after surrounding areas subside and drain away. Recall the comparison of two models in Figure 12: The mensa formed by extension alone had a flat-topped crest level with the plains, whereas the mensa formed by diapirism and extension had an arched crest below the plains level, like Hebes Mensa. The model shows how a diapir responds to extensional unroofing. The crest of the dome extended (Fig. 9A). Unit 1 was largely stripped off by this crestal extension, then by mass wasting of both units 1 and 2 (Figs. 9B and 9C), and then by viscous flow of unit 3 off the arch beneath a mantle of a thinned unit 2 (Fig. 9D). Viscous unit 3 in the core of the model dome rose diapirically, partly because it was buoyant and partly because unit 3 was overlain by thinned overburden and so received viscous flow from areas loaded by thicker overburden. This model dome was equivalent in position to Mini-Mensa, another inferred diapir in Hebes Chasma.

Fourth, a shift in the dynamic balance between drainage and upwelling in the North Pit records arching of Hebes Mensa. This shift altered how drainage influenced major flows from the north wall of the chasma. Ends of these flows are close to the base of the mensa and mark the approximate position of the drainage axis during their flow (Fig. 23). However, the midsection of these flows is now lower than their termini. The North Pit trench, a crease-like drainage axis, now crosses the middle of flows from the north chasma wall, which indicates that the flows have been back-tilted away from the mensa. This anomaly indicates that the drainage axis shifted northward away from the mensa after the flows extruded. This outward shift of up to 10 km is compatible with gradual rise and arching of Hebes Mensa. The same outward shift is suggested by the outward tilt of smooth dark sediments at the north and west foot of the mensa (Fig. 13). The deposits embay gullies at the base of the mensa, implying that they accumulated horizontally, but they now tilt 10° northward. We infer that further rise of the mensa lifted and tilted sediments to their present dip and displaced the West Pit outward to its present position.

The flat crest of Hebes Mensa is compatible with diapirism. Most terrestrial halokinetic diapirs covered by a roof are overlain by subhorizontal or gently arched strata, extended by normal faults (Nelson, 1991; Schultz-Ela et al., 1993; Rowan, 1995; Davison et al., 2000). Even the crest of a diapir itself is dominated by subhorizontal flattening fabrics in models (Dixon, 1975; Jackson and Talbot, 1989; Talbot and Aftabi, 2004; Chemia and Koyi, 2008). The only robust exception to horizontality is where dissolution has removed the diapir's crest so that steep fabrics, which formed deeper in the diapir, subcrop against the overlying cap rock or the topographic surface (Richter-Bernburg, 1987; Talbot and Jackson, 1987; Jackson et al., 1990; Talbot et al., 2009). These analogies with model and terrestrial diapirs explain why the crest of Hebes Mensa is flat and predict that steeper structures are likely in the mensa's core.

In summary, we infer that Hebes Mensa consists of lower Lower Hebes Formation layers—equivalent to those exposed in the Southeast Pit—that were arched by diapirism to the level of the upper Lower Hebes Formation in the chasma walls. The mensa rose in response to extensional thinning, mass wasting, and flows off the mensa, all this deformation being in response to subsidence. This unroofing removed the youngest layers (Upper Hebes Formation and upper Lower Hebes Formation).

Amount of Diapiric Uplift of Hebes Mensa

To evaluate the amount of diapiric uplift, we return to the back-tilted dark smooth deposits and flows from the base of the north wall, which caused the axis of the North Pit to migrate outward several kilometers from the mensa (Fig. 23).

Figure 26A shows a present-day topographic profile and partial cross section across the chasma. To remove the northward tilt of the dark smooth deposits and restore its upper surface to an inferred originally horizontal attitude, we rotated the topographic profile 9° by pivoting on a hinge at the lowest point in the North Pit (Fig. 26B). After this 9° rotation, the ends of the flows from the north chasma wall sloped 3° southward throughout their length, which is compatible with an original flow direction before back tilting. The same 9° rotation of the north slope of the mensa lowered the base of LHF_B ~5 km to −2500 m, which is ~5 km below the present chasma rims (Fig. 26B). Projected outward, the altitude of the reconstructed base of LHF_B is near or below the base of the present chasma walls, which would explain why layers similar to those in the mensa are absent in the chasma walls but are present in the deep Southeast Pit. Backward in time, addition of ~5 km of material above the base of LHF_B before arching of the mensa would put the top of a protomensa at about the level of the present plains surface (Fig. 26C). Thus, if the plains surface, Upper Hebes Formation, and ~5 km of Lower Hebes Formation once existed over the mensa, and that material were removed by erosion and extensional thinning into the active drains, the mensa still would have to rise ~5 km diapirically to reach its present altitude.

The main diapiric mass inferred to be present in the core of Hebes Mensa and responsible for its arching would have a present-day relief of at least 5 km. Depending on whether this core is a concordant pillow (geometrically like a laccolith) or a discordant diapir, the original thickness of the source layer for the mobile core could have been 1 km to 4 km thick if analogy with terrestrial salt structures is valid (e.g., Worrall and Snelson, 1989; Diegel et al., 1995; Rowan, 1995; Gottschalk et al., 2004; Jackson et al., 2008).

Timing of Diapiric Uplift of Hebes Mensa

The flows across the floors of the North Trench and South Basin also hold the key to timing of arching. If the above restoration is correct, most of the uplift of the present mensa must have occurred after the surrounding pits and troughs had ceased to drain as they became blocked with allochthonous flows and choked by debris. Once the drains were blocked, the trenches provided solid surfaces on which the allochthonous flows, slides, and deposits of dark smooth deposits from the mensa now rest (Fig. 26B). Allochthonous flows from beneath the mensa and below the south chasma wall continued to resurface the western end of the South Basin. However, material shed from the mensa was not deposited on the surface of the western end of the South Basin or in the Southeast Pit. The Southeast Pit, which exposes deep outcrops of LHF_L at the bases of Hebes Mensa and Mini-Mensa, must have continued to drain after the mensae rose.

The key conclusion from this hypothesis is that the chasma collapsed and drained before most of the mensa arching occurred. The two processes are dynamically linked, so why should they be separated in time? The simplest

explanation is that the two processes differed in rate. Subsidence, drainage, and collapse were relatively rapid, perhaps even catastrophic. In contrast, diapiric uplift was slower, so although it began when subsidence began, uplift continued after collapse mostly ended as the drains clogged. Diapiric arching ended when the mensa was high enough that its elevation head restored static equilibrium to the mobile layer.

Removing the tilt in the North Trench places the base of LHF_B in the mensa within a kilometer or so of the surface of the floor of the chasma during deposition of the dark smooth deposits. Perhaps the botryoidal structures of LHF_B formed at the time depicted in Figure 26B. The botryoidal features resemble the small concentric diapirs and pimple-like mounds that still exist in the North Trench, features absent in the other pits and trenches. Before the main arching of the mensa, the botryoidal layer may have been a spring field for fluids emerging from the chasma floor. These fluids may have flushed dark particulates from out of fractures in the mensa and from the pimple-like mounds. Milliken et al. (2008) found similar botryoidal structures at several locations in Valles Marineris, all of which were associated with opaline silica deposits that they interpreted as having formed by low-temperature aqueous alteration.

Mini-Mensa is structurally similar to Hebes Mensa in that it is a pale antiform adjacent to pits and troughs. Outward-dipping layered rocks of LHF_L form the flanks of Mini-Mensa. Although not extensive enough to be mapped, a few botryoidal structures near the top of the mensa suggest that LHF_B may overlie LHF_L. Mini-Mensa and Hebes Mensa are separated by a fracture zone that extends deep into the Southeast Pit. The similarity of the two mensae implies a common diapiric origin.

Rheology of Mobilization

Some materials, such as ice or salts, are inherently mobile (for a review, see Talbot and Pohjola, 2009). Salt glaciers and rock mechanics show that halite and other weak salts can flow rapidly at surface temperatures on Earth (e.g., van Keken et al., 1993; Weijermars et al., 1993; Talbot, 1998). Other rocks need to be softened before they flow at geologically meaningful rates. Geologic observations from Hebes Chasma suggest a mixture of two softening processes: autochthonous mobilization and allochthonous mobilization.

Autochthonous Mobilization

During autochthonous mobilization, brittle material changes in situ to weaker viscous fluid with gradational contacts. Magmatic heating lowers viscosity of all rocks and liberates water from hydrous salts, ice, and hydrates. The hydrous salts, mirabilite and epsomite, could yield water at heat fluxes and depths estimated for Valles Marineris in Hesperian time (Montgomery et al., 2009). However, other hydrous salts such as gypsum need additional magmatic heat or burial to disassociate. The result at Hebes Chasma was a rheid mixture of solid remnants in a matrix of softened material below melting point. Evidence of autochthonous mobilization is best preserved at the east end of Hebes Chasma (Fig. 21) in the westward gradation from (1) a wall bench resembling downdropped plains surface, through (2) the same material but partly broken into blocks and partly deformed by flow (forming hummocks, lobes, transverse wrinkles and scarps, and some longitudinal streaks), to (3) the Tongue, a mature flow having a smooth surface marked by a dense array of longitudinal streaks. This gradation is over a lateral distance of 20 km (the width of the WB_F) and a vertical distance of little more than 1 km. This narrow depth span contains the loose equivalent of a metamorphic isograd across which material softened with depth. The isograd is now 4–5 km below the rim. It is uncertain whether metamorphism was presubsidence (depth 4–5 km) or postsubsidence (depth ~1 km), or synsubsidence. During later cooling, a prograde metamorphic sequence that softens the mobile material could reverse as a retrograde sequence.

Allochthonous Mobilization

The previous paragraph suggests that softening mobilized material at depths of more than 5 km. After being tectonically unroofed, allochthonous flows broke out at the surface and flowed over bedrock, surficial deposits, and older flows (Fig. 18). The mobility of these flows suggests that they may have retained higher temperatures from depth. Contacts of allochthonous flows are sharp, and their emplacement was less like metamorphism and more like lava flows or salt glaciers (Fig. 20). The head of the flows emerged already stretched by subsurface flow, as shown by longitudinal streaks. In many places in the mid-to-lower slopes of the chasma walls and mensa flanks, vast lumpy flows emerged and flooded over the chasma floors toward the pits and drains (Figs. 22 and 23). The dynamics are closely analogous to allochthonous salt sheets on Earth: A mobile source layer kilometers deep feeds diapirs, which extrude as salt glaciers from surface vents.

Extent of Collapse

Collapse of Hebes Chasma implies weak material, but how widespread were these mobile units? To test the spatial limits of mobility, model 3 had a mobile layer (unit 3) reaching the edges of the entire model. As this model chasma subsided, extension spread outward far beyond the chasma to the outer edges of the model (Fig. DR6 [see footnote 1]). Major grabens encircled the model chasma rim and extended outward as far as the weak layer was present. The boundary of the chasma was gradational, not sharp as in model 1 (Figs. 11A and 11B) or in Hebes Chasma, which has a sharp, steep rim, beyond which the plains surface is flat with no significant relief or extension (Fig. 11C). Hebes Chasma thus resembles the chasmas of model 1 and model 2, in which weakness was purely local.

Local mobility of Hebes Chasma could have had two causes. Either the chasma formed where rocks were locally weak, or the chasma formed where local heating softened layered deposits that are also widespread beyond the chasma. If weak layers are indeed widespread on Mars, their mobilizing agent in Hebes Chasma was local. A likely agent is a combination of fracturing and advection of heat. Fracturing provided plumbing, and heat dewatered salts and melted ices and gas hydrates in a local area that subsided to form Hebes Chasma. This heating may have been part of the Tharsis magmatic episodes.

Composition and Mechanical Behavior of Materials

Landslides, Magma, Ice

Planetary geologists have interpreted large viscous flows at the Martian surface as landslides, lava flows, or glacial ice. Could these materials have formed the deep-sourced or shallow-sourced allochthonous flows in Hebes Chasma?

Martian landslides have been inferred from their morphology and low thermal inertia (Farrand and Gaddis, 2003; Skinner and Tanaka, 2007; Skinner and Mazzini, 2009). The geologic map of Valles Marineris by Witbeck et al. (1991) shows an *AS* map unit that they interpreted as slumps and landslides. Landslides are present at Hebes and are an integral result of collapse in the model. These range from incipient slumps to long-runout debris avalanches. Rock avalanches, especially, cannot always be distinguished from allochthonous flows, but several features suggest that most large flows in Hebes Chasma are not landslides. (1) Some flows emerged from the side or base of the chasma wall with no sign of a headwall alcove from which a landslide could have originated. (2) Few flows have an extensional zone of transverse scarps at their head. (3) Some flows emerge from the walls as lumpy and bulbous,

which is characteristic of the compressional toe of a landslide, but not its head. (4) Some flows emerge with longitudinal streaks, suggesting that they began flowing underground. (5) Some flows contain deformed layering continuous with stratigraphic layering at their source.

Evidence of volcanic flows in Hebes Chasma is sparse. Volcanic ash is likely to be part of the stratigraphy of Hebes Chasma; the nearest major volcano, Tharsis Tholis, is 1100 km away. The dark deposits filling gullies down the flanks of Hebes Mensa and ponding at its base have been interpreted as low-viscosity lava flows, as has the entire Hebes Mensa, by Ori et al. (2005). However, we interpret the dark deposits as particulates weathered from the Lower Hebes Formation and probably entrained in the outflow of aqueous springs, as discussed in Adams et al. (2009). Similarly, the large allochthonous flows in the floor of Hebes Chasma are unlikely to consist of lava for the following reasons. (1) The flows are too viscous to be mafic. Their flow morphology suggests a viscosity similar to that of felsic lavas, but felsic volcanic flows issue from cones or agglutinate ridges, which are not recognized at Hebes. (2) Hebes flows end in pits. (3) Why lavas would be expelled laterally from the walls of collapse structures but not from the surrounding plains is unexplained. (4) Hebes Chasma is not a volcanic caldera. (5) Volcanic flows explain neither the huge subsidence nor the proximity to giant floods in Echus Chasma.

Water ice has an important role near the surface of Mars, as evidenced by a wide range of landforms and landscapes (reviewed by Kargel, 2004; Baker, 2006), by remote sensing (Bandfield, 2007), and by direct observation of ice- and water-associated minerals (Smith et al., 2009). Melting ice could have released huge volumes of water, the drainage of which into an aquifer would have contributed to collapse of Hebes Chasma (Montgomery and Gillespie, 2005). Ice may be part of some chasma flows. For example, the North Flow falls 1.9 km over 41 km, an average slope of 2.7°. Its profile is equivalent to the viscous response of an ice glacier containing ~20% rock debris under Martian temperatures and gravity (Bourgeois et al., 2008).

Ice has its limits. (1) Ice is too weak to bear canyon relief of 8 km, so any ice in the canyon walls must be locked in pore space by the frictional strength of non-ice particles. (2) Surface ice ablates and shrinks at a rate determined by the thickness of insulating rubble. After surviving billions of years of exposure, the pale material cropping out in the flows is unlikely to be ice, although it may have been more icy during flow. (3) Glacial ice flows are not expected to come from the subsurface (although Mars still has many surprises and water seeping from the ground could locally freeze as sheets of aufeis; Kargel, 2004).

Gas hydrates and pockets of free gas trapped in the cryosphere also may have contributed water. Methane and carbon dioxide gas trapped within the crystal lattice of water ice could be stable on Mars within the water-ice cryosphere from near surface to as much as a kilometer below the base of the cryosphere (Hoffman, 2000; Pellenbarg et al., 2003). Magmatic warming and pressure release from structural unroofing during subsidence could liberate gas, which bubbled upward, and water, which drained downward.

Role of Salts

As Mars became drier and colder, salts could have formed as evaporites as salty water evaporated, not necessarily from standing bodies of water (Forsythe and Zimbelman, 1995; Mancinelli et al., 2004; Squyres et al., 2004; Tosca et al., 2005), or salts could have formed by hydrothermal precipitation and replacement in the subsurface at supercritical temperatures above 405 °C (Hovland et al., 2006a, 2006b). We have speculated elsewhere that parts of the Martian megaregolith are rich in water, salts, and tephra (Montgomery and Gillespie, 2005; Bigot-Cormier and Montgomery, 2007; Adams et al., 2009; Montgomery et al., 2009). In the present paper, we refer to "layered deposits" without connoting their origin, whether by impact, volcanism, or sedimentation. Layered deposits in any prechasma basins on Mars could include significant proportions of salts, which can form in a wide range of concentrations as discrete layers or cements, as proposed by Montgomery and Gillespie (2005).

As a weak constituent of Martian layered deposits, salts have some advantages over ice in explaining how Hebes Chasma collapsed. (1) There are no inherent depth limits for buried salts, unlike the cryosphere, which is limited to a depth of only a kilometer or two, depending on the latitude and the geothermal gradient. (2) Salt does not sublimate like ice and so can survive on the surface for billions of years without rainfall. (3) Hydrous salts, such as kieserite, epsomite, hexahydrite, and gypsum, have been identified spectroscopically on Mars, including in Hebes Chasma (Gendrin et al., 2005; Hauber et al., 2006, 2008; Adams et al., 2009). These occurrences include an unknown proportion of halite and other anhydrous salts, which are spectroscopically difficult to detect on Mars. (4) Most salts flow readily and are the weakest crystalline rocks. (5) Hydrous salts disassociate on heating and yield water that can drain away, shrinking the host rocks.

Like ices, salts have strength limits. On Earth, salt mountains above diapirs spread under their own weight to form salt glaciers that advance subaerially at rates up to 10 m/yr (Talbot and Pohjola, 2009). Larger salt glaciers advance more slowly at up to 8–20 mm/yr underwater (Jackson et al., 1994). The equilibrium slope of terrestrial salt glaciers is similar to that of the deep-sourced flows from the chasma walls, although we are not implying that the chasma flows necessarily consist mostly of halite. The North Flow's average slope is 2.7°. By comparison, one of the largest shallow allochthonous salt flows in the Gulf of Mexico falls 1.7 km over 40 km, an average slope of 2.4° (Schultz-Ela and Jackson, 1996). The walls of Hebes Chasma are too steep to consist of pure salts. For this reason, we infer that when first excavated, the upper walls consisted of a mixture of insoluble particles such as tephra and rubble with lesser amounts of sulfate and other salts, and water in solid form near the surface and liquid at depth. The lower walls could have been richer in weaker salts and contributed more to subsidence. The spectroscopic distribution of the salts in Hebes Chasma is discussed by Adams et al. (2009).

Disintegration and Deep Fluid Transport from Hebes Chasma

In the model, the brittle upper layers broke into rafted blocks, lumps, or particulate flows (Figs. 7, 8, 9, and 10). The Hebes Group also broke up as fault blocks cascading inward to the drainage pits (Figs. 16 and 21). Although Martian gravity is only one third that on Earth, the body forces breaking blocks in Hebes would have been much greater than in the model because body forces increase at a cubed proportion of the length scale (Hubbert, 1937).

Crumbling blocks increase surface area, which would hasten melting or sublimation of any freshly exposed ice or gas hydrate, causing further comminution. Some weathered material may have drained into the aquifer through a multitude of fissures in the fractured floor, organized along preexisting faults. Even so, there is unlikely to be sufficient space in the subsurface for the solid fraction of missing material, and the aquifer may have been saturated even before collapse began. Groundwater must have been expelled onto the surface to make room for the lost material, which must have been mostly water or other fluids, including gas. The most obvious route to the surface could have been as short as 5 km to the head of the Echus Chasma outburst flood into Kasei Valles.

As fluids drained from the collapsing Hebes Chasma, local pressure in the aquifer eventually

fell below the pressure under the adjacent plains. Brine from the regional aquifer beneath the plains may thus have leaked laterally into the chasma floor as the canyon widened. If so, any brine could have evaporated to leave another contribution of salt.

Summary of Events

We interpret here landforms in Hebes Chasma guided by insights from the physical models and identify a wide range of Hebes landforms consistent with karstic collapse. Our evolutionary model may apply elsewhere on Mars, especially in the neighboring Valles Marineris, but a comparative survey of other chasmata is beyond the scope of this paper. Here, we summarize and illustrate (Fig. 27) the inferred sequence of events at Hebes, the causes and effects of which are only partly understood.

Valles Marineris canyons, including Hebes Chasma, may have begun forming near the Noachian-Hesperian boundary, at ca. 3.7 Ga (Carr and Head, 2010). Instability started with local warming above the normal geothermal gradient in part of the planet dominated by large fracture systems striking west-northwest. Heating could have resulted from local magmatic heating, possibly as a local expression of Tharsis magmatism, or concentrated fractures could have focused advection of hot fluids from depth. Melting of permafrost ice and perhaps gas hydrates in the uppermost kilometer or two of layered deposits in the chasma walls and thermal dewatering of hydrous salts at all levels freed copious amounts of water and gas.

Fluids derived by melting and dewatering and some fraction of suspended materials began to drain through fractures into the aquifer, especially at intersections or concentrations of large fracture zones. Much of the drained fluids burst out where the aquifer intersected the surface, as at Echus Chasma. The enormous flux of fluids inferred for Echus Chasma suggests that the outburst received water and other liquids and gases from elsewhere besides Hebes Chasma.

The first surface sign of deep drainage was sagging of the plains surface as gentle swales above the most active drains (Figs. 6A and 27A). Within each sag, the plains surface tilted inward, hinging on peripheral grabens and overriding in a contractional crease in the floor of each swale.

Further subsidence caused surface layers to slide above weak material into pits (Figs. 6B and 27B). Sliding brittle material broke into fault benches and then slabs and smaller pieces that crumbled and drained away. Extensional breakaways for these inward slides spread outward in response to inward collapse (Fig. 6C). These extensional zones were curved and concentric to erosional headwalls in the chasma and were influenced by two sets of regional extensional faults.

Landslides occurred where subsidence oversteepened the chasma (Fig. 27C). As material drained into the deepening pits, this unroofed warmer and softer material near the base of the chasma walls. Unconfined allochthonous flows extruded laterally from the chasma and mensa walls into the pits. These extrusions sapped and undermined the stronger overburden. All the displaced material—benches, slabs, landslides, talus, and allochthonous flows—moved toward drainage pits in the chasma floor. The chasma floor began to break up by brittle rupture and

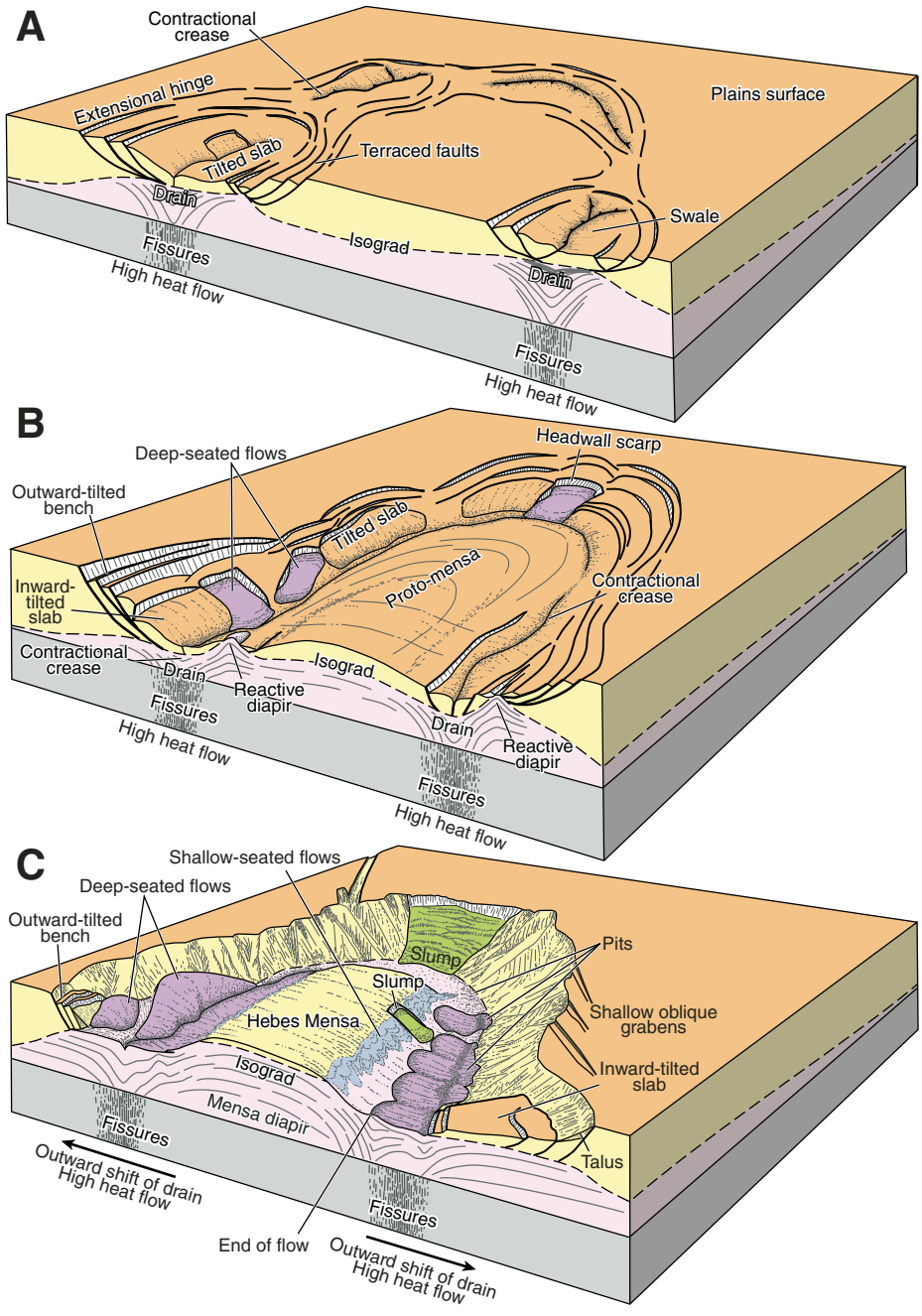

Figure 27. Block diagrams showing three phases (A, B, and C) in the evolution of Hebes Chasma inferred in this paper and described in the "Summary of Events." The isograd marks the upper limit of mobilized material. Views, which are not to scale, are toward the southwest.

viscous flow to form chaos terrain. Collapse spread outward to the edge of the mobilized material at the chasma margins (Fig. 6D).

Warm, mobile material rose diapirically from depth because it was less dense than its overburden and because of differential loading induced by exhumation (Figs. 27B and 27C). Diapirism focused where the overburden was most thinned by extension, mass wasting, and flow into the drainage pits.

Hebes Mensa and Mini-Mensa are islands of stratigraphically deep rocks surrounded by collapse pits. After their roofs slid and flowed into the pits and the allochthonous flows had covered the clogged drains, the mensae warped into box-shaped antiforms by diapiric arching and extensional sagging of their flanks (Figs. 27B and 27C). As Hebes Mensa arched, it back tilted some allochthonous flows and dark deposits and displaced the drainage depressions outward by up to 10 km. This arching was late in the evolution of Hebes Chasma and postdates heavy bombardment, as implied by the absence of large craters in the mensa's crest (Rossi et al., 2008).

After drainage into the pits ended, surficial deposits, many of them dark, continued to weather out of slopes or blew into the chasma and accumulated in the pits and on top of Hebes Mensa.

This new view of how Hebes Chasma formed, together with the findings of Adams et al. (2009), links many otherwise perplexing features, especially the origin of Hebes Mensa, which has been especially enigmatic. Formation of Hebes Chasma by karstic collapse and drainage followed by arching of its unroofed floor to form the mensa explains otherwise puzzling topography and stratigraphy with a single genetic process involving both drainage and upwelling. Similar processes may have helped form other chasmata of Valles Marineris, but each chasmata did not necessarily form in the same way.

ACKNOWLEDGMENTS

The Applied Geodynamics Laboratory consortium funded Jackson's and Dooley's work. National Aeronautics and Space Administration (NASA) Mars Data Analysis Program grant NNX07AV77G contributed support for Gillespie. We had useful discussions with J.-P. Combe, G. Skerlec, and B.C. Schreiber. Thorough reviews by C. Okubo and E. Hauber greatly improved the paper. T.B. McCord provided technical support; figures were drawn mostly by the authors but also by Nancy Cottington and Laura Gilson; Lana Dieterich edited the paper. This contribution is published with permission of the Director, Bureau of Economic Geology.

REFERENCES CITED

Adams, J.B., Gillespie, A.R., Jackson, M.P.A., Montgomery, D.R., Dooley, T.P., Combe, J.-P., and Schreiber, B.C., 2009, Salt tectonics and collapse of Hebes Chasma, Valles Marineris, Mars: Geology, v. 37, p. 691–694, doi: 10.1130/G30024A.1.

Anderson, S., and Grimm, R.E., 1998, Rift processes at the Valles Marineris, Mars: Constraints from gravity on necking and rate-dependent strength evolution: Journal of Geophysical Research, v. 103, p. 11,113–11,124.

Anguita, F., Fernández, C., Cordero, G., Carrasquilla, S., Anguita, J., Núñez, A., Rodríguez, S., and García, J., 2006, Evidences for a Noachian-Hesperian orogeny in Mars: Icarus, v. 185, p. 331–357, doi: 10.1016/j.icarus.2006.07.026.

Baikpour, S., Zulauf, G., Dehghani, M., and Bahroudi, A., 2010, InSAR maps and time series observations of surface displacements of rock salt extruded near Garmsar, northern Iran: Journal of the Geological Society, v. 167, p. 171–181, doi: 10.1144/0016-76492009-058.

Baioni, D., and Wezel, F.C., 2008, Similarities of a Martian dome with terrestrial salt domes: Italian Journal of Geoscience, v. 127, p. 453–465.

Baker, V.R., 2006, Geomorphological evidence for water on Mars: Elements, v. 2, p. 139–143, doi: 10.2113/gselements.2.3.139.

Bandfield, J.L., 2007, High-resolution subsurface water-ice distributions on Mars: Nature, v. 447, p. 64–67, doi: 10.1038/nature05781.

Beyer, R.A., and McEwen, A., 2005, Layering stratigraphy of eastern Coprates and northern Capri Chasmata, Mars: Icarus, v. 179, p. 1–23, doi: 10.1016/j.icarus.2005.06.014.

Bigot-Cormier, F., and Montgomery, D.R., 2007, Valles Marineris landslides: Strength limit to Martian relief?: Earth and Planetary Science Letters, v. 260, p. 179–186, doi: 10.1016/j.epsl.2007.05.028.

Blasius, K. R., Cutts, J. A., Guest, J. E., and Masursky, H., 1977, Geology of the Valles Marineris: First analysis of imaging from the *Viking 1 Orbiter* primary mission: Journal of Geophysical Research, v. 82, p. 4067–4091.

Bleamaster, L.F., III, 2009, A dynamic mechanism for Valles Marineris formation: Proceedings of the 40th Lunar and Planetary Science Conference, p. 2552.

Bourgeois, O., Devismes, D., and Cevatoglu, M., 2008, The rheology of ice-rock mixtures inferred from analogue models: Application to the gravitational flow of Martian superficial formations: Proceedings of the 39th Lunar and Planetary Science Conference, p. 1260.

Bruthans, J., Asadi, N., Filippi, M., Vilhelm, Z., and Zare, M., 2008, A study of erosion rates on salt diapir surfaces in the Zagros Mountains, SE Iran: Environmental Geology, v. 53, p. 1079–1089, doi: 10.1007/s00254-007-0734-6.

Bruthans, J., Filippi, M., Asadi, N., Zare, M., Šlechta, S., and Churáčková, Z., 2009, Surficial deposits on salt diapirs (Zagros Mountains and Persian Gulf Platform, Iran): Characterization, evolution, erosion and the influence on landscape morphology: Geomorphology, v. 107, p. 195–209, doi: 10.1016/j.geomorph.2008.12.006.

Carr, M.H., and Head, J.W., III, 2010, Geologic history of Mars: Earth and Planetary Science Letters, v. 294, p. 185–203, doi: 10.1016/j.epsl.2009.06.042.

Chadwick, D.J., and Lucchitta, B.K., 1993, Fault geometries and extension in the Valles Marineris, Mars: Proceedings of the 24th Lunar and Planetary Science Conference, p. 263–264.

Chemia, Z., and Koyi, H., 2008, The control of salt supply on entrainment of an anhydrite layer within a salt diapir: Journal of Structural Geology, v. 30, p. 1192–1200, doi: 10.1016/j.jsg.2008.06.004.

Courtillot, V.E., Allegre, C.J., and Mattauer, M., 1975, On the existence of lateral relative motions on Mars: Earth and Planetary Science Letters, v. 25, p. 279–285, doi: 10.1016/0012-821X(75)90242-3.

Davison, I., Alsop, I., Birch, P., Elders, C., Evans, N., Nicholson, H., Rorison, P., Wade, D., Woodward, J., and Young, M., 2000, Geometry and late-stage structural evolution of Central Graben salt diapirs, North Sea: Marine and Petroleum Geology, v. 17, p. 499–522, doi: 10.1016/S0264-8172(99)00068-9.

Diegel, F.A., Karlo, J.F., Schuster, D.C., Shoup, R.C., and Tauvers, P.R., 1995, Cenozoic structural evolution and tectono-stratigraphic framework of the northern Gulf Coast continental margin, *in* Jackson, M.P.A., Roberts, D.G., and Snelson, S., eds., Salt Tectonics: A Global Perspective: American Association of Petroleum Geologists Memoir 65, p. 109–151.

Dixon, J.M., 1975, Finite strain and progressive deformation in models of diapiric structures: Tectonophysics, v. 28, p. 89–124, doi: 10.1016/0040-1951(75)90060-8.

Farrand, W.H., and Gaddis, L.R., 2003, *Themis* observations of pitted cones in Acidalia Planita and Cydonia Mensae, *in* 6th International Conference on Mars: Houston, Texas, Lunar and Planetary Institute, p. 3094.

Forsythe, R.D., and Zimbelman, J.R., 1995, A case for ancient evaporite basins on Mars: Journal of Geophysical Research, v. 100, p. 5553–5563, doi: 10.1029/95JE00325.

Frey, H., 1979, Martian canyons and African rifts: Structural comparisons and implications: Icarus, v. 37, p. 142–155, doi: 10.1016/0019-1035(79)90122-2.

Fueten, F., Stesky, R.M., and MacKinnon, P., 2005, Structural attitudes of large scale layering in Valles Marineris, Mars, calculated from Mars Orbiter Laser Altimeter data and Mars Orbiter Camera imagery: Icarus, v. 175, p. 68–77, doi: 10.1016/j.icarus.2004.11.010.

Gendrin, A., Mangold, N., Bibring, J.-P., Langevin, Y., Gondet, B., Poulet, F., Bonello, G., Quantin, C., Mustard, J., Arvidson, R., LeMouélic, S., and the OMEGA Team, 2005, Sulfates in Martian layered terrains: The OMEGA/*Mars Express* view: Science, v. 307, no. 5715, p. 1587–1591, doi: 10.1126/science.1109087.

Gindrod, P.M., and Balme, M.R., 2010, Groundwater processes in Hebes Chasma, Mars: Proceedings of the 41st Lunar and Planetary Science Conference, p.1311.

Gottschalk, R.R., Anderson, A.V., Walker, J.D., and Da Xilva, J.C., 2004, Modes of contractional salt tectonics in Angola Block 33, Lower Congo basin, West Africa, *in* Post, P.J., et al., eds., Salt-Sediment Interactions and Hydrocarbon Prospectivity: Concepts, Applications, and Case Studies for the 21st Century, 24th Annual Research Conference: Houston, Texas, Society of Economic Paleontologists and Mineralogists Foundation, p. 705–734.

Gudmundsson, M.T., Sigmundsson, F., and Björnsson, H., 1997, Ice-volcano interaction of the 1996 Gjálp subglacial eruption, Vatnajökull, Iceland: Nature, v. 389, p. 954–957, doi: 10.1038/40122.

Harrison, J.C., and Jackson, M.P.A., 2008, Bedrock Geology, Strand Fiord–Expedition Fiord Area, Western Axel Heiberg Island, Northern Nunavut (Parts of NTS 59E, F, G, and H): Geological Survey of Canada Open-File 5590, CD-ROM.

Hauber, E., Gwinner, K., Stesky, R., Fueten, F., Michael, G., Reiss, D., Zegers, T., Hoffman, H., Jaumann, R., van Gasselt, S., and Neukum, G., 2005, Interior layered deposits in Valles Marineris, Mars: Insights from 3D-data obtained by the high-resolution stereo camera (HRSC): Proceedings of the 36th Lunar and Planetary Science Conference, p. 1760.

Hauber, E., Gwinner, K., Gendrin, A., Fueten, F., Stesky, R., Pelkey, S., Wulf, H., Reiss, D., Zegers, T., MacKinnon, P., Michael, G., Jaumann, R., Binring, J.-P., Neukum, G., and the HRSC Co-Investigator Team, 2006, An integrated study of interior layered deposits in Hebes Chasma, Valles Marineris, Mars, using MGS, MO, and MEX data: Proceedings of the 37th Lunar and Planetary Science Conference, p. 2022.

Hauber, E., Gwinner, K., Gendrin, A., Fueten, F., Stesky, R., Pelkey, S., Reiss, D., Zegers, T., MacKinnon, P., Jaumann, R., Bibring, J.-P., and Neukum, G., 2008, Hebes Chasma, Mars: Slopes and stratigraphy of interior layered deposits: Proceedings of the 39th Lunar and Planetary Science Conference, p. 2375.

Hoffman, N., 2000, White Mars: A new model for Mars' surface and atmosphere based on CO_2: Icarus, v. 146, p. 326–342, doi: 10.1006/icar.2000.6398.

Hovland, M., Kuznetsova, T., Rueslåtten, H., Kvamme, B., Johnsen, H.K., Fladmark, G.E., and Hebach, A., 2006a, Sub-surface precipitation of salts in supercritical seawater: Basin Research, v. 18, p. 221–230, doi: 10.1111/j.1365-2117.2006.00290.x.

Hovland, M., Rueslåtten, H.G., Johnsen, H.K., Kvamme, B., and Kuznetsova, T., 2006b, Salt formation associated with sub-surface boiling and supercritical water: Marine and Petroleum Geology, v. 23, p. 855–869, doi: 10.1016/j.marpetgeo.2006.07.002.

Hubbert, M.K., 1937, Theory of scale models as applied to the study of geological structures: Geological Society of America Bulletin, v. 48, p. 1459–1520.

Hudec, M.R., and Jackson, M.P.A., 2006, Advance of allochthonous salt sheets in passive margins and orogens: American Association of Petroleum Geologists (AAPG) Bulletin, v. 90, p. 1535–1564, doi: 10.1306/05080605143.

Hudec, M.R., and Jackson, M.P.A., 2007, Terra infirma: Understanding salt tectonics: Earth-Science Reviews, v. 82, p. 1–28, doi: 10.1016/j.earscirev.2007.01.001.

Hudec, M.R., and Jackson, M.P.A., 2009, Interaction between spreading salt canopies and their peripheral thrust systems: Journal of Structural Geology, v. 31, p. 1114–1129, doi: 10.1016/j.jsg.2009.06.005.

Jackson, M.P.A., and Talbot, C.J., 1989, Anatomy of mushroom-shaped diapirs: Journal of Structural Geology, v. 11, p. 211–230, doi: 10.1016/0191-8141(89)90044-8.

Jackson, M.P.A., Cornelius, R.R., Craig, C.H., Gansser, A., Stöcklin, J., and Talbot, C.J., 1990, Salt Diapirs of the Great Kavir, Central Iran: Geological Society of America Memoir 177, 139 p.

Jackson, M.P.A., Vendeville, B.C., and Schultz-Ela, D.D., 1994, Structural dynamics of salt systems: Annual Review of Earth and Planetary Sciences, v. 22, p. 93–117, doi: 10.1146/annurev.ea.22.050194.000521.

Jackson, M.P.A., Hudec, M.R., Jennette, D.C., and Kilby, R.E., 2008, Evolution of the Cretaceous Astrid thrust belt in the ultradeep-water Lower Congo Basin, Gabon: American Association of Petroleum Geologists (AAPG) Bulletin, v. 92, p. 487–511, doi: 10.1306/12030707074.

Kargel, J.S., 2004, Mars: A Warmer, Wetter Planet: Chichester, United Kingdom, Springer Praxis, 557 p.

Kent, P.E., 1979, The emergent Hormuz salt plugs of southern Iran: Journal of Petroleum Geology, v. 2, p. 117–144, doi: 10.1111/j.1747-5457.1979.tb00698.x.

Le Deit, L., Le Mouélic, S., Bourgeois, O., Combe, J.-P., Mège, D., Sotin, C., Gendrin, A., Hauber, E., Mangold, N., and Bibring, J.-P., 2008, Ferric oxides in East Candor Chasma, Valles Marineris (Mars), inferred from analysis of OMEGA/*Mars Express* data: Identification and geological interpretation: Journal of Geophysical Research–Planets, v. 113, no. E7, E07001, doi: 10.1029/2007JE002950.

Lucchitta, B.K., 1979, Landslides in Valles Marineris, Mars: Journal of Geophysical Research, v. 84, no. B14, p. 8097–8113, doi: 10.1029/JB084iB14p08097.

Lucchitta, B.K., and Chapman, M.G., 2002, Are the Valles Marineris giant volcano-tectonic depressions?: Proceedings of the 33rd Lunar and Planetary Science Conference, p. 1689.

Lucchitta, B.K., Clow, G.D., Geissler, P.E., McEwen, A.S., Schultz, R.A., Singer, R.B., and Squyres, S.W., 1992, The canyon system on Mars, *in* Kieffer, H.H., et al., eds., Mars: Tucson, University of Arizona Press, p. 453–492.

Malin, M.C., and Edgett, K.S., 2000, Sedimentary rocks of early Mars: Science, v. 290, p. 1927–1937, doi: 10.1126/science.290.5498.1927.

Malin, M.C., and Edgett, K.S., 2001, Global Surveyor Mars Orbital Camera; interplanetary cruise through primary mission: Journal of Geophysical Research, v. 106, no. E10, p. 23,429–23,570, doi: 10.1029/2000JE001455.

Mancinelli, R.L., Fahlen, T.F., Landheim, R., and Klovstad, M.R., 2004, Brines and evaporites: Analogs for Martian life: Advances in Space Research, v. 33, p. 1244–1246, doi: 10.1016/j.asr.2003.08.034.

Masson, P., 1977, Structure pattern analysis of the Noctis Labyrinthus–Valles Marineris regions of Mars: Icarus, v. 30, p. 49–62, doi: 10.1016/0019-1035(77)90120-8.

Masson, P., 1985, Origin and evolution of the Valles Marineris region of Mars: Advances in Space Research, v. 5, no. 8, p. 83–92, doi: 10.1016/0273-1177(85)90244-3.

McCauley, J.F., Carr, M.H., Cutts, J.A., Hartmann, W.K., Masursky, H., Milton, D.J., Sharp, R.P., and Wilhelms, D.E., 1972, Preliminary *Mariner 9* report on the geology of Mars: Icarus, v. 17, p. 289–327, doi: 10.1016/0019-1035(72)90003-6.

McEwen, A.S., Malin, M.C., Carr, M.H., and Hartmann, W.K., 1999, Voluminous volcanism on early Mars revealed in Valles Marineris: Nature, v. 397, p. 584–586, doi: 10.1038/17539.

Mège, D., and Masson, P., 1996, Amounts of crustal stretching in Valles Marineris, Mars: Planetary and Space Science, v. 46, p. 345–356.

Milliken, R.E., Grotzinger, J., Beyer, R.A., Muchie, S., McEwen, A., and the CRISM Science Team, 2007, Evidence for salt tectonics in Valles Marineris, *in* 7th International Conference on Mars: Houston, Texas, Lunar and Planetary Institute, p. 3383.

Milliken, R.E., Swayze, G.A., Arvidson, R.E., Bishop, J.L., Clark, R.N., Ehlmann, B.L., Green, R.O., Grotzinger, J.P., Morris, R.V., Murchie, S.L., Mustard, J.F., and Weitz, C., 2008, Opaline silica in young deposits on Mars: Geology, v. 36, p. 847–850, doi: 10.1130/G24967A.1.

Mitchell, N.C., Ligi, M., Ferrante, V., Bonatti, E., and Rutter, E., 2010, Submarine salt flows in the central Red Sea: Geological Society of America Bulletin, v. 122, p. 701–713, doi: 10.1130/B26518.1.

Montgomery, D.R., and Gillespie, A., 2005, Formation of Martian outflow channels by catastrophic dewatering of evaporite deposits: Geology, v. 33, p. 625–628, doi: 10.1130/G21270.1.

Montgomery, D.R., Som, S.M., Jackson, M.P.A., Schreiber, B.C., Gillespie, A.R., and Adams J.B., 2009, Continental-scale salt tectonics on Mars and the origin of Valles Marineris and associated outflow channels: Geological Society of America Bulletin, v. 121, p. 117–133.

Nahm, A.L., and Schultz, R.A., 2010, Evaluation of the orogenic belt hypothesis for the formation of the Thaumasia Highlands, Mars: Journal of Geophysical Research, v. 115, E04008, 14 p.

Nedell, S.S., Squyres, S.W., and Anderson, D.W., 1987, Origin and evolution of the layered deposits in the Valles Marineris, Mars: Icarus, v. 70, p. 409–414, doi: 10.1016/0019-1035(87)90086-8.

Nelson, T.H., 1991, Salt tectonics and listric-normal faulting, *in* Salvador, A., ed., The Gulf of Mexico Basin: Boulder, Colorado, Geological Society of America, The Geology of North America, v. J, p. 73–89.

Ori, G. G., Pacifici, A., Komatsu, G., Neukum, G., and the HRSC Science Team, 2005, A probable fluid lava flow in the Hebes Mensa (Mars) studied by HRSC images: Proceedings of the 36th Lunar and Planetary Science Conference, p. 1648.

Pellenbarg, R.E., Max, M.D., and Clifford, S.M., 2003, Methane and carbon dioxide hydrates on Mars: Potential origins, distribution, detection, and implications for future in situ resource utilization: Journal of Geophysical Research, v. 108, Pt. 4, doi: 10.1029/2002JE001901.

Peulvast, J.-P., and Masson, P.L., 1993, Erosion and tectonics in central Valles Marineris (Mars): A new morphostructural model: Earth, Moon, and Planets, v. 61, p. 191–217, doi: 10.1007/BF00572245.

Peulvast, J.-P., Mège, D., Chiciak, J., Costard, F., and Masson, P.L., 2001, Morphology, evolution and tectonics of Valles Marineris wallslopes (Mars): Geomorphology, v. 37, p. 329–352, doi: 10.1016/S0169-555X(00)00085-4.

Popa, C.I., Esposito, F., Ori, G.G., Marinangeli, L., and Colangeli, L., 2007, Tithonium Chasma domes: A result of salt diapirism by means of thin-skinned extension?: Proceedings of the 38th Lunar and Planetary Science Conference, p. 1848.

Ramberg, H., 1981, Gravity, Deformation and Earth's Crust in Theory, Experiments and Geological Application (2nd ed.): London, Academic Press, 452 p.

Richter-Bernburg, G., 1987, Deformation within salt bodies, *in* Lerche, I., and O'Brien, J.J., Dynamical Geology of Salt and Related Structures: Orlando, Florida, Academic Press, p. 39–75.

Robinson, M.S., and Tanaka, K.L., 1990, Magnitude of a catastrophic flood event at Kasei Valles, Mars: Geology, v. 18, p. 902–905, doi: 10.1130/0091-7613(1990)018<0902:MOACFE>2.3.CO;2.

Rodríguez, J.A.P., Kargel, J., Crown, D.A., Bleamaster, L.F., III, Tanaka, K.L., Baker, V., Miyamoto, H., Dohm, J.M., Sasaki, S., and Komatsu, G., 2006, Headward growth of chasmata by volatile outbursts, collapse, and drainage: Evidence from Ganges chaos, Mars: Geophysical Research Letters, v. 33, L18203, doi: 10.1029/2006GL026275.

Rossi, A.P., Neukum, G., Pondrelli, M., van Gasselt, S., Zegers, T., Hauber, E., Chicarro, A., and Foing, B., 2008, Large-scale spring deposits on Mars?: Journal of Geophysical Research, v. 113, E08016, doi: 10.1029/2007JE003062, 17 p.

Rowan, M.G., 1995, Structural styles and evolution of allochthonous salt, central Louisiana outer shelf and upper slope, *in* Jackson, M.P.A., Roberts, D., and Snelson, S., eds., Salt Tectonics: A Global Perspective: American Association of Petroleum Geologists (AAPG) Memoir 65, p. 199–228.

Schléder, Z., and Urai, J.L., 2007, Deformation and recrystallization mechanisms in mylonitic shear zones in naturally deformed extrusive Eocene–Oligocene rocksalt from Eyvanekey plateau and Garmsar hills (central Iran): Journal of Structural Geology, v. 29, p. 241–255, doi: 10.1016/j.jsg.2006.08.014.

Schonfeld, E., 1979, Origin of Valles Marineris: Proceedings of the 10th Lunar and Planetary Science Conference, p. 1064–1065.

Schultz, R.A., 1991, Structural development of Coprates Chasma and western Ophir Planum, central Valles Marineris rift, Mars: Journal of Geophysical Research, v. 96, p. 22,777–22,792, doi: 10.1029/91JE02556.

Schultz, R.A., 1995, Gradients in extension and strain at Valles Marineris, Mars: Planetary and Space Science, v. 43, p. 1561–1566.

Schultz, R.A., 1998, Multiple-process origin of Valles Marineris basins and troughs, Mars: Planetary and Space Science, v. 46, p. 827–829, doi: 10.1016/S0032-0633(98)00030-0.

Schultz, R.A., and Lin, J., 2001, Three-dimensional normal faulting models of the Valles Marineris, Mars, and geodynamic implications: Journal of Geophysical Research, v. 106, p. 16,549–16,566, doi: 10.1029/2001JB000378.

Schultz-Ela, D.D., and Jackson, M.P.A., 1996, Relation of subsalt structures to suprasalt structures during extension: American Association of Petroleum Geologists (AAPG) Bulletin, v. 80, p. 1896–1924.

Schultz-Ela, D.D., Jackson, M.P.A., and Vendeville, B.C., 1993, Mechanics of active salt diapirism: Tectonophysics, v. 228, p. 275–312, doi: 10.1016/0040-1951(93)90345-K.

Sharp, R.P., 1973, Fretted and chaotic terrain: Journal of Geophysical Research, v. 78, p. 4073–4083, doi: 10.1029/JB078i020p04073.

Skinner, J.A., Jr., and Mazzini, A., 2009, Martian mud volcanism: Terrestrial analogs and implications for formational scenarios: Marine and Petroleum Geology, v. 26, p. 1866–1878, doi: 10.1016/j.marpetgeo.2009.02.006.

Skinner, J.A., Jr., and Tanaka, K.L., 2007, Evidence for and implications of sedimentary diapirism and mud volcanism in the southern Utopia highland-lowland boundary plain, Mars: Icarus, v. 186, p. 41–59, doi: 10.1016/j.icarus.2006.08.013.

Smith, P.H., et al., 2009, H_2O at the Phoenix landing site: Science, v. 325, no. 5936, p. 58–61.

Spencer, J.R., and Fanale, F.P., 1990, New models for the origin of Valles Marineris closed depressions: Journal of Geophysical Research, v. 95, p. 14,301–14,313, doi: 10.1029/JB095iB09p14301.

Squyres, S.W., Grotzinger, J.P., Arvidson, R.E., Bell, J.F., III, Calvin, W., Christensen, P.R., Clark, B.C., Crisp, J.A., Farrand, W.H., Herkenhoff, K.E., Johnson, J.R., Klingelhöfer, G., Knoll, A.H., McLennan, S.M., McSween, H.Y., Jr., Morris, R.V., Rice, J.W., Jr., Rieder, R., and Soderblom, L.A., 2004, In situ evidence for an ancient aqueous environment at Meridiani Planum, Mars: Science, v. 306, p. 1709–1714, doi: 10.1126/science.1104559.

Talbot, C.J., 1998, Extrusions of Hormuz salt in Iran, *in* Blundell, D.J., and Scott, A.C., eds., Lyell: The Past Is the Key to the Present: Geological Society of London Special Publication 143, p. 315–334.

Talbot, C.J., and Aftabi, P., 2004, Geology and models of salt extrusion at Qum Kuh, central Iran: Journal of the Geological Society of London, v. 161, p. 1–14.

Talbot, C.J., and Jackson, M.P.A., 1987, Internal kinematics of salt diapirs: The American Association of Petroleum Geologists Bulletin, v. 71, p. 1068–1093.

Talbot, C.J., and Pohjola, V., 2009, Subaerial salt extrusions in Iran as analogues of ice sheets, streams and glaciers: Earth-Science Reviews, v. 97, p. 155–183, doi: 10.1016/j.earscirev.2009.09.004.

Talbot, C.J., Aftabi, P., and Chemia, Z., 2009, Potash in a salt mushroom at Hormoz Island, Hormoz Strait, Iran: Ore Geology Reviews, v. 35, p. 317–332, doi: 10.1016/j.oregeorev.2008.11.005.

Tanaka, K.L., 1997, Origin of Valles Marineris and Noctis Labyrinthus, Mars, by structurally controlled collapse and erosion of crustal materials: Proceedings of the 28th Lunar and Planetary Science Conference, p. 1169.

Tanaka, K.L., and Golombek, M.P., 1989, Martian tension fractures and the formation of grabens and collapse features at Valles Marineris: Proceedings of the 20th Lunar and Planetary Science Conference, v. 19, p. 383–396.

Tosca, N.J., McLennan, S.M., Clark, B.C., Grotzinger, J.P., Hurowitz, J.A., Knoll, A.H., Schröder, C., and Squyres, S.W., 2005, Geochemical modeling of evaporation processes on Mars: Insight from the sedimentary record at Meridiani Planum: Earth and Planetary Science Letters, v. 240, p. 122–148, doi: 10.1016/j.epsl.2005.09.042.

Treiman, A.H., Fuks, K.H., and Murchie, S., 1995, Diagenetic layers in the upper walls of Valles Marineris, Mars: Evidence for drastic climate change since the mid-Hesperian: Journal of Geophysical Research, v. 100, p. 26,339–26,344, doi: 10.1029/95JE03223.

van Keken, P.E., Spiers, C.J., van den Berg, A.P., and Muyzert, E.L., 1993, The effective viscosity of rocksalt: Implementation of steady-state creep laws in numerical models of salt diapirism: Tectonophysics, v. 225, p. 457–476, doi: 10.1016/0040-1951(93)90310-G.

Vendeville, B.C., and Jackson, M.P.A., 1992, The rise of diapirs during thin-skinned extension: Marine and Petroleum Geology, v. 9, p. 331–354, doi: 10.1016/0264-8172(92)90047-I.

Weijermars, R., Jackson, M.P.A., and Vendeville, B.C., 1993, Rheological and tectonic modeling of salt provinces: Tectonophysics, v. 217, p. 143–174, doi: 10.1016/0040-1951(93)90208-2.

Wilkins, S.J., and Schultz, R.A., 2003, Cross faults in extensional settings: Stress triggering, displacement localization, and implications for the origin of blunt troughs at Valles Marineris, Mars: Journal of Geophysical Research–Planets, v. 108, no. E6, p. 5056, doi: 10.1029/2002JE001968.

Witbeck, N.E., Tanaka, K.L., and Scott, D.H., 1991, Geologic map of the Valles Marineris region, Mars, U.S. Geological Survey Miscellaneous Investigations Series Map I–2010, scale 1:5,000,000.

Worrall, D.M., and Snelson, S., 1989, Evolution of the northern Gulf of Mexico, with emphasis on Cenozoic growth faulting and the role of salt, *in* Bally, A.W., and Palmer, A.R., eds., An Overview: Boulder, Colorado, Geological Society of America, The Geology of North America, v. A, p. 97–138.

Wyrick, D., Ferrill, D.A., Morris, A.P., Colton, S.L., and Sims, D.W., 2004, Distribution, morphology, and origins of Martian pit crater chains: Journal of Geophysical Research–Planets, v. 109, E06005, doi: 10.1029/2004JE002240.

Manuscript Received 30 March 2010
Revised Manuscript Received 23 June 2010
Manuscript Accepted 28 July 2010

Printed in the USA